SUB-6 GHZ 5G MIMO ANTENNA

A THESIS SUBMITTED TO
THE GRADUATE SCHOOL OF NATURAL AND APPLIED SCIENCES
OF
MIDDLE EAST TECHNICAL UNIVERSITY

BY

ABDURRAHMAN BAYLAN

IN PARTIAL FULFILLMENT OF THE REQUIREMENTS
FOR
THE DEGREE OF MASTER OF SCIENCE
IN
ELECTRICAL AND ELECTRONIC ENGINEERING

SEPTEMBER 2023

Approval of the thesis:

SUB-6 GHZ 5G MIMO ANTENNA

submitted by **ABDURRAHMAN BAYLAN** in partial fulfillment of the requirements for the degree of **Master of Science** i**n Electrical and Electronic Engineering, Middle East Technical University** by,

Prof. Dr. Halil Kalıpçılar
Dean, Graduate School of **Natural and Applied Sciences** _____

Prof. Dr. İlkay Ulusoy
Head of the Department, **Electrical and Electronics Engineering** _____

Prof. Dr. Özlem Aydın Çivi
Supervisor, **Electrical and Electronics Engineering** _____

Examining Committee Members:

Prof. Dr. Sencer Koç
Electrical and Electronics Engineering, METU _____

Prof. Dr. Özlem Aydın Çivi
Electrical and Electronics Engineering, METU _____

Prof. Dr. Gülbin Dural
Electrical and Electronics Engineering, METU _____

Assist. Prof. Dr. Ahmet Cemal Durgun
Electrical and Electronics Engineering, METU _____

Prof. Dr. Vakur B. Ertürk
Electrical and Electronics Engineering, Bilkent University _____

Date: 04.09.2023

I hereby declare that all information in this document has been obtained and presented in accordance with academic rules and ethical conduct. I also declare that, as required by these rules and conduct, I have fully cited and referenced all material and results that are not original to this work.

Name Last name : Abdurrahman Baylan

Signature :

ABSTRACT

SUB-6 GHZ 5G MIMO ANTENNA

Baylan, Abdurrahman
Master of Science, Electrical and Electronic Engineering
Supervisor : Prof. Dr. Özlem Aydın Çivi

September 2023, 120 pages

This thesis focuses on the design and optimization of a Sub-6 GHz Multiple-Input Multiple-Output (MIMO) antenna array tailored for 5G New Radio base stations. The unique attributes of 5G technologies, such as reduced latency, improved energy efficiency, increased connection density, and higher peak data rates, come hand in hand with the concepts of network densification, bandwidth enhancement, and spectral efficiency improvement. MIMO techniques, involving multiple antennas for diversity or multiplexing, further amplify the potential of 5G systems. The primary objective is to design and optimize a MIMO antenna array operating at the n78 band (3.3 - 3.8 GHz), which is designated for 5G applications in Europe. The research encompasses antenna array design, radiation pattern synthesis, performance optimization through simulations, prototype development, and comprehensive performance evaluation. The study targets an 8×4 antenna array configuration, exploring element number, spacing, and array geometry.

Keywords: MIMO Antennas, 5G Antenna Arrays, Stacked Patch Antennas, Slant Polarization, Active Element Pattern Synthesis

ÖZ

6 GHZ ALTI 5G ÇOK GİRDİLİ ÇOK ÇIKTILI ANTEN

Baylan, Abdurrahman
Yüksek Lisans, Elektrik ve Elektronik Mühendisliği
Tez Yöneticisi: Prof. Dr. Özlem Aydın Çivi

Eylül 2023, 120 sayfa

Bu tez çalışmasında, 5G Yeni Radyo baz istasyonları için özel olarak tasarlanmış 6 GHz altı Çok Girdili Çok Çıktılı (MIMO) anten dizisinin tasarımı ve optimizasyonuna odaklanmaktadır. Azalan gecikme süresi, iyileştirilmiş enerji verimliliği, artan bağlantı yoğunluğu ve daha yüksek veri hızları gibi 5G teknolojilerinin benzersiz özellikleri; ağ yoğunlaştırma, bant genişliği geliştirme ve spektral verimlilik iyileştirme kavramlarıyla sağlanır. Çeşitlilik veya çoğullama için birden fazla anten içeren MIMO teknikleri, 5G sistemlerinin potansiyelini daha da güçlendirir. Bu kapsamda bu çalışmanın amacı, Avrupa'daki 5G uygulamaları için belirlenmiş olan n78 bandında (3,3 - 3,8 GHz) çalışan bir MIMO anten dizisini tasarlamak ve optimize etmektir. Araştırma, anten dizisi tasarımını, ışıma örüntüsü sentezini, simülasyonlar yoluyla performans optimizasyonunu, prototip geliştirmeyi ve kapsamlı performans değerlendirmesini kapsamaktadır. Çalışma kapsamında, eleman sayısı, eleman aralığı ve dizi geometrisi irdelenerek 8×4 anten dizisi geliştirilmesi hedeflenmektedir.

Anahtar Kelimeler: MIMO Antenler, 5G Anten Dizileri, Yığınlı Yama Antenler, Eğimli Polarizasyon, Aktif Eleman Işıma Örüntüsü Sentezi

ø

ACKNOWLEDGMENTS

The author wishes to express his deepest gratitude to his supervisor, Prof. Dr. Özlem Aydın Çivi, for her guidance, advice, criticism, encouragement, and insight throughout the research.

Furthermore, the author is thankful to Tualcom Elektronik A.Ş. for their generous funding for manufacturing the prototypes in the context of this thesis.

TABLE OF CONTENTS

LIST OF TABLES

TABLES

LIST OF FIGURES

FIGURES

LIST OF ABBREVIATIONS

ABBREVIATIONS

5G	Fifth Generation Communication Technologies
AEP	Active Element Pattern
BS	Base Station
Co-Pol	Co-Polarization
dB	Decibel
EEE	Electrical and Electronics Engineering
EM	Electromagnetic
F/B	Front to Back Ratio
HPBW	Half Power Beam Width
LTE	Long-Term Evolution
MIMO	Multi Input Multi Output
mmWave	Milimeter Wave
MoM	Method of Moments
MPA	Microstrip Patch Antenna

PCB	Printed Circuit Board
Q	Quality Factor
SIW	Substrate Integrated Waveguide
SMA	SubMiniature version A
S Parameters	Scattering Parameters
TM	Transverse Magnetic
UE	User Equipment
VNA	Vector Network Analyzer
VSWR	Voltage Standing Wave Ratio
X-Pol	Cross Polarization

LIST OF SYMBOLS

SYMBOLS	
θ	Elevation angle
ϕ	Azimuth angle
λ_0	Wavelength in the free space
ϵ_r	Relative permittivity
ϵ_{reff}	Effective relative permittivity

CHAPTER 1

INTRODUCTION

Antennas serve as essential building blocks within wireless communication systems. Analogously, they enable us to capture and process unguided electromagnetic waves in the free space, much like how trees absorb water, carbon dioxide, and sunlight from the air during photosynthesis and release oxygen and glucose as output. Since antennas have this much critical role in communication systems, their design and implementation are of utmost importance.

With the rapid advancement of technology, the demand for wireless communications has grown substantially. Presently, fifth-generation (5G) communication technologies emerge as the leading solution to address this demand. As with any wireless communication system, antennas play a critical role as subsystems that influence performance and specifications, contributing significantly to the effective operation of 5G systems.

In this context, Sub-6 GHz MIMO (multi input multi output) antenna arrays that can be employed in fifth-generation (5G) communication applications are the major topic of this thesis study. This newest communication technology differs in a number of performance metrics from earlier communication technologies. In terms of latency, spectrum and network energy efficiency, connection density, and peak data rate, the 5G technologies offer a benefit [1].

These offerings come along with three enabling concepts. First of which is network densification, meaning shrinking the cell size used in cellular communication. The efficient spatial reuse of the spectrum and the reduction in the number of users competing for the same cell resources are the two advantages of lowering the cell size. The second key enabling concept is increasing the bandwidth since the higher

the bandwidth, the higher the data rate. The final one is increasing the spectral efficiency. The spectral efficiency indicates the amount of traffic that can be carried per unit bandwidth and unit area, i.e., increasing the number of bits/s/Hz per node. Once coverage area of a network provider and bandwidth have been determined, higher-level modulation schemes, multiple access approaches, and MIMO diversity via polarization and/or angular disposition can be used to improve spectral efficiency [2].

MIMO stands for a set of signal processing algorithms created to improve the performance of wireless communication systems using multiple antennas at the transmitter, receiver, or both. Diversity (for redundancy) or multiplexing can be achieved in MIMO by varying the spacing, cross-polarization, and/or angular orientation of more than one antenna. Diversity techniques, multiplexing techniques, multiple access methods, beamforming, and multi-functional MIMO arrangements, which are combinations of various MIMO techniques, are all examples of MIMO schemes.

This thesis study proposes a MIMO antenna array designed for utilization in 5G New Radio base stations, specifically operating in the n78 band. The selection of the n78 band as the operating frequency is deliberate, as this band is dedicated to 5G applications in Europe, including Türkiye, making it an ideal choice for the deployment and compatibility of the antenna with 5G networks at the region. In modern communication systems, planar antennas are favored for their compact footprint and seamless integration capabilities. Hence, the proposed antenna is also a planar patch antenna array. Several key stages are involved in the study, starting with the design and simulations of the unit antenna element. Following this, the prototype of the unit antenna element was manufactured, and measurements were conducted to assess its performance. Subsequently, the same steps were applied to the antenna array, encompassing its design, simulations, prototyping, and performance evaluation. By following this systematic approach, the overall antenna array was comprehensively analyzed and optimized, ensuring its effectiveness for 5G applications.

1.1 Literature Review

The transition towards 5G cellular communication has prompted the investigation of novel technologies and antenna concepts to fulfill the growing need for enhanced data rates and more effective wireless connectivity. Therefore, a considerable amount of literature is available on this topic. Given the specific focus of this thesis on Sub-6 GHz MIMO antenna arrays for 5G applications, the literature related to antennas in the context of 5G technologies is being shared.

Upon delving into the existing literature, the suggested design concepts can be categorized into distinct groups according to their common characteristics. The first group centers around the operating frequency of the intended antenna. Notably, two primary frequency ranges have been allocated for 5G utilization: the Sub-6 GHz region and the millimeter-wave region. The Sub-6 GHz spectrum has a well-recognized standing, and it is noteworthy that a significant portion of the sub-6 GHz bands aligns with previous generation communication technologies to enable dual connectivity. Conversely, the millimeter-wave (mm-Wave) region remains a subject of ongoing investigation.

In [3] - [5], mm-Wave region is utilized. In [3], a concept of a phased antenna array based on substrate integrated waveguide technology (SIW) for 5G base stations operating at 28 GHz is proposed. Another study, [4], employs multifunctional staggered 8×12 butterfly phased array antenna for 5G communications at 28 GHz. Also in [5], a planar linearly dual-polarized mm-Wave antenna array for the 24-GHz band is designed. On the other hand, studies [6] - [7], propose antenna designs operating at Sub-6 GHz region. In [6], a dual-polarized antenna is built based on full-wavelength dipoles which operates across the band from 1.63 GHz to 3.71 GHz, in order to cover both the LTE band from 1.7 to 2.7 GHz and the 5G band from 3.3 to 3.6 GHz, simultaneously. Similarly, [7] presents a planar, low-profile, and single-layer metasurface based 4×4 array operating at Sub-6 GHz band. Besides [3] – [7], there are some studies which incorporate both Sub-6 GHz and millimeter wave frequency regions in a single design [8],[9].

Another category that researchers in the field of 5G antenna design focus on is finding solutions to the challenges that come with designing antennas. One of the main problems for antennas on modern base stations is achieving wide bandwidth. It is preferred to make antennas that can cover the whole range of frequencies available, even if service providers do not use all of those frequencies. This is because having one design that spans all the available spectrum brings universal compatibility. However, it is not easy to make a single antenna that works well in all frequency ranges. To do this, it is necessary to make sure both the antenna element and feeding network achieve a wide bandwidth. Usually, there are three main ways researchers try to broaden the bandwidth of antennas: modifications to antenna shape, using a wideband balun and use of extra parasitic elements.

In [10] to [12], radiating elements are modified to enhance the bandwidth. In [10], a modified multi-dipole shape which results in nearly 60% impedance bandwidth is proposed. In [11], wideband, dual polarized crossed loop dipole antennas are presented in which extra loops are incorporated into original loops to excite a new resonant frequency. This technique results in a 51% measured impedance bandwidth. Similarly, in [12], 53% bandwidth is obtained by incorporating fan-shaped slots on the dipoles and etching chamfers at the diagonal lines on the dipoles.

Studies [13] and [14] incorporate wideband baluns in order to achieve wider bandwidth. In [13], a dual-polarized patch antenna element excited by an L-shaped probe pair is proposed resulting in 54% bandwidth. [14] proposes a broadband dual polarized base station antenna which has Y-shaped feeding lines to provide a wide impedance bandwidth of 45%.

The last method to enhance the impedance bandwidth is to use parasitic elements. In [15], four directly driven loop radiators with four parasitic loop elements are utilized in order to obtain 52% impedance bandwidth. In [16], a wideband dual polarized antenna array with 6 elements, which consists of 4 folded dipoles, a parasitic patch, and a convex-shaped reflector, is designed. A parasitic patch is located above the folded dipole in order to improve the impedance bandwidth by as much as 65%. In

[17], U shaped parasitic elements are utilized around the driven dipole elements, in order to achieve an impedance bandwidth of 63%. In [18], a massive MIMO array consisting of stacked patch antennas with dual polarization is proposed. In this study, patch antennas and metallic coupling strips are stacked on top of each other. Bow-tie shaped apertures are utilized on the ground plane in order to incorporate aperture coupled feeding. As a result, bandwidth is enhanced to 170 MHz.

There are several additional challenges related to MIMO and beamforming in the context of 5G technologies. Two main types of beamforming techniques are available in this context, which are analog and digital beamforming techniques. Butler matrix is a popular analog beamforming technique which is used in [19]. This study incorporates 4×4 Butler matrix in order to generate 4 different beams. In [20], a novel spherical Luneburg lens is utilized in a dual linear slant polarized antenna operating at 3.3-3.8 GHz range. On the other hand, lenses and Butler matrices are space occupying structures. Therefore, they prevent small and compact antenna designs. Also the other common analog beamforming techniques can be encountered in the antenna design such as the utilization of metasurfaces [21], parabolic cylindrical reflectors [22] and reconfigurable parasitic radiators [23].

Besides analog beamforming techniques, digital beamforming is a cutting-edge technology that plays an important role in modern wireless communication systems, particularly in the context of 5G and beyond. This technique involves adjusting the phases and amplitudes of signals from multiple antenna elements to form precise and dynamically adjustable radiation patterns. By doing so, digital beamforming enables the creation of directional beams that can be steered and adapted in real-time, offering significant advantages in terms of coverage, capacity, and interference mitigation.

Unlike analog beamforming, which employs passive components like phase shifters to adjust signal phases, digital beamforming harnesses the computational power of modern signal processing algorithms. This empowers wireless systems to adaptively focus and steer their transmission and reception beams toward specific users or areas,

enhancing the overall performance of the network. In this context, some concepts of digital beamforming technology are presented in [24].

Finally, literature regarding antenna design for 5G applications can be categorized around utilized antenna element type. The choice of unit antenna element type is of utmost importance in designing 5G MIMO antennas due to its direct impact on the overall performance and capabilities of the antenna array. The unit antenna element serves as the fundamental building block of the antenna array, and its characteristics significantly influence various aspects of the antenna system. In [25], various unit antenna element types are listed and compared based on their advantages and disadvantages. This comparison is presented in Table 1.1.

At this point, the proposed antenna array in this thesis study should be situated within the context of these categorizations. This study proposes a MIMO antenna array for 5G applications which operates at Sub-6 GHz range, specifically n78 band. Proposed antenna array, utilizes coaxial fed stacked patch antennas with air gap between its layers in order to enhance the impedance bandwidth. In order to perform beamsteering, beamforming and multi-beam generation digital beamforming method is utilized.

Table 1.1 Comparison of unit antenna element types [25]

Antenna Type	Advantages	Disadvantages
Monopole	• Simple to design and fabricate • In multi-element monopole antenna design, it can be easily rotated in any direction	• Less gain • Requires large area of ground • Gives poor response in bad weather condition
Dipole	• Simple to design and fabricate • Receives balanced signal	• Less gain • Cannot be used for long range communication • Low bandwidth
Magneto-Electric (ME) Dipole	• High front to back ratio • Low side lobe and back lobe level • Wide bandwidth • Low cross polarization	• Design and fabrication is complex • Costly
Loop	• Easy to design • Provides good channel capacity	• As single element loop antennas cannot meet the 5G requirements, multi-element loop antenna is required • Low gain
Antipodal Vivaldi Antenna (AVA)	• Enhances the gain • Provides wider bandwidth • Gives stable radiation pattern	• Requires more space • Low gain at lower frequencies
Fractal	• It helps to miniaturize antenna size • Provides wider bandwidth • Good impedance matching • Provides consistent antenna performance over the operating range	• Design is complex • Limitation on repetetion of fractal design
Inverted F Antenna (IFA)	• Smaller in size • Good impedance matching due to intermediate feeding	• Narrow bandwidth • Low gain
Planar Inverted F Antenna (PIFA)	• Low profile • Good impedance matching • Enhances front to back ratio	• Narrow bandwidth • Low gain

1.2 Objectives and Scope

The primary objectives of this thesis are to design and optimize a sub-6 GHz MIMO antenna array tailored for 5G New Radio applications. The research aims to achieve the following specific goals:

- Antenna Array Design: Develop an efficient and high-performance antenna array configuration suitable for 5G base stations operating in the n78 band (3.3 - 3.8 GHz) in compliance with European 5G standards.

- Radiation Pattern Synthesis: Investigate and implement advanced beamforming and beamsteering techniques to synthesize the far-field radiation pattern of the antenna array. The goal is to maximize coverage, spatial resolution, and signal quality for enhanced communication performance.

- Performance Optimization: Conduct parametric sweeps and simulations to optimize the physical properties of the antenna, such as element spacing, number of elements, and feed network design. Seek to achieve superior characteristics in terms of gain, directivity, and impedance matching.

- Prototype Development: Fabricate a physical prototype of the designed antenna array and assess its performance through comprehensive measurements.

- Performance Evaluation: Compare the measurement results with simulation outcomes to validate the accuracy and efficacy of the proposed design. Analyze the performance of the prototype in terms of radiation efficiency, bandwidth, and compatibility with 5G standards.

The scope of this study is focused on the design, simulation, optimization, and prototyping of a sub-6 GHz MIMO antenna array for 5G New Radio applications, particularly operating in the n78 band. The research primarily concentrates on the following aspects:

- Antenna Frequency Band: The study is limited to the sub-6 GHz frequency range, specifically the n78 band (3.3 - 3.8 GHz), which is designated for 5G applications in Europe, including Türkiye.

- Antenna Array Configuration: The research investigates the optimization of an antenna array configuration, exploring element number, element spacing, and array geometry.

- Radiation Pattern Synthesis: Advanced beamforming and beamsteering techniques are employed to synthesize the far-field radiation pattern of the antenna array for improved coverage and spatial resolution.

- Simulation and Prototyping: The study involves extensive simulations using the ANSYS HFSS software for design verification and optimization. A physical prototype of the antenna array was also fabricated and evaluated through measurements.

- Performance Evaluation: The performance of the designed antenna array is analyzed based on key parameters such as gain, directivity, impedance matching, and radiation efficiency. The evaluation will include a comparison of simulation results with measurement outcomes to validate the effectiveness of the design.

1.3 Thesis Outline

This study utilizes the 3D full-wave solver ANSYS HFSS for all antenna simulations, while MATLAB serves as a tool for active antenna array pattern synthesis and functions as the graphical interface. The thesis is organized into several chapters as follows:

Chapter 1 provides an overview of the objectives and structure of the research. It introduces the concepts of 5G New Radio, which offer advantages such as lower latency, higher spectrum and network energy efficiency, increased connection

density, and elevated peak data rates in wireless communication. Additionally, the proposed antenna array design is outlined in this chapter.

Chapter 2 provides a comprehensive theoretical background on MIMO antenna systems for 5G applications. It begins by covering MIMO system concepts, and square patch antennas, along with their corresponding feed methods and polarizations. The radiation mechanism and other essential aspects of patch antennas are analyzed in detail. Additionally, the study investigates stacked patch antennas with air gaps to explore their potential benefits. Finally, design specifications are determined based on the specifications of reference commercial designs and provided to be followed throughout the thesis.

Chapter 3 presents the simulation environment and simulation setup. The chosen antenna topology is presented, along with its physical aspects, including dimensions and stack-up configuration. Parametric sweeps are performed to explore the physical properties of the antenna using the simulation environment. The study highlights the optimal parameters and their resulting characteristics. Once the design is finalized, the steps for prototyping are detailed. Subsequently, the fabricated prototype is measured, and a comprehensive comparison with simulation results is conducted, accompanied by a detailed analysis of the performance of the design.

Chapter 4 digs into the exploration of antenna array configurations, including the investigation of element number and element spacings. It showcases the resulting antenna array radiation pattern and its beamforming/beamsteering capabilities. Additionally, the design process for the feeding network of antenna elements is presented, followed by the analysis of simulation results related to the antenna array with the feeding network. Once the design is refined, the chapter outlines the steps involved in prototype production. Subsequently, the fabricated prototype undergoes comprehensive measurements, and a detailed analysis of its performance is conducted, drawing comparisons with simulation results to assess the effectiveness of the design.

Chapter 5 examines the far-field pattern of the 8×4 antenna array, which is synthesized by utilizing the measured active element patterns. To accomplish this, the 1×4 sub-array radiation pattern measurements, previously presented in Chapter 4, are processed in the MATLAB environment. The synthesis results are then compared with simulation results obtained from ANSYS HFSS to validate the agreement between measurements and simulations.

CHAPTER 2

THEORETICAL BACKGROUND of MIMO ANTENNA SYSTEMS and 5G APPLICATIONS

This chapter presents an exploration of MIMO system concepts that enhance the efficiency of wireless communication systems. It also delves into the operating frequency bands for 5G applications and examines how communication system performance is influenced by bandwidth. Within the context of these concepts and effects, a comprehensive investigation into microstrip patch antennas and their diverse types is conducted, given their potential advantages in the realm of 5G MIMO antenna configurations. Additionally, the chapter explores slant polarization techniques applied to microstrip patch antennas, as they hold promise in delivering polarization diversity within MIMO systems. Finalizing this chapter, a set of design specifications is provided to establish the foundation of this thesis study, serving as a guideline for the design of the proposed antenna array.

2.1 MIMO System Concepts

The adoption of the 5G communication systems brings about a substantial transformation in wireless communication. One of the notable differentiators of 5G in comparison to its predecessors is the predominant integration of MIMO technology. This technology is characterized as a set of signal processing techniques developed to elevate the efficiency of wireless communication systems through the incorporation of multiple antennas at the transmitter, receiver, or both. By employing an array of antennas, MIMO facilitates diversity or multiplexing, achieved through spacing, cross-polarization, and/or angular arrangement [2]. The incorporation of

MIMO systems plays a pivotal role in augmenting the capacity, coverage, and overall performance of contemporary wireless networks.

The fundamental principles of MIMO technology are based on spatial multiplexing and beamforming. Through the utilization of the spatial dimension, MIMO facilitates the concurrent transmission of numerous data streams using a shared frequency channel. Each pair of antennas adds an extra communication path, consequently enhancing the overall capacity of the system [26].

Some key enabling concepts and benefits of the MIMO systems are summarized below.

1. **Spatial Diversity:** MIMO provides spatial diversity by transmitting identical information through more than one antenna. The receiver can then exploit the varied received signals to mitigate fading effect and enhance signal quality. This spatial diversity results in decreased error rates and improved resilience against channel impairments [27].

2. **Spatial Multiplexing:** MIMO systems facilitate spatial multiplexing, wherein separate data streams are transmitted simultaneously via identical frequency bands at different spatial paths. This results in a substantial augmentation of data rates and network capacity. Through optimal distribution of data across different spatial routes, the system can enhance spectral efficiency to the fullest extent.

   Contrary to spatial diversity, spatial multiplexing is a concept wherein separate data streams are transmitted through different spatial routes (basically through different beams) whereas in spatial diversity identical data streams are transmitted through different spatial paths to mitigate fading [28].

3. **Beamforming:** MIMO involves sophisticated beamforming methods that enable the generation of concentrated beams targeted towards particular directions. This not only amplifies coverage but also enhances signal strength

for users positioned in the designated direction. Beamforming plays a crucial role in serving multiple users concurrently and mitigating interference.

4. **Massive MIMO:** An inherent characteristic of 5G, known as massive MIMO, entails the installation of a substantial quantity of antennas at both the base station and user equipment. This strategy yields unparalleled enhancements in spectral efficiency, capacity, and coverage. Massive MIMO setups can efficiently cater to numerous users concurrently, all while upholding high data rates and the reliability of connections [29],[30].

5. **Hybrid Beamforming:** In MIMO systems used for 5G applications, hybrid beamforming methods are frequently adopted to address the difficulties arising from hardware complexities and power usage. By employing a mix of digital and analog beamforming, hybrid systems find an equilibrium between performance optimization and the limitations of available resources.

6. **Polarization Diversity:** Polarization diversity within 5G MIMO systems refers to the employment of various polarizations during the transmission and reception of signals. This involves the utilization of antennas capable of transmitting and receiving signals with diverse polarizations, encompassing horizontal, vertical or circular polarizations. An essential advantage of polarization diversity is its potential to mitigate multipath fading. Furthermore, polarization diversity yields the advantage of increasing the data-carrying capacity of the channel. By employing diverse polarizations, the system can simultaneously transmit numerous independent data streams, ultimately elevating the data rate and capacity of the system [31].

In conclusion, MIMO technology stands as an important foundation within the 5G communication systems, providing an array of substantial benefits that redefine wireless connectivity. At its core, MIMO utilizes the power of spatial diversity, spatial multiplexing, polarization diversity and advanced beamforming techniques to revolutionize the way data is transmitted and received.

Notably, it is imperative to emphasize that the successful deployment of all these concepts heavily depends on effective antenna design. In essence, transformative potential of the MIMO technology within 5G communication systems can only be fully utilized through careful antenna design. Antennas emerge as the vital interface that bridges theoretical benefits of the mentioned concepts with real-world communication performance.

2.2 5G Frequency Bands and Effect of Bandwidth in System Performance

Enhancing bandwidth and data rate within wireless communication are interconnected ideas that jointly enhance the general efficiency and potentialities of a communication system. Bandwidth pertains to the spectrum of frequencies applicable for signal transmission within a communication channel. A broader bandwidth permits the transmission of a larger volume of data within a specific time frame. This correlation becomes evident when considering Shannon's channel capacity formula, a renowned equation in communication theory, which is expressed as follows:

$$C = B \log_2(1 + S/N) \tag{2.1}$$

where C is the achievable channel capacity in bit/sec, B is channel bandwidth in Hz, S and N are signal and noise powers in Watts, respectively.

Expanding the accessible bandwidth can also result in enhanced capacity concerning the number of users accommodated. With a broader bandwidth, the communication channel gains the capability to concurrently serve numerous users, each with their individual data streams. This becomes pivotal in situations involving a substantial quantity of connected devices, as it facilitates effective distribution of the available frequency spectrum among users.

Following the introduction of the impact of the channel bandwidth on wireless communication system performance, the subsequent focus is on the frequency bands

Table 2.1 5G Operation Bands

Name of the band	Frequency Range (GHz)
n77	3.3 - 4.2
n78	3.3 – 3.8
n79	4.4 – 5.0
n257	26.5 – 29.5
n258	24.25 – 27.5
n260	37.0 – 40.0
n261	27.5 – 28.35

for 5G applications. The specified bands for 5G are commonly categorized into two groups: those below and those above 6 GHz (Table 2.1). A substantial portion of the sub-6 GHz bands align with LTE (Long-Term Evolution) to facilitate dual connectivity. Notably, the frequency range spanning from 24.25 to 29.5 GHz, namely mm-Wave region is under active examination [2].

As the operational frequency increases, the potential to construct broader bandwidth components in microwave and antenna theory expands due to the influence of quality factor. This paves the way for achieving more extensive bandwidth systems while maintaining a constant quality factor. Consequently, components within the mmWave region inherently possess the advantage of harboring sufficiently broad bandwidth. However, it is important to note that the mmWave region does exhibit certain drawbacks. These encompass relatively elevated atmospheric, rain, and foliage absorptions, leading to propagation losses. Furthermore, the mmWave region is subject to decreased specular reflection, which reduces the power intensity at the receiver end, and it also holds increased vulnerability to blockages. Nevertheless, the progression of the technology holds the potential to alleviate these adverse effects, as the utilization of the mmWave region becomes more prevalent [2].

On the other hand, the Sub-6 GHz spectrum range has a well-established reputation, with its familiar attributes making it a strong candidate for the imminent integration

of 5G technology. Within the context of this thesis, n78 band for antenna design is deliberately selected which is notably significant since this specific frequency band is exclusively designated for 5G applications in Europe, including Türkiye. This choice ensures alignment with the prevailing 5G networks of the region, reaffirming its appropriateness for the deployment and seamless integrationof the antenna.

The deliberate selection of this frequency band necessitates meticulous antenna design considerations, particularly due to the inherent challenge of achieving wider bandwidth at lower frequencies. Within the designated band of interest (3.3 - 3.8 GHz), the incorporation of the bandwidth enhancement techniques becomes paramount. These techniques will be mentioned and discussed in the subsequent sections, addressing the imperative need to optimize the bandwidth performance in the chosen frequency range.

In conclusion, the relationship between enhancing the bandwidth and data rate in wireless communication is crucial. A wider bandwidth enables the transmission of more data within a given time frame, as emphasized by Shannon's channel capacity formula. Additionally, broader bandwidth supports concurrent user connections, which is vital for scenarios with numerous devices.

In the context of 5G, the sub-6 GHz range emerges as a favorable choice due to its familiar characteristics. The deliberate selection of the n78 band for antenna design ensures compatibility with 5G networks of Europe. However, proposed antenna design within this band should overcome challenges due to achieving wide bandwidth at lower frequencies.

2.3 Microstrip Patch Antennas

When considering factors such as size, weight, cost, performance, ease of installation, and profile, microstrip patch antennas (MPAs) present an advantageous solution that aligns with these requirements. MPAs possess an inherently minimal profile, making them adaptable to a variety of planar and non-planar surfaces. They

are cost-effective to manufacture using modern PCB (Printed Circuit Board) technology, contributing to their affordability, and are easily integratable with other technologies or applications. Moreover, their properties can be tailored extensively, including the resonant frequency, polarization, radiation pattern, and input impedance.

Despite these merits, it is important to acknowledge some of their drawbacks, such as relatively lower efficiency, limited power handling capability, a high quality factor (which can be problematic when broad bandwidth is sought), and challenges in maintaining polarization purity. However, the range of applications for MPAs remains extensive, encompassing areas like aircraft, spacecraft, satellites, missiles, and various mobile, radio, and wireless communication systems.

It is worth noting that strategies exist to mitigate certain disadvantages of MPAs. For instance, techniques involving bandwidth enhancement can be employed to address some of these limitations. Some of these approaches will be mentioned in more detail later in this scope.

Given its vast number of advantages, including its compact size, low profile, ease of fabrication, configurability for arrays, capacity to integrate the concepts outlined in sections 2.1 and 2.2, seamless compatibility with other hardware components (such as transmitters), and potential for addressing its drawbacks, MPAs emerge as highly suitable candidates for Sub-6 GHz 5G MIMO antenna array applications. Consequently, this section will delve into a comprehensive exploration of MPAs within this context.

Figure 2.1(a) illustrates the fundamental configuration of a MPA. This design entails a thin metallic patch with a thickness denoted as t, where usually $t \ll \lambda_0$, with λ_0 being the wavelength in free space. The patch rests atop a ground plane and is separated by a dielectric substrate characterized by a height h. It is noteworthy that height of the substrate remains considerably smaller than the free space wavelength. Within the context of a rectangular patch, the L and W dimensions signify the length and width of the patch, respectively. Typically, the length L is chosen to be nearly

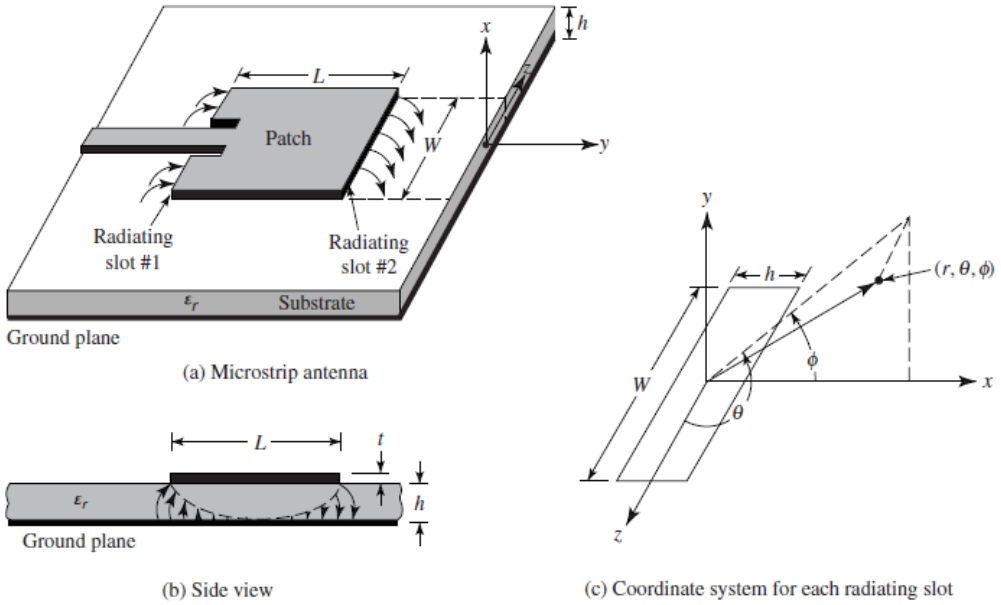

Figure 2.1. Structure of microstrip pach antennas [32]

half the effective wavelength, a factor that substantially influences the resonant frequency.

Substrates for MPAs come in diverse types, with their dielectric constants spanning the range from 1 (for substances like air or foam) to 40. The choice of substrate depends on the priorities of the application. When aiming for enhanced efficiency and broader bandwidth, thicker substrates with lower dielectric constants are favored. However, this decision results in a larger overall antenna size. Conversely, thinner substrates featuring higher relative permittivity curtail undesired radiation and coupling effects. This path leads to a more compact antenna size, yet at the trade-off of reduced efficiency and relatively narrower bandwidths.

Regarding their shapes, MPAs exhibit a variety of options, including square, rectangle, triangle, circle, disk, and dipole forms. Among these shapes, the rectangular and square configurations are most commonly employed. These shapes are preferable due to their ease of analysis and simpler fabrication processes.

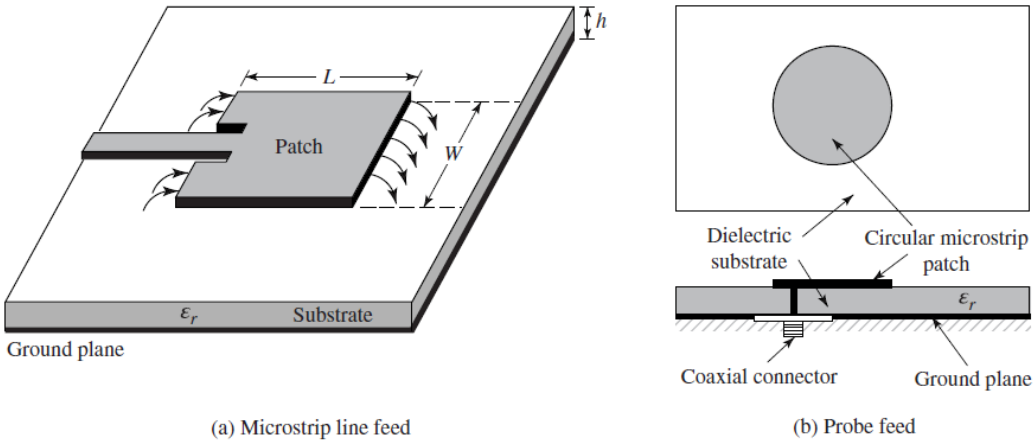

Figure 2.2. Common feeding methos for MPAs [32]

Several feeding methods are utilized for MPAs. The most common ones are microstrip line feeding and coaxial probe feeding, although there are some other methods such as aperture coupling feeding and proximity coupling feeding.

Common feeding methods are presented in Figure 2.2. The feeding method by microstrip transmission line has very easy fabrication process and simple matching procedure by adjusting inset position of the microstrip line. However, by increasing substrate thickness, undesired radiation increases due to surface waves and spurious feed radiation. On the other hand, coaxial probe feeding utilizes inner conductor of a coaxial transmission line which is attached to the radiating patch and outer conductor is attached to the ground plane. This method also has simple fabrication process and simple matching procedure by adjusting the probe position.

Furthermore, a graph depicting the normalized input resistances of MPAs fed by microstrip lines, which are calculated using analytical methods is presented in Figure 2.3 [32]. This principle can also be extended to probe-fed MPAs, where the position of the probe on the patch can be adjusted similarly to achieve the desired impedance characteristics.

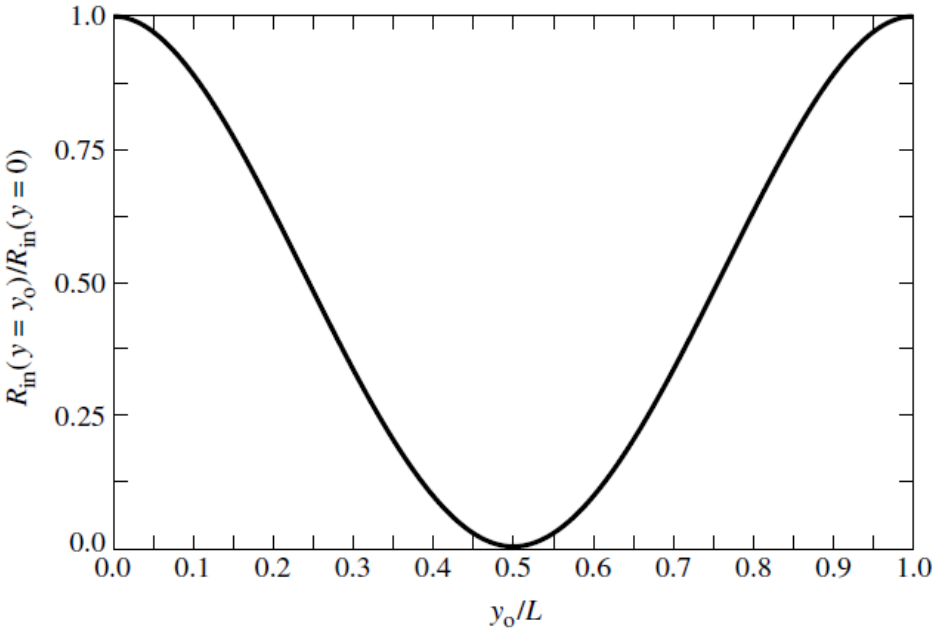

Figure 2.3. Inset length dependency of input impedance of a MPA [32]

An inherent characteristic that holds profound significance in the realm of MPAs is the quality factor (Q). The quality factor serves as a pivotal indicator, establishing an inverse relationship with the fractional bandwidth of the antenna. It is quantitatively expressed in [33] as :

$$Q = \frac{2\omega \max\{W_e, W_m\}}{P_d} \tag{2.2}$$

where P_d signifies the dissipated power within the antenna due to various losses, ω stands as the angular frequency. W_e and W_m denote the electrically and magnetically stored energy, respectively.

The interplay of certain factors bears a profound influence on the Q of MPAs. One such factor is the substrate height (h), which carries the potential to significantly impact the capacitive energy storage of the antenna. As substrate height increases, the capacitively stored energy within the microstrip patch antenna decreases, consequently leading to a reduction in the quality factor. This phenomenon, in turn,

amplifies the bandwidth of the antenna, allowing it to cover a wider range of frequencies effectively.

A second determinant in this relationship is the relative permittivity (ϵ_r) of the substrate. A decrease in the relative permittivity results in a corresponding reduction in the capacitive energy stored within the antenna. As with the increase in substrate height, this modification contributes to a decrease in the quality factor and an expansion of the bandwidth.

In addition to the aforementioned inherent methods for broadening the bandwidth, there exists a range of other techniques outlined in [34] that serve to further augment the bandwidth of MPAs. Among these strategies, a prominent group is linked to the feeding mechanism. These techniques operate with the intention of generating an additional resonant frequency by creating a coupling between the feeding structure and the patch itself. Two key members of this technique are the proximity and aperture coupled feeds.

The proximity coupled feed technique involves creating an electromagnetic coupling between the feeding structure and the patch through the substrate. This coupling fosters an additional resonant frequency, thus widening the bandwidth. This method offers the advantage of reduced electromagnetic interference due to the segregation of the feeding mechanism from the radiating patch.

Aperture coupled feeds, on the other hand, implement an aperture in the ground plane beneath the patch antenna. This aperture facilitates a controlled coupling between the patch and the feeding structure, giving rise to a supplementary resonant frequency. The advantage of aperture coupled feeds lies in their capacity to maintain improved isolation between the feeding mechanism and the radiating element, contributing to enhanced performance and lower losses.

Another group of techniques underscored in [34] involves harnessing the potential of parasitic elements. Through the strategic introduction of the auxiliary elements, coupled to the driven element, the overall bandwidth of the antenna can be

effectively expanded, provided that the resonant frequencies of these additional components are carefully adjusted. This concept is illustrated in Figure 2.4.

These auxiliary elements, often referred to as "dummy elements," can be integrated into the antenna design in various ways. They can exist on the same layer as the main element, or they can be stacked atop one another, operating in tandem to broaden the bandwidth. Moreover, alternative resonant frequencies can be generated by etching slots of varying shapes on the main radiating element. This technique not only augments the antenna bandwidth but also introduces versatility into the design by accommodating multiple resonant frequencies.

The utilization of the parasitic elements introduces a realm of creative possibilities for engineers seeking to enhance the performance of MPAs. By ingeniously manipulating these auxiliary elements and their coupling mechanisms, it becomes possible to tailor the frequency response of the antenna to specific application requirements, effectively widening its operational bandwidth and optimizing its overall efficiency.

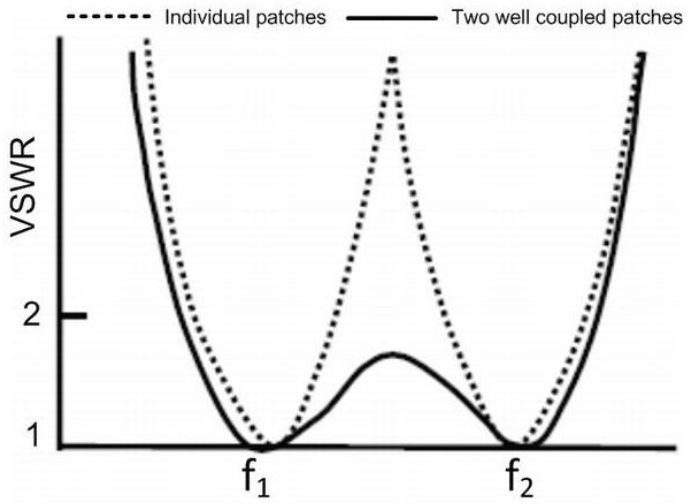

Figure 2.4. Bandwitdh enhancement by integrating elements having two different resonant frequencies [34]

2.4 Coaxial Fed Stacked Patch Antennas with Air Gap

The bandwidth of MPAs can be extended by incorporating additional parasitic elements, which introduce new resonant frequencies. These parasitic elements can either be coplanar with the driven patch, which increases the overall size of the antenna and makes it unsuitable for an array element, or multiple patches can be stacked on top of each other to achieve multiresonance. The latter approach allows stacked antenna elements to be easily utilized in array configurations.

One of the most prevalent types of these multiresonator antennas is the coaxial-fed stacked square patch antenna with an air gap between the layers, as depicted in Figure 2.5. In this design, the coaxial line excites the bottom patch, while the top patch is driven parasitically through electromagnetic coupling. The square patches are placed on different substrate layers, and an air gap is inserted between them to enhance the bandwidth. When the sizes of the two patches are electrically close to each other, their accompanying resonant frequencies become very similar, resulting in a broad

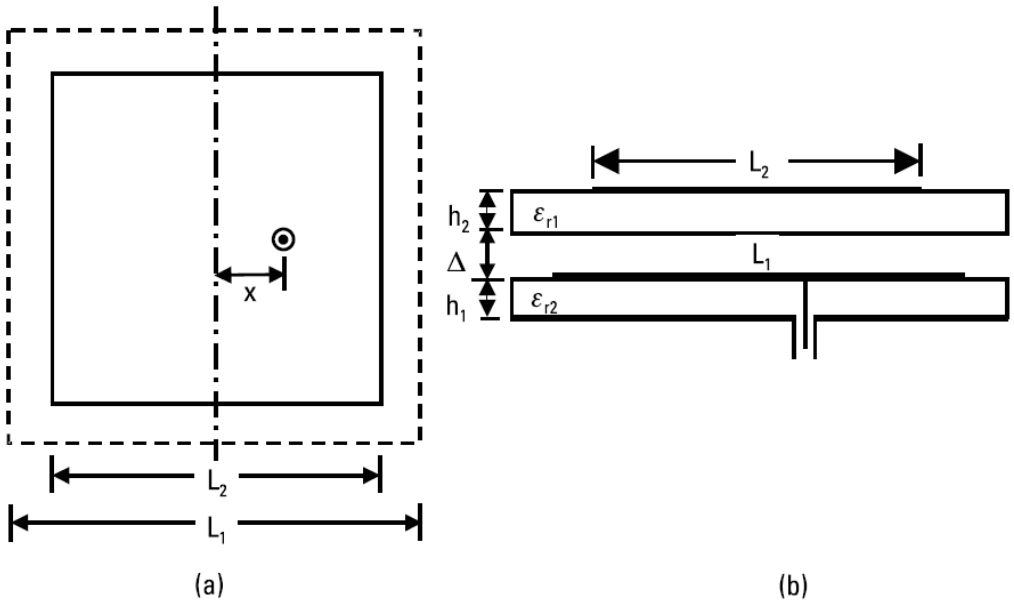

Figure 2.5. (a) Top and (b) side views of coaxial fed stack patch antenna with air gap between the patch layers [35]

bandwidth. By adopting this approach, a bandwidth of 10-30% can be achieved [35]. The expansion of the bandwidth is accomplished by increasing the overall height of the antenna, reducing the effective dielectric constant through the air gap between the layers, and taking advantage of the multiresonator effect.

Also, antenna radiation pattern is observed to be non-varying within the bandwidth of the antenna. Additionally, increasing air gap thickness results in increased gain due to increased effective aperture of the antenna [35].

Considering advantages of the coaxial-fed stacked square patch antennas with an air gap, it can be concluded that this antenna topology offers several advantages, making it an ideal choice as the unit antenna element in the Sub-6 GHz MIMO antenna array. Firstly, the proposed topology allows for easy extension of the bandwidth, achieving a significant increase of the bandwidth of over 10%. This relatively broad bandwidth capability is highly advantageous in accommodating the ever-growing demand for higher data rates and improved network performance.

Another noteworthy advantage of this antenna topology is its minimal impact on the antenna height. Unlike other parasitic structures, which may require significant adjustments to the antenna physical dimensions, the coaxial-fed stacked patch antenna with an air gap affects only the antenna height. As a result, this antenna element can be seamlessly integrated into an antenna array without compromising the overall design.

Furthermore, the radiation pattern of the stacked patch antenna with an air gap exhibits relatively stable characteristics over its entire bandwidth. This desirable feature ensures consistent and predictable performance, making it suitable for applications where reliable signal transmission and reception are essential.

Considering these compelling reasons, the coaxial-fed stacked square patch antenna with an air gap emerges as an excellent candidate for the purpose of this thesis. This topology will serve as a cornerstone throughout the design process, enabling the development of an efficient and high-performing Sub-6 GHz MIMO antenna array.

2.5 Polarization Diversity and Slant Polarization Technique

As mentioned in Chapter 2.1, polarization diversity in 5G MIMO systems involves using different signal polarizations during transmission and reception, including horizontal, vertical, or circular polarizations. It helps counteract multipath fading and boosts the data-carrying capacity of the system. By employing diverse polarizations, the system can transmit multiple independent data streams concurrently, enhancing data rates and overall capacity since effectively the number of available channels are multiplied.

A square or rectangular MPA featuring two feed points arranged orthogonally produces two distinct polarizations: horizontal and vertical. An MPA designed with orthogonal dual feeds, particularly in a square shape, exhibits dual polarization at the same frequency due to its inherent symmetry. Conversely, a rectangular MPA provides dual orthogonal polarizations at separate frequencies corresponding to its length and width [35].

On the other hand, slant polarization techniques for microstrip patch antennas involve adjusting the polarization orientation to a diagonal angle instead of a strictly horizontal or vertical one. Achieving +45° or -45° polarizations is possible by locating the feed points along the diagonal axis of the square MPA. In Figure 2.6, various configuration setups are presented for different polarization scenarios, along with the resulting surface current directions depicted using distinct colors. These current distributions are aligned in parallel with the line connecting the feeding point and the center of the MPA. Notably, as the far zone electric field should align with the current density vector [32], the resulting polarization also conforms to the designated current directions.

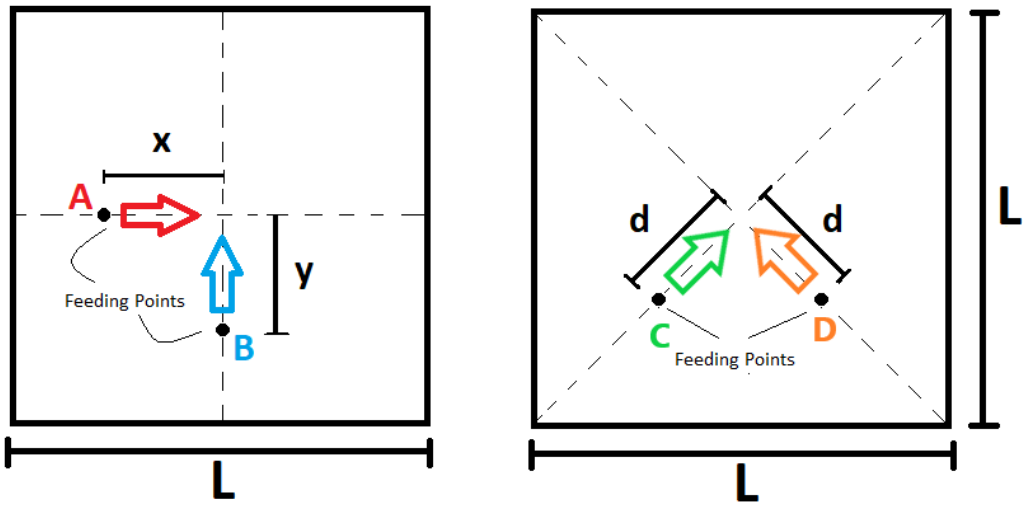

Figure 2.6. Different feeding points and resulting polarization configurations for square microstrip patch antennas (A-horizontal (0°) and B-vertical (90°) polarizations on the left - slant polarizations (+45° and -45 °/C and D) on the right)

2.6 Design Specifications and Summary

Within the framework of this thesis, the goal is to design a MIMO antenna array for 5G applications by incorporating the insights discussed in this chapter . This involves focusing on specific attributes of the design and specifying a set of design requirements.

First of all, considering discussions in this chapter, it can be said that the unit antenna element may be a coaxially fed stacked patch antenna with an air gap in between its layers. This topology is an appropriate candidate to fulfill the impedance bandwidth requirement of 500 MHz for the n78 band (3.3 – 3.8 GHz) by its potential. At the beginning, the 3.4 – 3.6 GHz sub-band of the n78 band is interested to be centered by operation band of the proposed antenna and, if possible, it is aimed to cover the whole n78 band.

Additionally, it is desired to include dual slant polarization capabilities to the proposed antenna array. This can be achieved by means of arranging the feed points

on the diagonal axes of the proposed coaxially fed stacked patch antenna. This choice makes the antenna versatile enough to handle the complexities of 5G communication.

Besides the properties of the unit antenna element, also the proposed array is desired to work effectively by ensuring that the array can handle spatial multiplexing, multi-beamforming, and beam steering which are discussed in the previous sections. This results in a substantial augmentation of the data rates and network capacity, and also plays a crucial role in serving multiple users concurrently and mitigating interference.

To guide this process, several commercially available 5G radio units are examined and a set of specifications are put together (Table 2.2) that will help shape the design of the array. This set of specifications is followed throughout the design phase of this thesis work.

Table 2.2 Antenna array desing specifications set

Operation Frequency Range	Preferably covering whole n78 band with centered around 3.4-3.6 GHz sub-band
Polarization	+45° and -45°
Gain	20 dBi
Horizontal Beam Scanning Range	-60° to +60° (with grating lobe occurrence when beam is steered to ±60°)
Vertical Beam Scanning Range	-15° to +15° (with grating lobe occurrence when beam is steered to ±15°)
Front to Rear Ratio	30 dB

CHAPTER 3

UNIT ANTENNA ELEMENT DESIGN, FABRICATION and MEASUREMENT RESULTS

This chapter digs into the process of designing the unit element of the antenna array, carefully aligning with the specifications outlined in Chapter 2. To reiterate, the proposed antenna element is expected to cover the 3.4-3.6 GHz sub-band of the n78 band, preferably having much more broader impedance bandwidth to preemptively counteract potential frequency shifts arising from manufacturing tolerances. This extended bandwidth also serves the practical purpose of accommodating neighboring frequency bands within a single antenna, enhancing spectrum utilization efficiency. Also another important specification is the antenna gain, in which element gain is important in order to determine the antenna array gain. High gain elements minimize the number of elements required to fulfill gain specification. Another requirement is slant polarized unit element antenna, which should have two orthogonal independent polarizations. Considering the aforementioned issues, double stacked patch antenna with air gap between its layers is a good nominee for unit antenna element. Throughout this chapter, the proposed unit element will be constructed in the ANSYS HFSS environment, and comprehensive simulations will be conducted to assess its properties. Once the design phase is over and structure is fully simulated, the chapter will proceed to the prototyping phase, where a physical prototype of the unit antenna element will be manufactured based on satisfying simulation results. Following a detailed section on prototyping, the antenna element undergoes S-parameter measurements. Finally, at the end of Chapter 3, the measurement results will be presented and analyzed.

3.1 Stacked Patch Antenna Element Design

The first step in the design phase involves developing the unit element for the antenna array. It is crucial to fulfill the requirements of frequency bandwidth, polarization, and other specifications for the antenna array element. The unit element plays a significant role in achieving antenna array gain and meeting the array input impedance requirement. To serve as the unit antenna element, a double-stacked patch antenna configuration with an air gap between the patch antenna layers has been proposed. This configuration allows for dual polarization by accommodating two feed points.

3.1.1 Geometry and Dimensions of the Antenna Structure

Figure 3.1 to Figure 3.3 (isometric, stack up and top views, respectively) illustrate the design. The structure consists of two Rogers RO4350B substrates (ϵ_r =3.66), each with a thickness denoted as H, separated by an air gap of thickness D. On top of each substrate, a square patch is positioned. A ground plane is present beneath the entire structure. The lower patch is directly fed by two probes, and their positions are arranged to ensure orthogonal excitation. Consequently, the upper patch is parasitically fed, resulting in two resonant frequencies within the structure.

The distance between the centers of the patches and the feed points in both the x and y dimensions is represented by dx. The dimensions of the square patches are denoted as W1 and W2, respectively. The locations of the feed points (dx) play a significant role in determining the input impedance of the antenna, while the patch dimensions (W1 and W2) are responsible for defining the resonant frequencies.

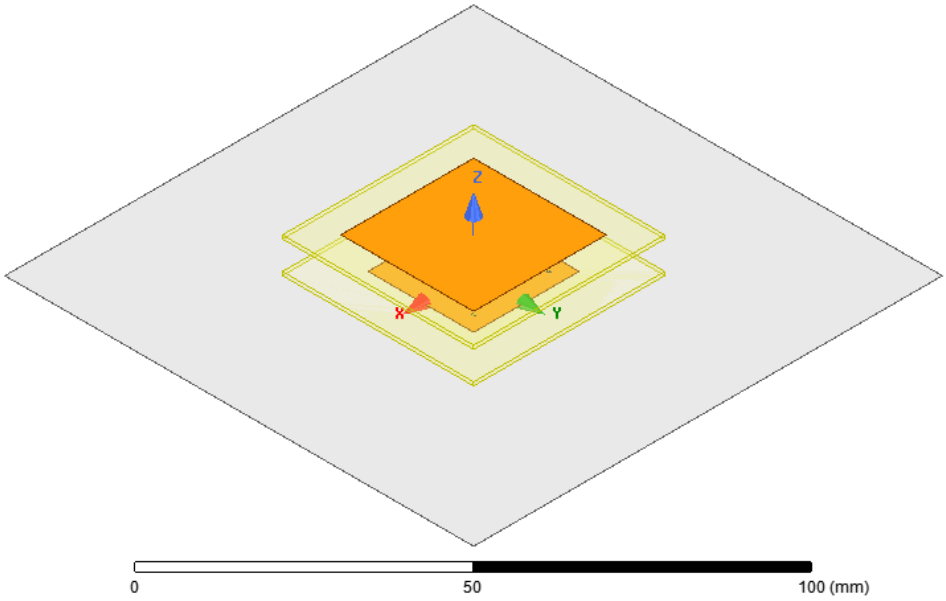

Figure 3.1. Isometric view of the unit antenna element

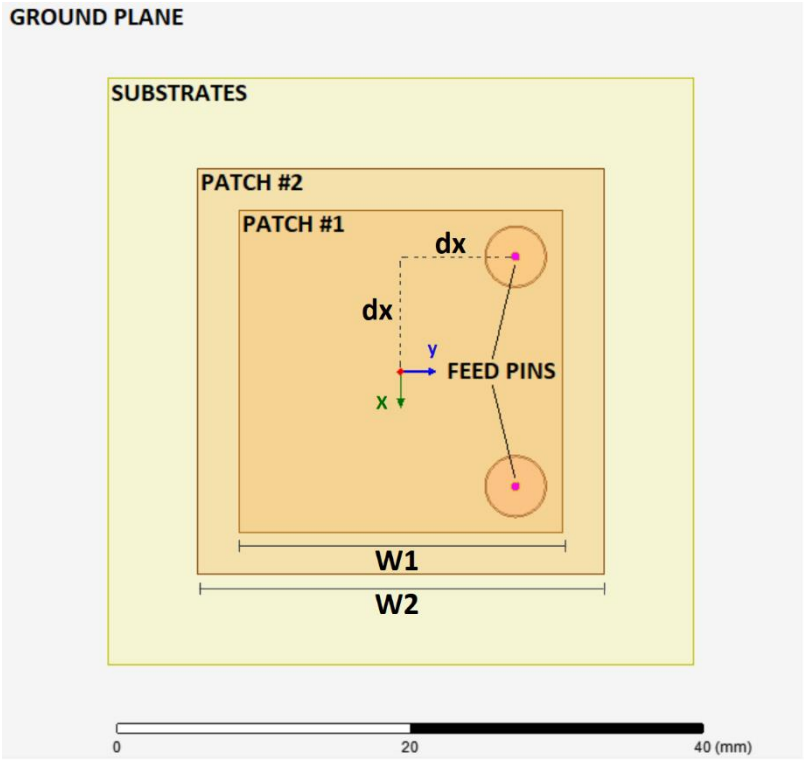

Figure 3.2. Top view of unit antenna element

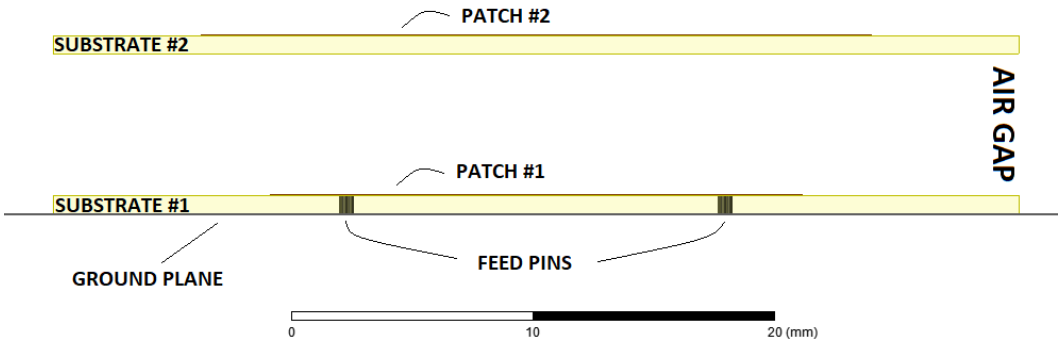

Figure 3.3. Layer stack-up of unit antenna element

Table 1 provides a list of the parameters along with their explanations. To explore the impact of these parameters, a set of simulations was conducted using the ANSYS HFSS 3D EM solver. The parameters listed in Table 1 were systematically varied during a parametric sweep. The results of this parametric sweep are presented in the next section.

Table 3.1 List of antenna parameters and their descriptions

Parameter	Description
H	Dielectric substrate thickness
D	Air gap thickness between substrates
W1	Width of square patch #1
W2	Width of square patch #1
dx	Distance between patch centers and feed locations in x and y directions
GND	Dimension of square shaped ground plane

3.1.2 Parametric Sweeps

In order to understand the impacts of the parameters given in Table 3.1 on the antenna performance, they are swept one by one. During parametric sweep of a

specific parameter, unswept parameters are kept constant at their nominal values. Nominal values of the parameters are given in Table 3.2.

The effect of sweeping the square patch dimensions, W1 and W2, is illustrated in Figures 3.4 and 3.5, respectively. Notably, there is an equilibrium state between resonant frequencies when W1=22.5 mm and W2=28.3 mm, where both resonant frequencies have equal weight and contribution to the reflection coefficient. As the patch dimensions increase, the equilibrium is disturbed and the resonant frequencies shift to the lower frequencies. Similarly, when patch dimensions are decreased, the equilibrium is disturbed in favor of higher frequencies. It can be observed that patch size variations are effective to determine the resonant frequencies.

Similarly, the impact of the feed point location on the reflection coefficient is demonstrated in Figure 3.6. As a reminder, the feed point is positioned on the diagonal axis of the patch to achieve slant polarization, and the dx dimension represents the offset from the patch center in both the x and y directions. It is observed that the feeding probe location determines the input impedance of the antenna element, while it does not have any effect on the resonant frequencies. This can be inferred from Figure 3.6, where changes in the level of S_{11} (reflection coefficient) are observed, but the curve remains unshifted on the frequency axis. Upon a thorough examination of Figure 3.6, it becomes apparent that dx=8 mm is a good point in terms of return loss. At this specific location, the antenna element exhibits a good performance in terms of impedance matching and reflection coefficient. Higher values of dx, on the other hand, are not preferred as they bring the feed point closer to the patch edge, making the design impractical and difficult to implement effectively.

Figure 3.7 illustrates the impact of varying the thickness of the air gap between the substrates (D). As D increases until reaching its optimal value (D = 6mm), the location of the upper resonant frequency shifts towards smaller values on the frequency axis, while the lower resonance frequency becomes dominant. Beyond this optimal point, the upper resonant frequency takes precedence. As discussed in

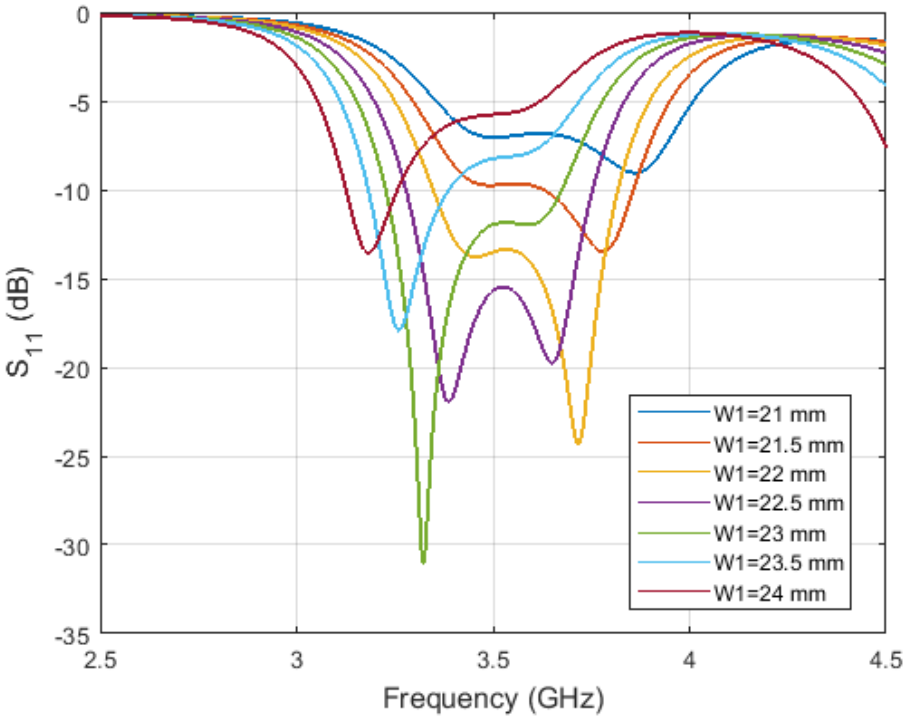

Figure 3.4. Return loss variation with respect to W1

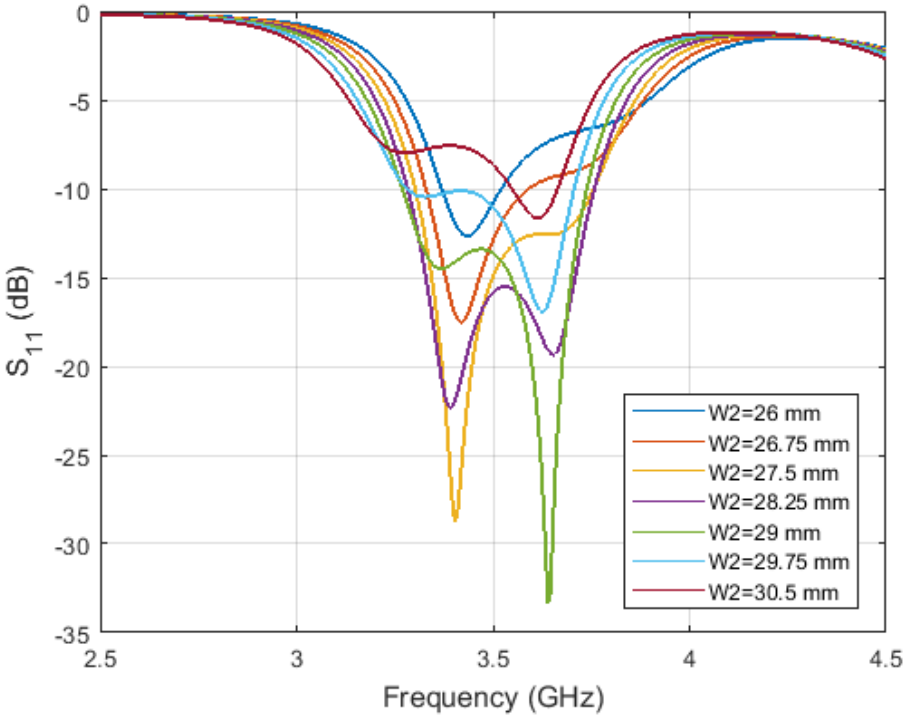

Figure 3.5. Return loss variation with respect to W2

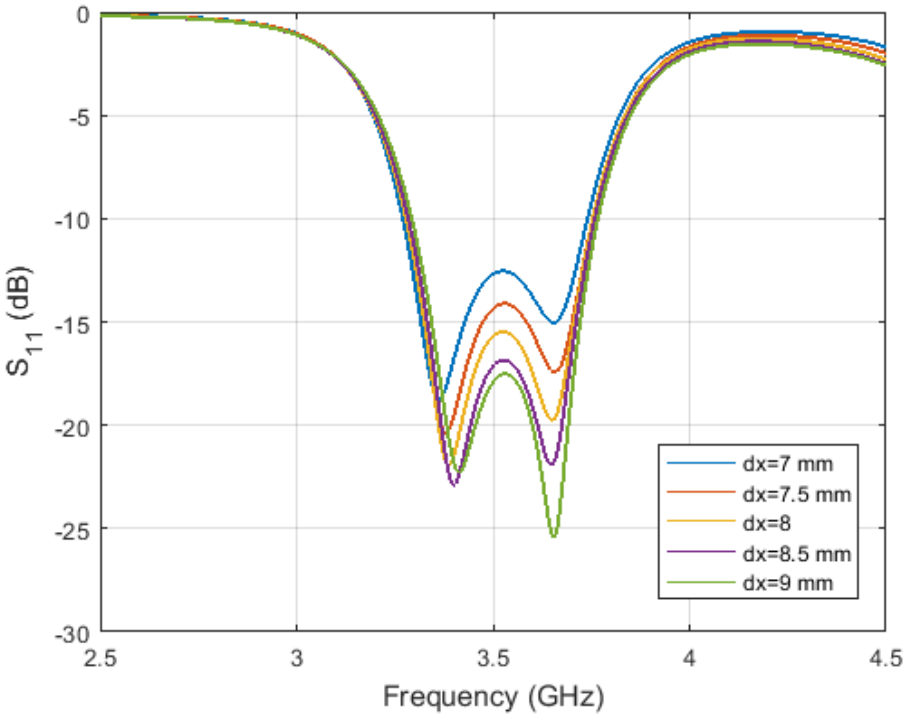

Figure 3.6. Return loss variation with respect to dx

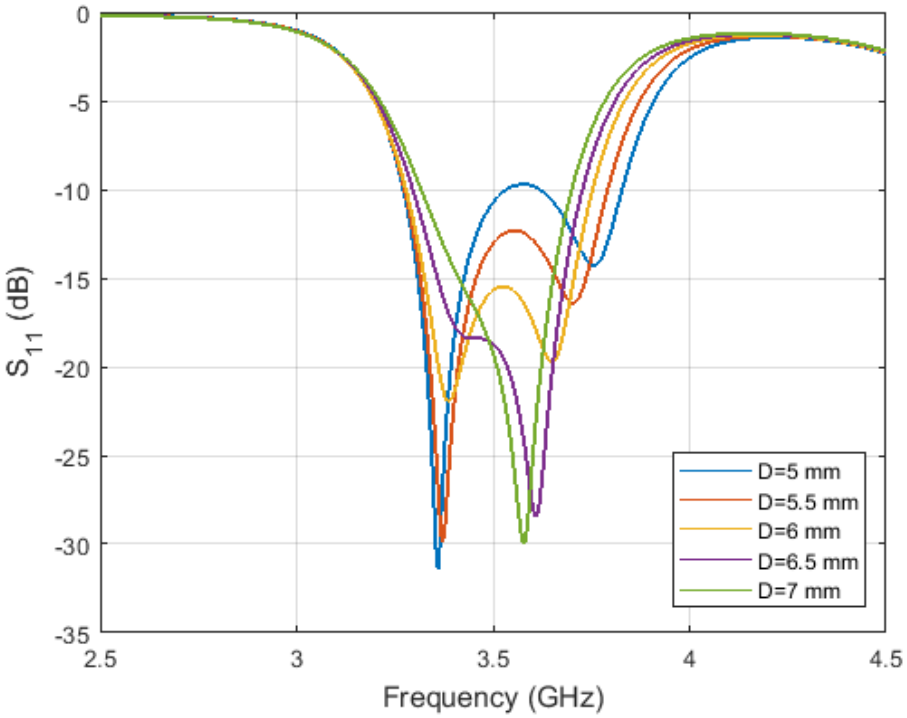

Figure 3.7. Return loss variation with respect to D

Chapter 2, D has a significant role in determining the bandwidth of the antenna. It can be seen in Figure 3.7 that how return loss curve creates wider windows on the -10 dB line as D varies.

The last parameter to be swept is the ground plane dimension, denoted as GND. Unlike W1, W2, and D, this parameter exhibits a behavior similar to the dx parametric sweep. As the ground plane size increases, the level of the reflection coefficient improves. However, it should be noted that a larger ground plane size requires more substrate usage during prototyping. Therefore, GND = 40 mm is a more suitable option as it is smaller, requiring less substrate usage, while still maintaining an acceptable reflection coefficient performance. It is worth mentioning that when the antenna array is constructed, it will have a much larger ground plane due to the presence of adjacent antenna elements. In this case, its behavior will resemble that of the GND = 100 mm scenario.

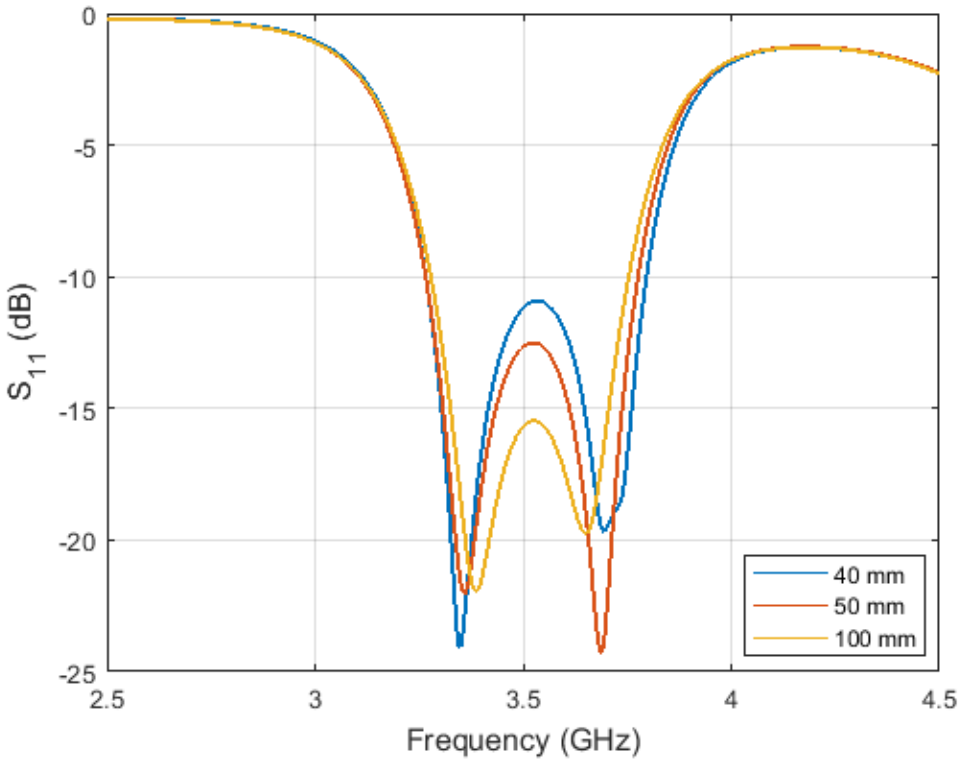

Figure 3.8. Return loss variation with respect to GND

After systematically sweeping the geometric variables of the antenna and conducting multiple optimization iterations, the desired specifications have been successfully achieved. Throughout these iterations, parametric sweeping was carried out while considering the reflection coefficient, as demonstrated in the previous figures. However, it is important to note that the unit antenna element possesses additional properties that should be addressed, including polarization, port isolation, and radiation pattern.

3.1.3 Simulation Results of Optimized Unit Antenna Element

In this section, the final version of the reflection coefficient of the antenna will be presented, as well as the ultimate versions of the aforementioned properties (polarization, port isolation, radiation pattern), once the optimal values of the parameters have been evaluated. These comprehensive evaluations allow us to assess the antenna performance completely, beyond solely focusing on the reflection coefficient.

The final values of the parameters used in the simulations are presented in Table 3.2, and the corresponding simulation results for this final parameter set can be found in Figures 3.9 to 3.18. These results offer insights into the antenna performance based on the chosen parameter configuration.

Table 3.2 Optimal values of the geometrical parameters of the antenna

Parameter	Value (mm)
H	0.762
D	6
W1	22.5
W2	28.3
dx	8
GND	100

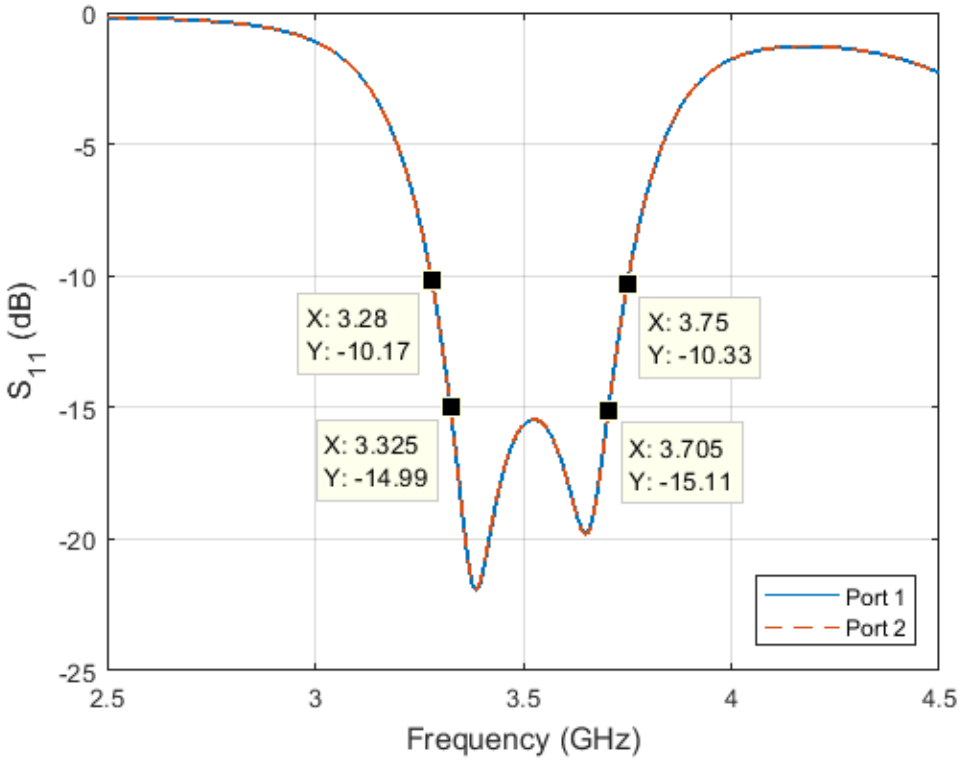

Figure 3.9. Return loss of the unit antenna element with optimal parameters

As shown in Figure 3.9, the reflection coefficient of the unit element exhibits good performance, consistently remaining well below the -10 dB threshold within the frequency range of 3280 MHz to 3750 MHz.

This return loss characteristic translates into a 470 MHz impedance bandwidth. Furthermore, even when considering a tighter requirement of achieving a -15 dB level of reflection coefficient, the proposed antenna meets this criterion with corner frequencies of 3325 MHz and 3705 MHz, resulting in a 380 MHz bandwidth.

These simulation results confirm that the proposed antenna is fully capable of operating within the 3400-3600 MHz subband of the 5G n78 band in terms of return

loss performance. The return loss performance of the antenna within this frequency range ensures reliable and efficient operation for 5G applications.

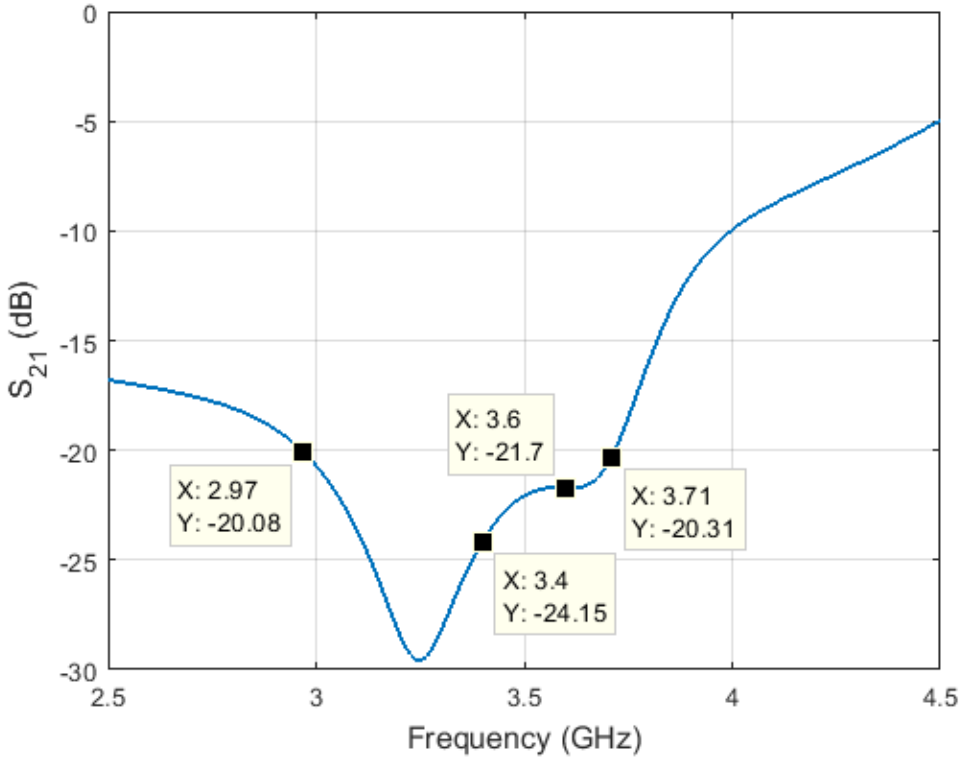

Figure 3.10. Port isolation of the unit antenna element with optimal parameters

Isolation between the input ports of the proposed unit antenna element is another crucial parameter that significantly impacts the antenna performance. Figure 3.10 illustrates the isolation results, providing valuable insights into this characteristic. Upon careful examination of Figure 3.10, it becomes apparent that sufficient isolation levels of more than 20 dB are achieved within the frequency range of 2970 MHz to 3715 MHz. Furthermore, within the narrower band of 3400 MHz to 3600 MHz, a minimum isolation of 21.7 dB is attained between the input ports.

This substantial level of isolation is highly significant, particularly when considering the signals transmitted or received from the two orthogonal polarizations of the proposed antenna. The achieved isolation ensures minimal interference between the signals, allowing for efficient and reliable communication. It guarantees that the

antenna can effectively handle the simultaneous transmission and reception of signals with different polarizations, resulting in optimal performance and a robust communication system.

One of the most critical parameters of the unit antenna element is its radiation pattern, which is provided in the following figures (Figure 3.11 to 3.17). Figure 3.11 presents the 3D polar radiation pattern at 3.5 GHz. Figures 3.12 to 3.17 show the 2D radiation patterns at different frequencies for +45° polarized excitations and for ϕ=0° and ϕ=90° planes. Also in these figures, some cursors (C1 and C2) and markers (Marker 1 and Marker 2) are provided corresponding to Half-Power Beamwidth, broadside antenna gain and back-lobe antenna gain, respectively. Upon analyzing these figures, it becomes evident that the main lobes are oriented in the broadside direction. Moreover, as the frequency increases from 3.3 GHz to 3.8 GHz, the electrical dimensions of the patch also increase, resulting in a gain enhancement from 9.54 dB to 10.26 dB. A similar phenomenon is observed in the Half-Power Beamwidth (HPBW), which decreases from 64° to 56°. The Front to Back Ratio (F/B Ratio) is observed to be approximately 17 dB for the radiation patterns. This ratio indicates the level of signal strength between the front (main lobe direction) and back (opposite) direction of the antenna. As expected, the antenna patterns are symmetrical along the ϕ direction. This symmetry is a desirable feature as it ensures consistent and uniform radiation characteristics in all directions.

The polarization characteristics of the unit element antenna are illustrated in Figure 3.18 (a) to Figure 3.18 (d). Based on the simulation results, it is evident that the current on the patch surfaces aligns diagonally (+45° and -45°) with respect to the patches, exactly as expected. This configuration results in the anticipated slant polarization.

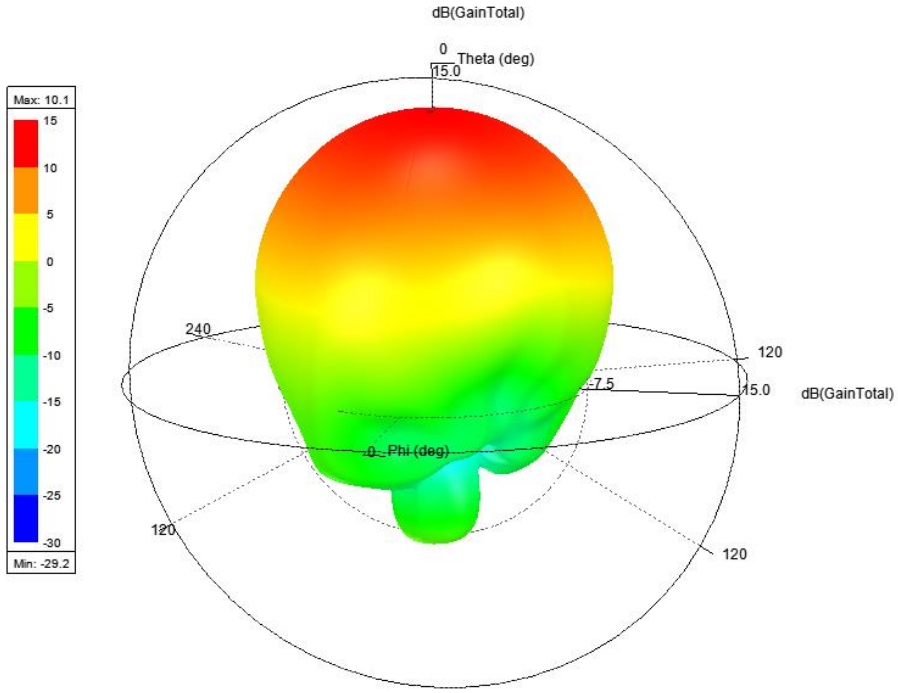

Figure 3.11. 3D radiation pattern of the unit antenna element at 3.5GHz

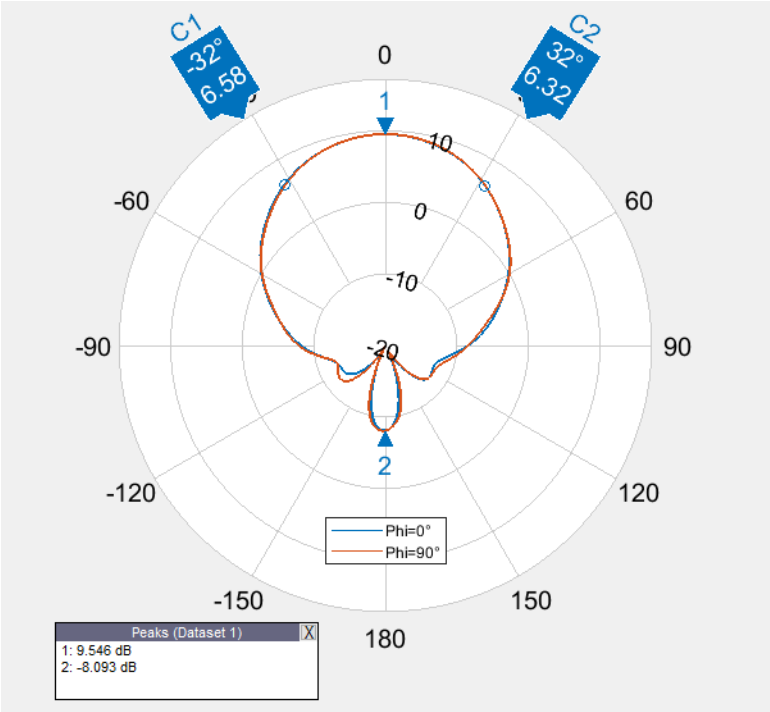

Figure 3.12. Radiation pattern of the unit element for ϕ=0° and ϕ=90° at 3.3 GHz

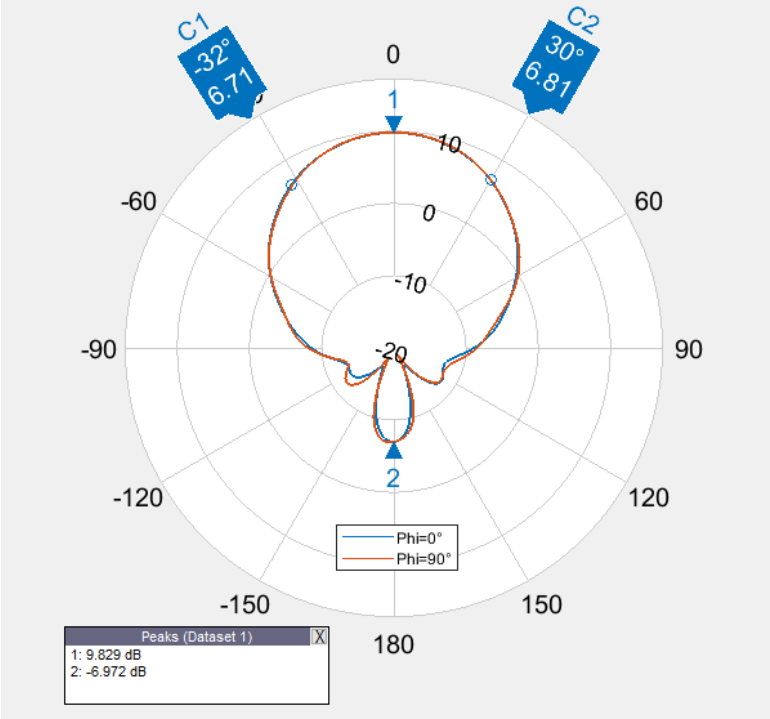

Figure 3.13. Radiation pattern of the unit element for ϕ=0° and ϕ=90° at 3.4 GHz

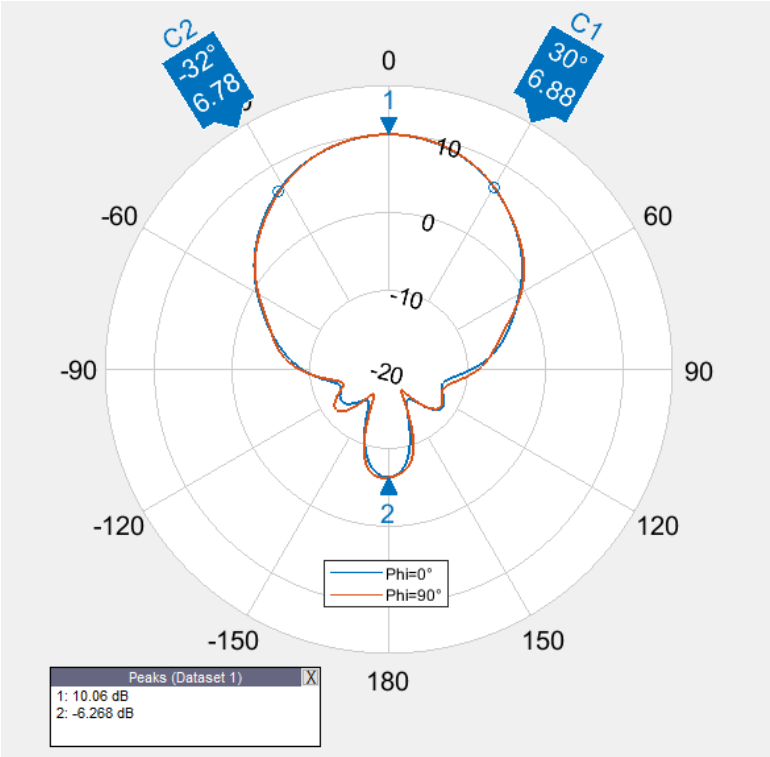

Figure 3.14. Radiation pattern of the unit element for ϕ=0° and ϕ=90° at 3.5 GHz

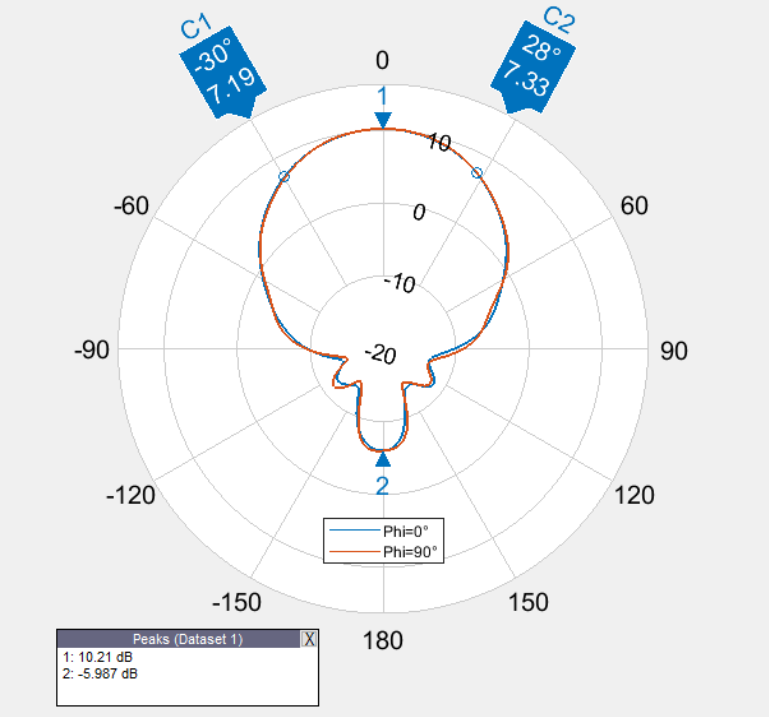

Figure 3.15. Radiation pattern of the unit element for ϕ=0° and ϕ=90° at 3.6 GHz

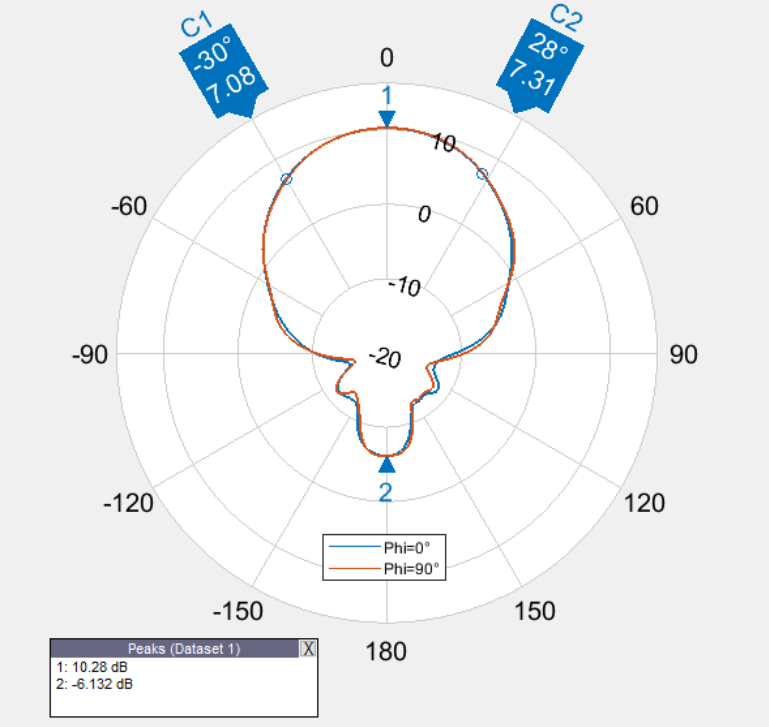

Figure 3.16. Radiation pattern of the unit element for ϕ=0° and ϕ=90° at 3.7 GHz

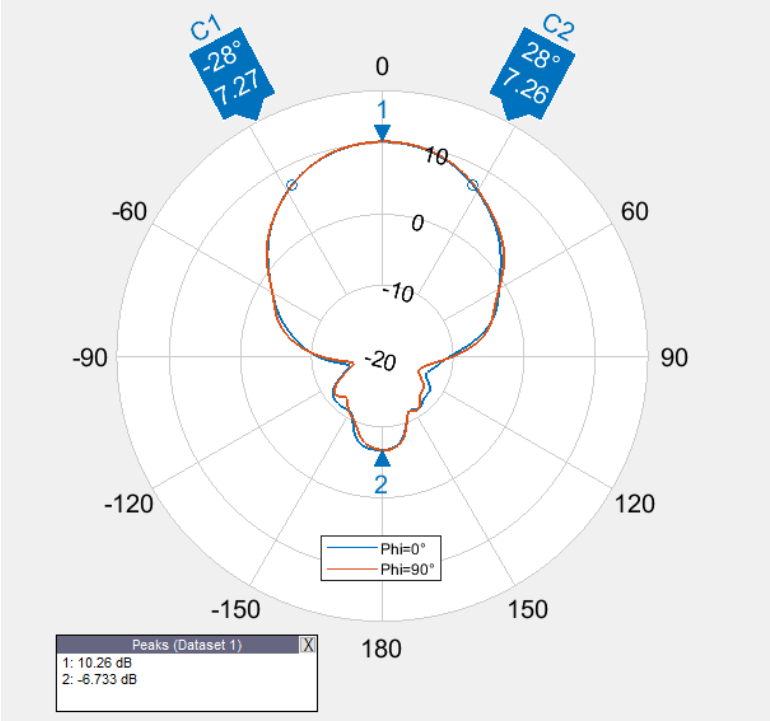

Figure 3.17. Radiation pattern of the unit element for ϕ=0° and ϕ=90° at 3.8 GHz

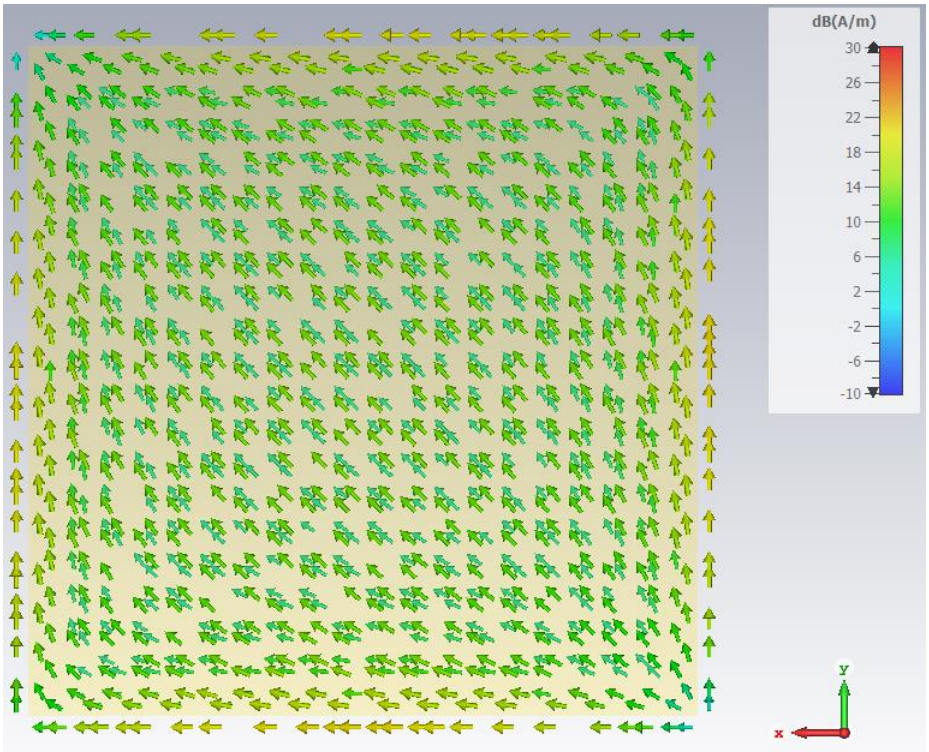

(a) Top patch surface current distribution (Excited with -45° polarization)

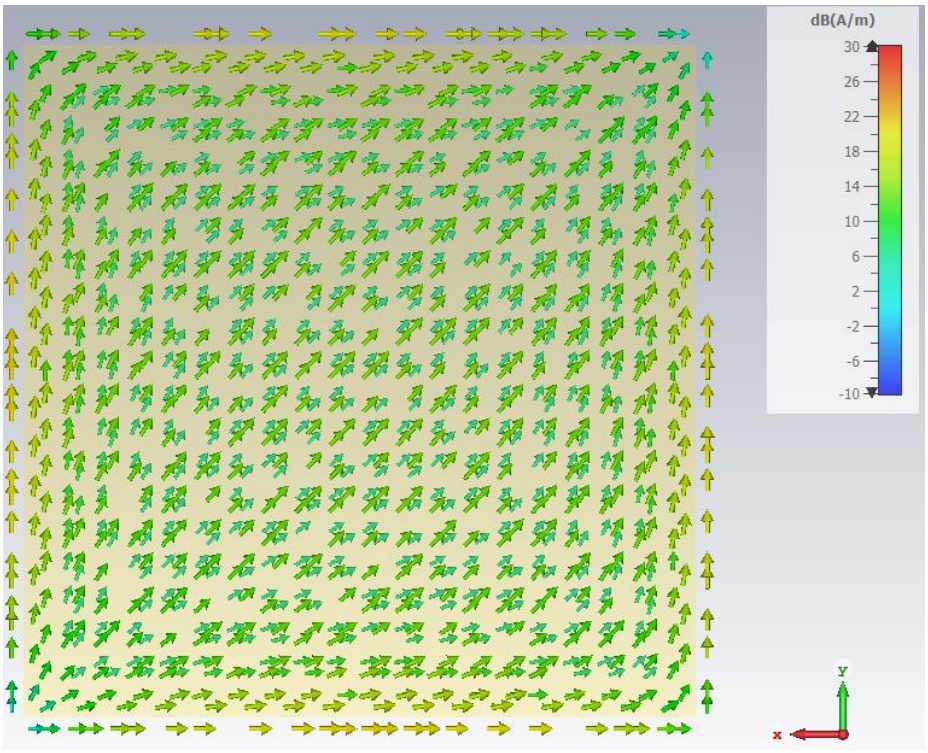

(b) Top patch surface current distribution (Excited with +45° polarization)

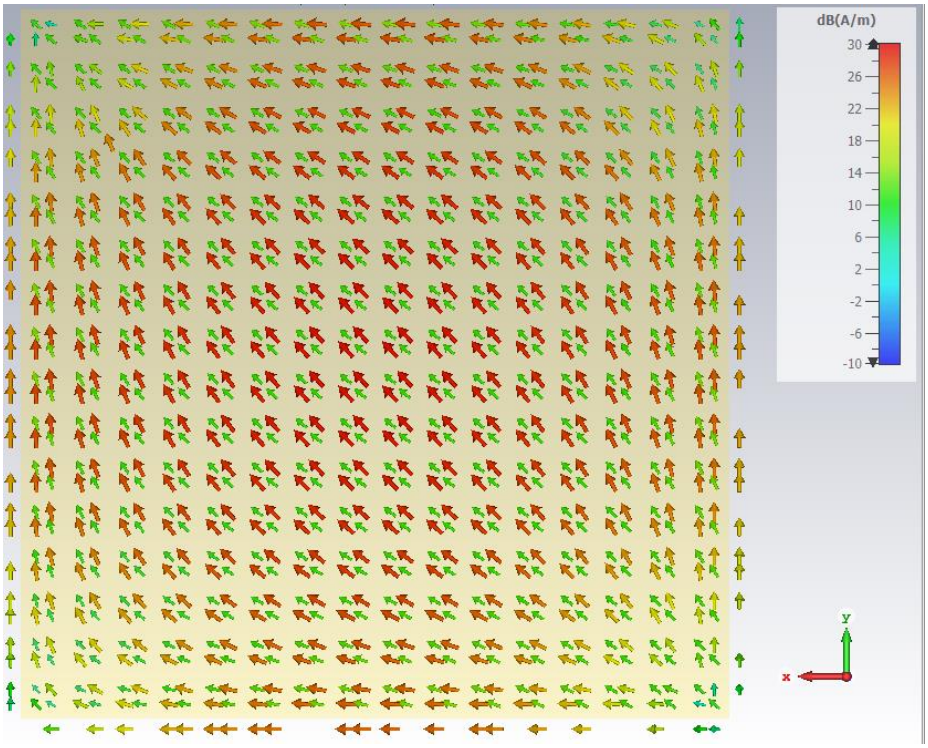

(c) Bottom patch surface current distribution (Excited with -45° polarization)

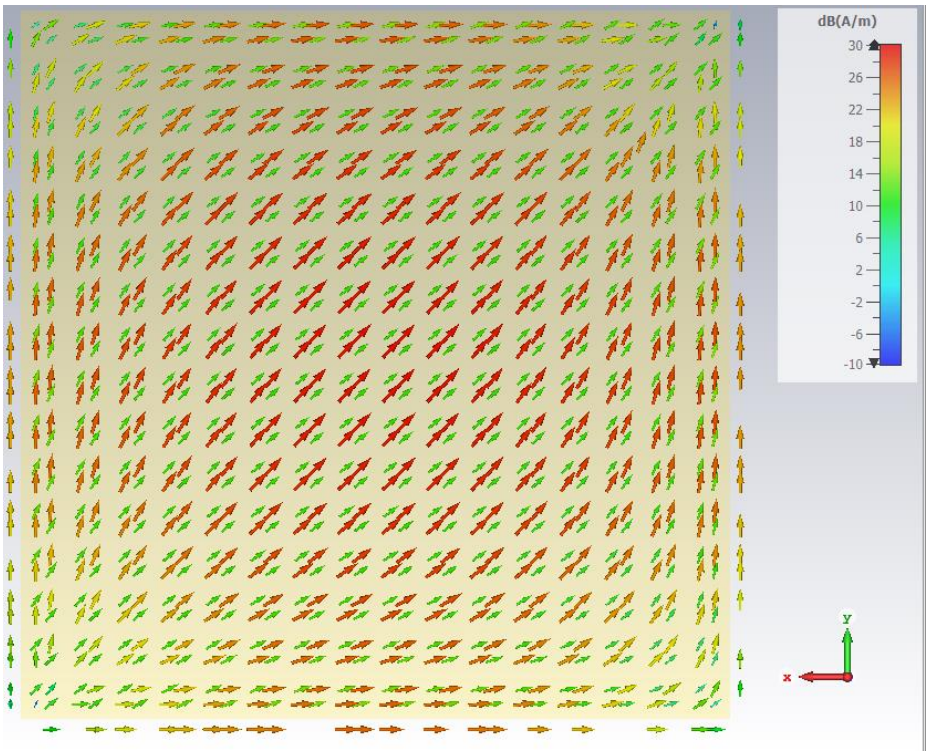

(d) Bottom patch surface current distribution (Excited with +45° polarization)

Figure 3.18 (a)(b)(c)(d). Current distributions on the patch surfaces when excited by two different polarizations

3.2 Prototype Fabrication

After optimizing the antenna parameters through extensive parametric sweeps and obtaining satisfactory results for return loss, isolation, polarization, and antenna pattern from simulation data, the decision has been made to proceed with manufacturing a prototype of the unit antenna element. The values obtained from Table 3.2 are utilized, with the exception of the ground plane size (GND) parameter, which will be implemented as GND=40 mm to minimize substrate usage. The manufacturing process involves using the LPKF ProtoMat S63 prototyper, utilizing a 30 mil thick Rogers RO4350B substrate. The copper foil on the substrate is carefully milled, and the required holes for the SMA connectors are drilled using the LPKF ProtoMat S63 prototyper. Subsequently, two SMA connectors are soldered to the bottom substrate layer from its ground plane side, ensuring a secure and reliable connection. In the final assembly stage, spacers, nuts, and screws made from Nylon 6 material are utilized to assemble all components together seamlessly. The resulting prototype of the unit antenna element is presented in Figure 3.19.

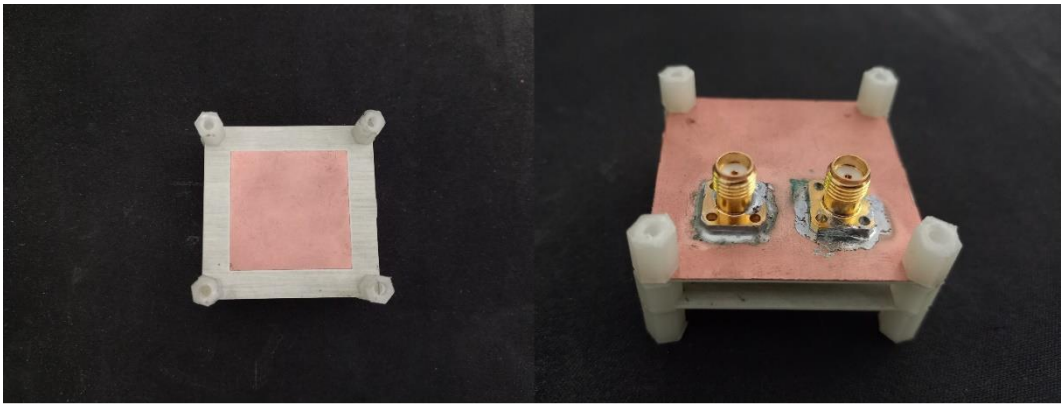

Figure 3.19. Prototype of the unit antenna element

3.3 Measurement Results and Analysis

To validate the performance of the manufactured prototype, S parameters are measured using a vector network analyzer. However, radiation pattern and polarization measurements are not conducted for the unit antenna element individually. Instead, these measurements will be carried out for the complete antenna array once it is assembled.

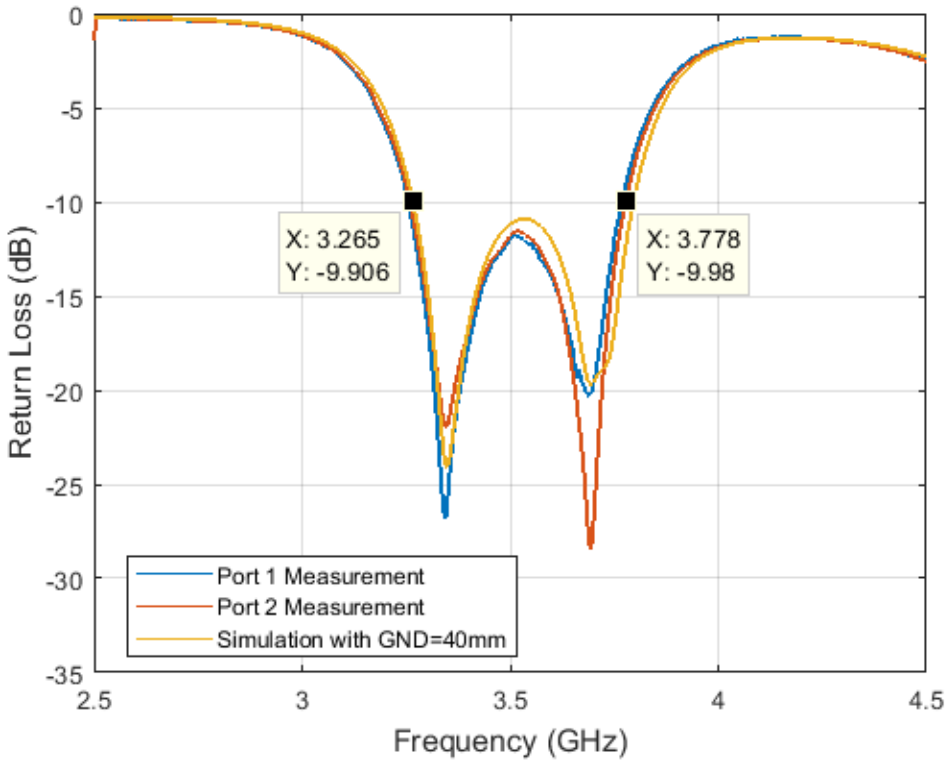

Figure 3.20. Simulation and measurement results comparison of return loss of the prototype

Figure 3.20 illustrates the return loss performance of the manufactured prototype, comparing both simulation and measurement results. It is evident that the measurement and simulation results align closely, except for only a slight shift observed in the higher resonant frequency, indicating a high degree of accuracy in the simulation model. The manufactured prototype boasts a bandwidth of over 500

MHz, covering the 3400-3600 MHz band, and achieves a return loss level of 10 dB. This return loss performance ensures that the antenna is well-suited for 5G applications within this frequency range, providing robust and efficient signal transmission and reception.

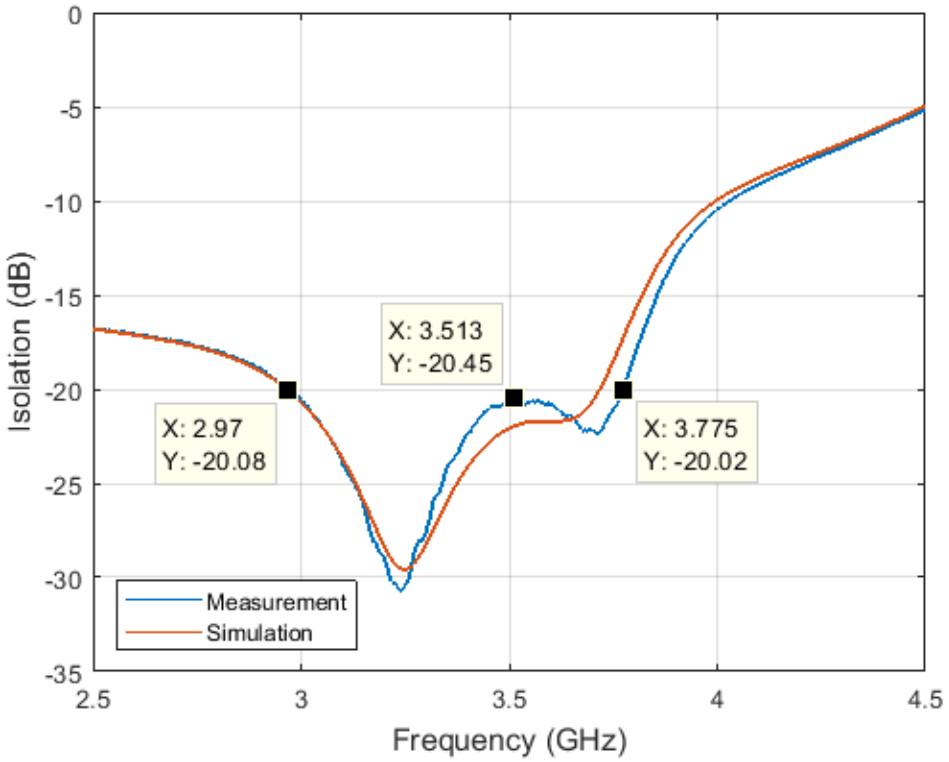

Figure 3.21. Simulation and measurement results comparison of port isolation of the prototype

Similarly, the simulation and measurement results for the port isolation of the manufactured prototype exhibit a good agreement. The prototype demonstrates over 20 dB of isolation between the frequencies 2970-3773 MHz, as depicted in Figure 22. This isolation performance guarantees minimal interference between the input ports, enhancing the ability of the antenna to handle signals with different polarizations effectively.

The consistency between the simulation and measurement results showcases the accuracy and reliability of the antenna design and simulation process. It reaffirms

that the manufactured prototype meets the desired specifications and delivers sufficiently good performance, making it a promising candidate for various 5G applications.

CHAPTER 4

ANTENNA ARRAY DESIGN, FABRICATION and MEASUREMENT RESULTS

In this chapter, the configuration of the antenna array is presented, encompassing the number of unit antenna elements and their respective spacings based on the specifications provided in Chapter 2. Subsequently, the proposed array is constructed in the ANSYS HFSS environment, and comprehensive simulations are conducted to assess its beamforming and beamsteering capabilities. As each unit antenna element cannot be practically excited separately, the chapter will explore how to group antenna elements into sub-arrays and devise the excitation method for these sub-arrays. The design of the feeding network for the sub-arrays is carried out using Keysight ADS. Once the feeding network is integrated into the antenna array and the updated structure is simulated, the chapter will proceed to the prototyping phase, where a physical prototype of the antenna array is manufactured based on satisfying simulation results. Following a detailed section on prototyping, S parameter measurements and radiation pattern measurements in the anechoic chamber are presented and thoroughly analyzed.

4.1 Array Configuration and Design

The initial step in antenna array design involves determining the optimal element spacings and the number of elements. These parameters are determined based on the specifications provided in Chapter 2, which include considerations such as the desired antenna gain and beam scanning ranges. To begin with, element spacings are decided based on horizontal and vertical beam scanning ranges which are specified as -60° to +60° and -15° to +15° respectively in Chapter 2.

In an antenna array, element spacings are limited by grating lobes. Grating lobes occur when the spacing between the elements is too large, causing the array to radiate energy in undesired directions, in addition to the main beam direction. These additional lobes can lead to signal degradation, interference, and reduced antenna performance.

The maximum allowable element spacing, which prevents the occurrence of a grating lobe, is given in [32] by the following equation:

$$d_{max} = \frac{\lambda}{(1 + |\sin \theta_{max}|)} \tag{4.1}$$

In Equation (4.1), d_{max}, θ_{max} and λ represent the maximum allowable element spacing, the maximum beam scan angle measured from broadside direction and the wavelength, respectively. Using Equation (4.1) and beam scanning ranges given in Chapter 2, required element spacings are determined to be approximately 0.54λ and 0.79λ for horizontal (x) and vertical (y) directions, respectively.

Furthermore, when the operating frequency is selected as the center frequency of the 3.4-3.6 GHz sub-band of the n78 band, which is 3.5 GHz, the corresponding element spacing will be approximately 48.28 mm and 67.66 mm for the horizontal and vertical directions, respectively.

After determining the element spacings of the antenna array, the next step is to determine the required number of antenna elements to meet the antenna gain requirement. As specified in Chapter 2, an antenna gain of more than 20dB is necessary. It is advisable to choose the number of elements in both the horizontal and vertical directions as a power of two, as this facilitates the implementation of the antenna feeding network using power dividers. Additionally, selecting a power of two for the element count allows for scalability, where multiple antenna arrays can be combined to create larger configurations. Hence, in both commercially available

products and research studies similar to this thesis, it is common to encounter array configurations like 4×4, 4×8, 8×4, 8×8, 8×16, and so on. Considering the factors discussed above, an 8 by 4 array is a suitable choice, with 8 elements arranged horizontally to facilitate beamsteering in the azimuth direction. The azimuth direction offers a wide 120° beamsteering range, making it ideal for narrower beams without causing issues in comparison to the elevation direction. Conversely, aligning 4 elements vertically results in a broader beam in the elevation direction, which has a narrower beam scanning range of 30°. Additionally, in a scenario involving a base station and user equipments (UE) such as mobile phones, the UEs are typically distributed horizontally around the base station (BS). Therefore, the configuration of 8 horizontal and 4 vertical elements aligns well with this distribution, provided it meets the antenna gain requirement.

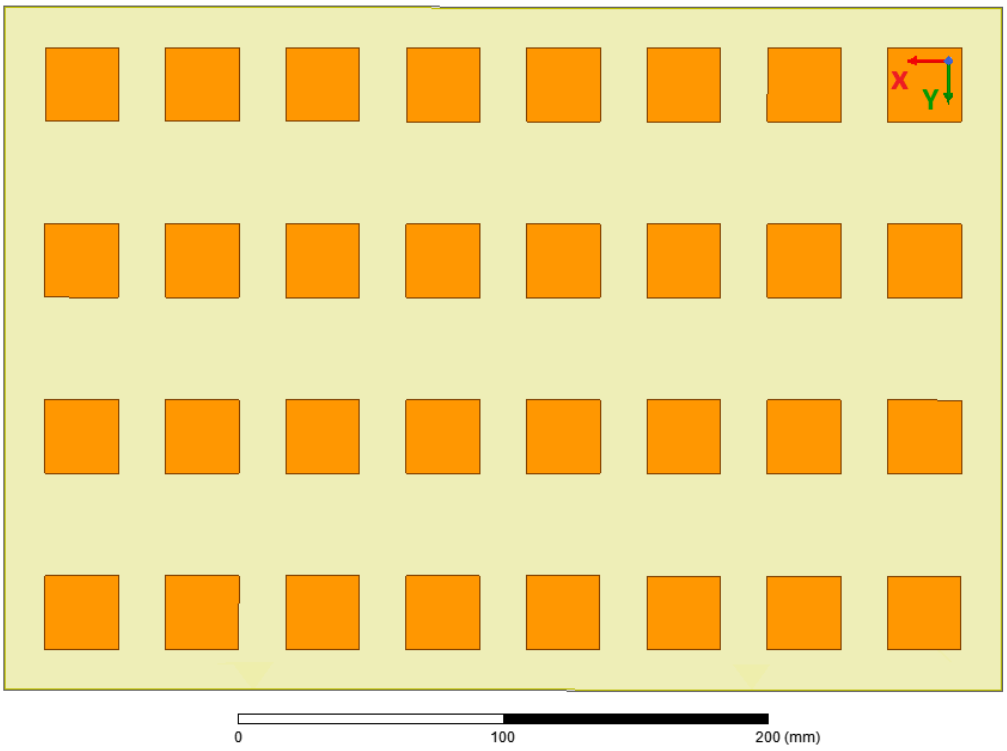

Figure 4.1. Top view of the antenna array

At this point, it is time to validate the proposed element spacing and numbers by creating the model of the antenna array in ANSYS HFSS. The HFSS model of the antenna array can be observed in Figure 4.1. The model shown in Figure 4.1 is simulated in HFSS, utilizing the same simulation setup as described in Chapter 3, with the exception of a larger radiation boundary box due to the increased model size. Additionally, for computational efficiency, a single solution frequency of 3.5 GHz is used to reduce the simulation load. According to the simulation results, the antenna array provides a gain of 22.5 dB at the broadside direction, as depicted in Figure 4.2. This result meets the requirement given in Table 2.2.

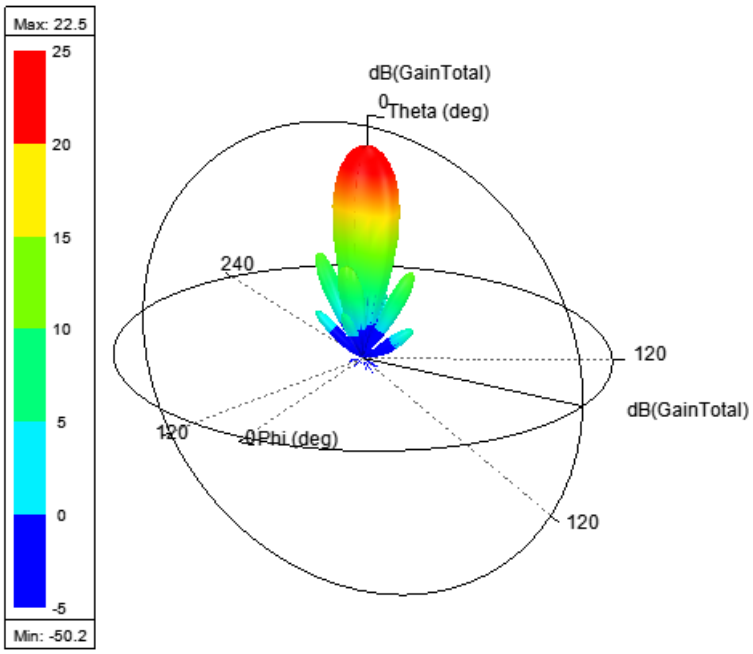

Figure 4.2. Broadside gain of the antenna array

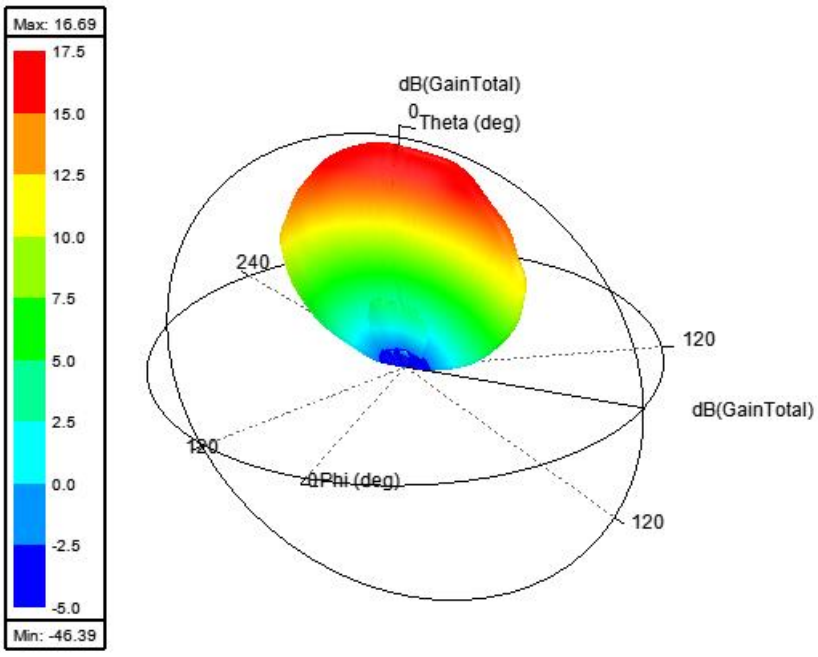

Figure 4.3. Gain of the antenna array when only 2nd row elements are excited

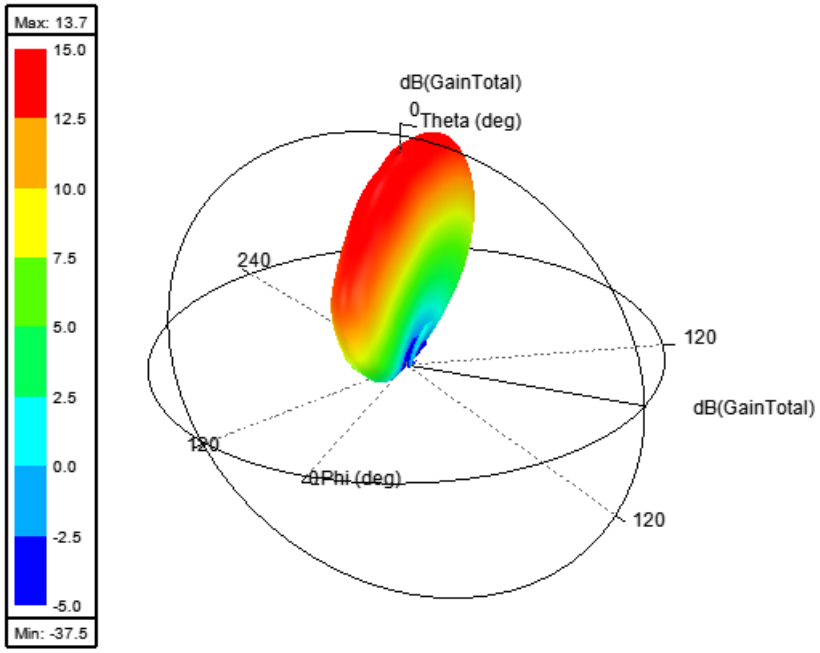

Figure 4.4. Gain of the antenna array when only 4th column elements are excited

As shown in Figures 4.2, 4.3 and 4.4, obtained level of gain is sufficient to fulfill the gain requirement given in Chapter 2. Other important attributes of the broadside gain of the array at 3.5 GHz are as follows: a 12° half-power beamwidth (HPBW) and a 13.5 dB side lobe level at the xz plane, a 14° HPBW and a 13.5 dB side lobe level at the yz plane, and a 28 dB front-to-back ratio. The radiation patterns for 3.5 GHz at the xz and yz planes are shown in Figure 4.5 and Figure 4.6, respectively. Additionally, to demonstrate the beamsteering capability of the array, a progressive phase shift is applied to the antenna elements. The steered beam in the xz plane is presented in Figure 4.7, and the steered beam in the yz plane is shown in Figure 4.8, also corresponding progressive phase shifts between adjacent elements are given in the figure legends..

To further explore the limits of beamsteering, the antenna elements in the horizontal (x) direction are excited with a 168.5° progressive phase shift (phase shift required to rotate the beam to -60°). This results in the main lobe and grating lobe being directed towards -60° and +90°, respectively (Figure 4.9). However, grating lobe is suppressed due to the radiation pattern of the unit element, since radiation pattern of the unit element rapidly decays after +60° in elevation. Similarly, in Figure 4.10, the beamsteering limit in the yz plane is presented, where the main lobe is directed towards +15°, and a grating lobe occurs at -90° with a progressive phase shift of 73.5° between adjacent elements. The same effect is observed in the grating lobe the radiation pattern of the unit element attenuates the magnitude of the grating lobe.

Besides, broadside gain characteristic with respect to frequency is illustrated in Figure 4.11. By increasing frequency, there is a slight increase in the gain from 22 to 23 dB, due to increasing electrical size of the array.

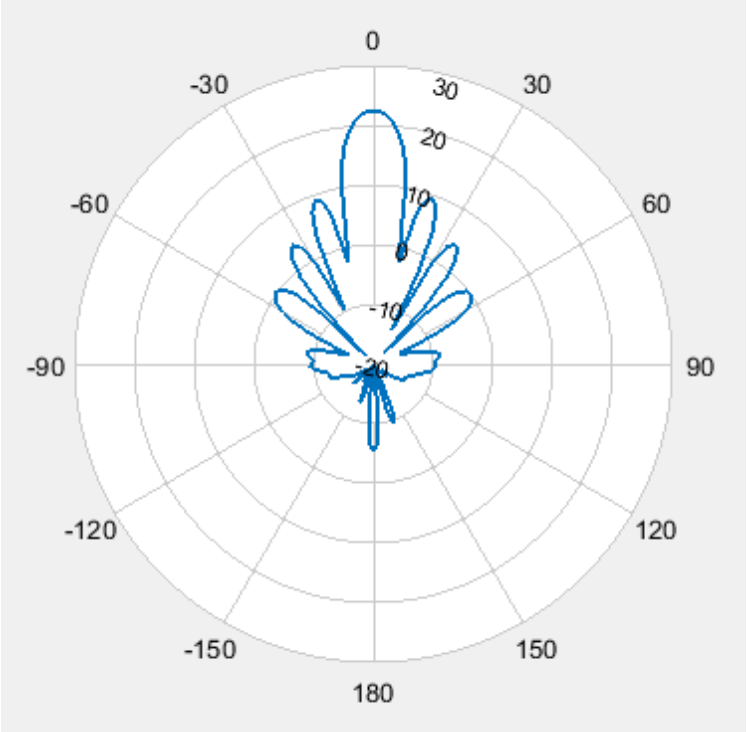

Figure 4.5. Radiation pattern of the antenna array at 3.5 GHz (xz plane)

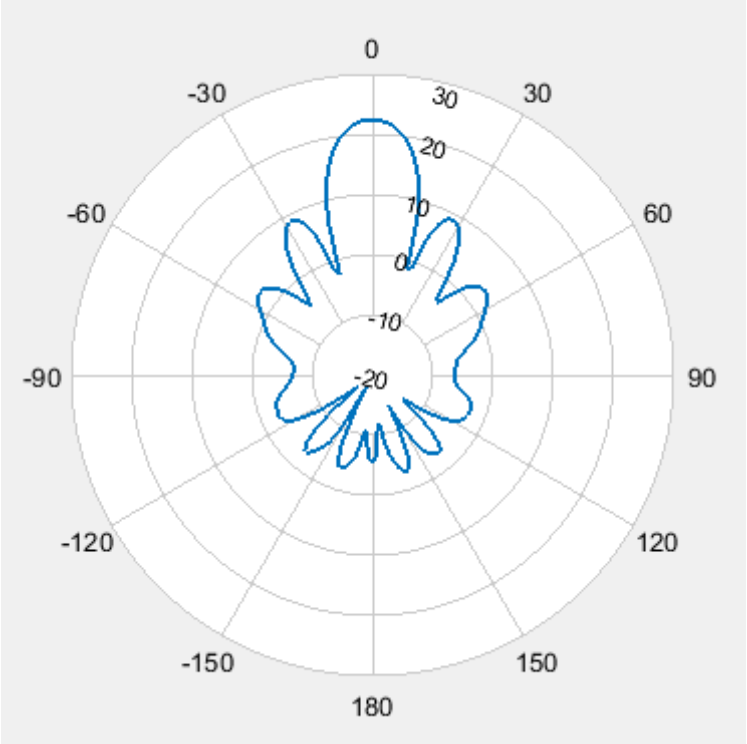

Figure 4.6. Radiation pattern of the antenna array at 3.5 GHz (yz plane)

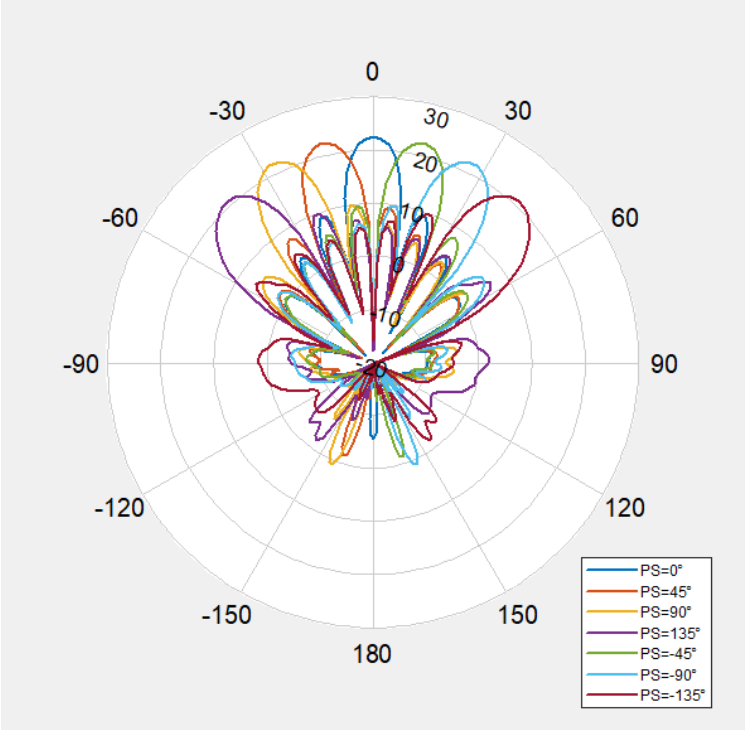

Figure 4.7. Steered beams in xz plane at 3.5 GHz

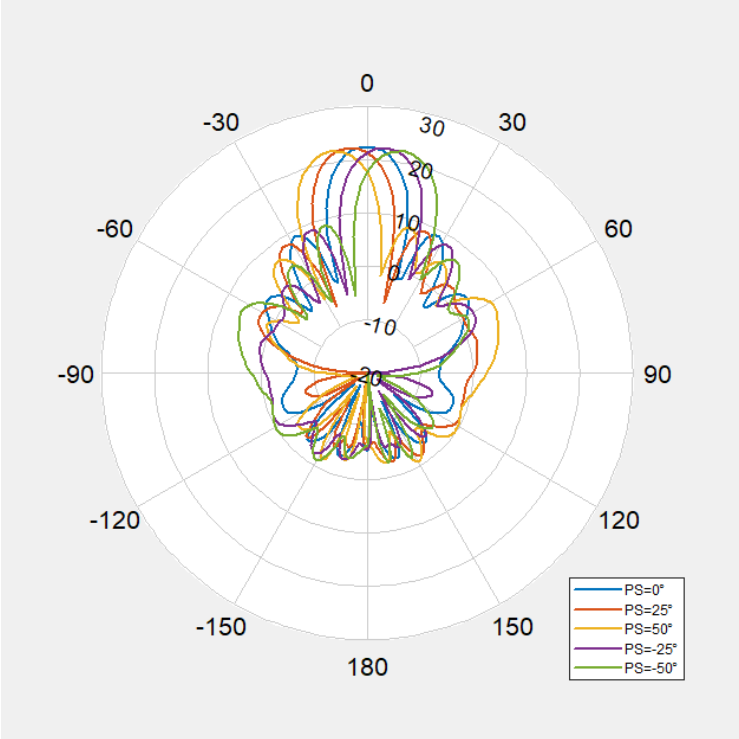

Figure 4.8. Steered beams in yz plane at 3.5 GHz

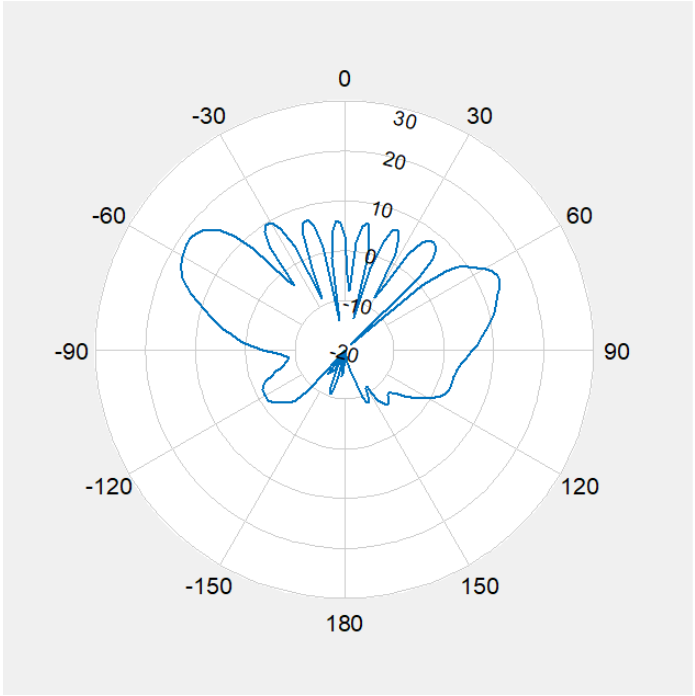

Figure 4.9. Limit of beamsteering in xz plane with 168.5° phase shift between adjacent elements at 3.5 GHz

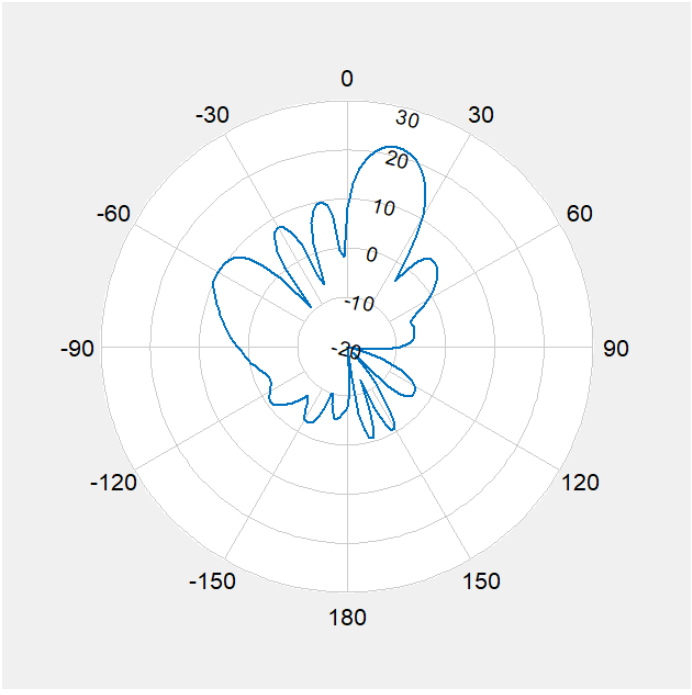

Figure 4.10. Limit of beamsteering in yz plane with 73.5° phase shift between adjacent elements at 3.5 GHz

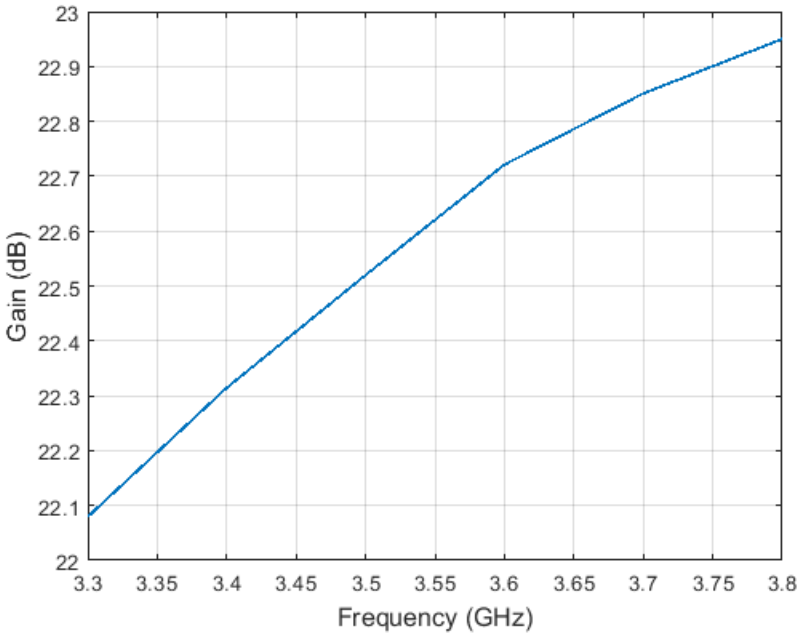

Figure 4.11. Broadside gain change with respect to frequency

4.2 Feeding Network Design

Up to this point, the design and simulation of the individual antenna unit have been executed. Likewise, an antenna array has been constructed and simulated utilizing this particular unit, encompassing a total of 64 distinct ports. Although each of those 64 ports could be fed by radio transmitters independently and organized into alternative configurations in order to facilitate beamforming either along both the xz and yz planes or at intermediate θ and ϕ angles, the comprehensive assessment of all 64 ports within the confines of this thesis is found to be impractical.

Therefore, a decision has been reached to group every set of +45° or -45° polarized ports of 4 vertically aligned elements, which will be powered through a single antenna feeding network. This approach enables the preservation of polarization diversity. Consequently, each distinct grouping of 4 elements, termed a subarray, is linked to 2 separate feeding networks. This arrangement allows for the excitation of 2 distinct polarizations, thereby enhancing performance and capabilities of the array.

To facilitate the implementation of the antenna feeding network, an additional RO4350B substrate layer with a thickness of 10 mils is introduced. This third layer shares a common ground plane with the antenna array, positioned in a back-to-back configuration with the bottom antenna layer (Substrate #1 in Figure 3.3) of the array. The schematic overview of the feeding network is depicted in Figure 4.12, wherein Wilkinson power dividers are interconnected in a collaborative manner. This arrangement involves the concatenation of a first-stage Wilkinson power divider with two successive power dividers to achieve a desired 1:4 power division ratio. Moreover, length-matched transmission lines with a characteristic impedance of 50 Ω are strategically integrated between the stages. This step ensures the alignment of geometrical dimensions between the feeding network and the antennas, contributing to the seamless integration of the components.

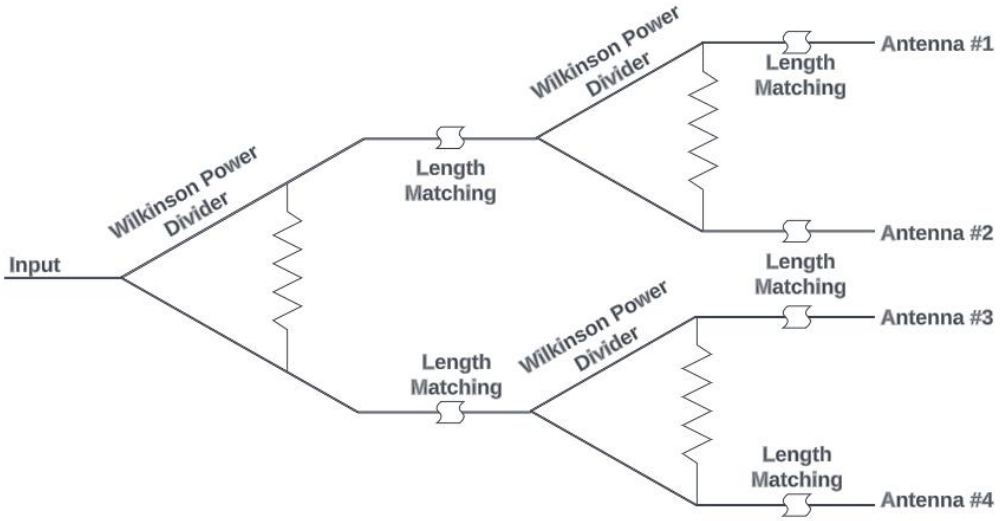

Figure 4.12. Block diagram of the feeding network

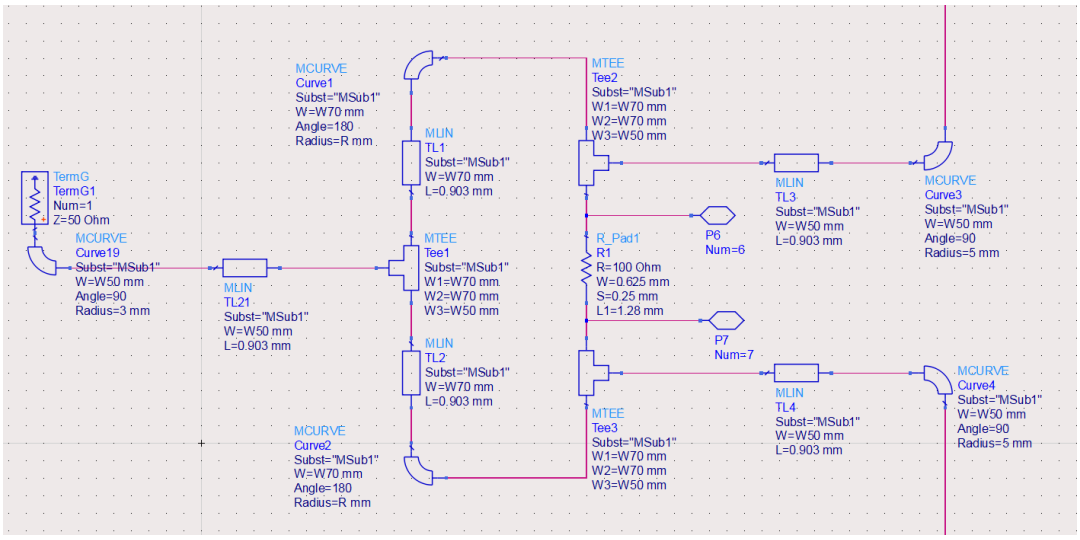

Figure 4.13. Schematic view of Wilkinson power divider

The design process of the proposed feed network and Wilkinson power divider is executed within Keysight ADS. Figure 4.13 presents a schematic representation of a single-stage Wilkinson power divider, illustrating the configuration. The input impedance of the unit antenna element, as extracted from ANSYS HFSS, is imported into Keysight ADS to establish a connection with the output of the feed network. Upon conducting schematic-level simulations and optimizations within Keysight ADS, the designed network is subsequently translated into layout. This facilitates co-simulation using Keysight ADS' MoM (Method of Moments) solver, namely Momentum. A visual depiction of the relevant layout configuration is presented in Figure 4.14, and the resulting simulation outcomes for the antenna loaded feed network are presented in Figure 4.15. As shown in Figure 4.15, a return loss of 10 dB is achieved within the 3.3-3.8 GHz range.

After obtaining satisfactory outcomes within Keysight ADS for the feeding network,

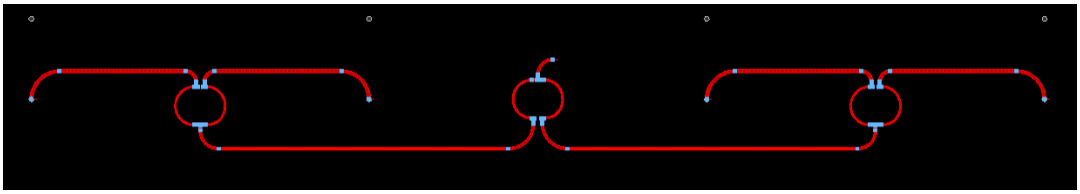

Figure 4.14. Layout view of Wilkinson power divider

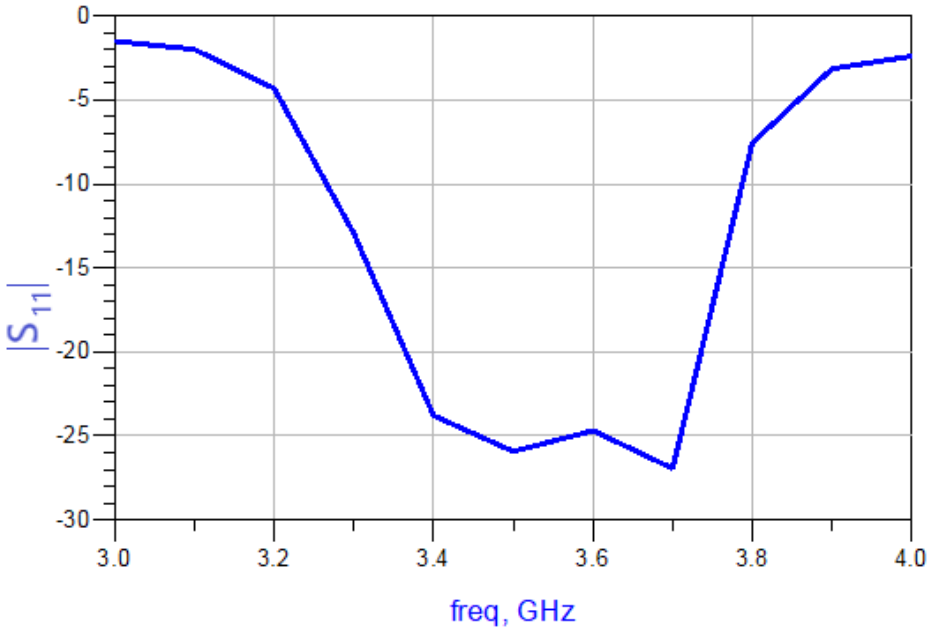

Figure 4.15. Return loss of the antenna loaded feed network

the designed network is subsequently imported into HFSS. The objective here is to integrate this network into the broader antenna array framework. Figure 4.16 provides a top-view portrayal of a single 1×4 sub-array, effectively incorporating the feeding network. This illustration employs transparency for enhanced clarity, depicting the interconnection between the feed network and the antennas. The integration is facilitated through the utilization of metallic vias, ensuring a transition between the feeding network and antennas.

In line with the depiction in Figure 4.16, each 1×4 vertical sub-array is fed by two distinct feeding networks. One serves the +45° polarized ports, while the other corresponds to the -45° polarized ports. This design ensures the proper polarization

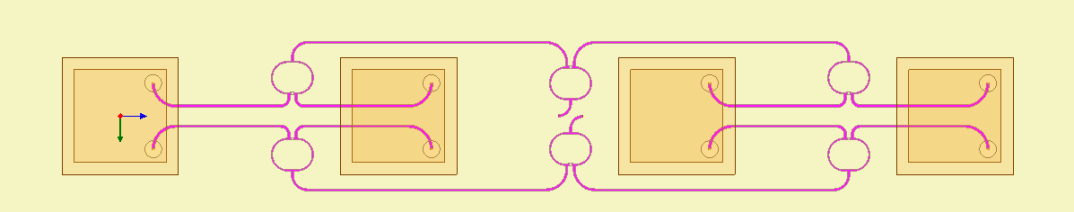

Figure 4.16. Feeding networks for each 1×4 vertically alligned sub-array

alignment. After the integration of the feeding network and the antenna array was completed, the resultant structure undergoes simulations to evaluate its performance and functionality.

Figure 4.17 illustrates the return loss characteristics of the sub-array, along with the reflection coefficient of the individual unit antenna element. Observing Figure 4.17, it becomes apparent that the integration of the feed network did not induce a shift in the operational frequency range of the sub-array. Notably, there is a slight degradation in the reflection coefficient level, however it still remains below the -10 dB threshold within the specified region of interest.

Likewise, Figures 4.18 and 4.19 depict the isolation characteristics of the antenna array. Figure 4.18 illustrates the isolation between two ports with orthogonal polarizations within the same sub-array. Notably, a port isolation exceeding 20 dB is achieved across the 3.3-3.7 GHz range.

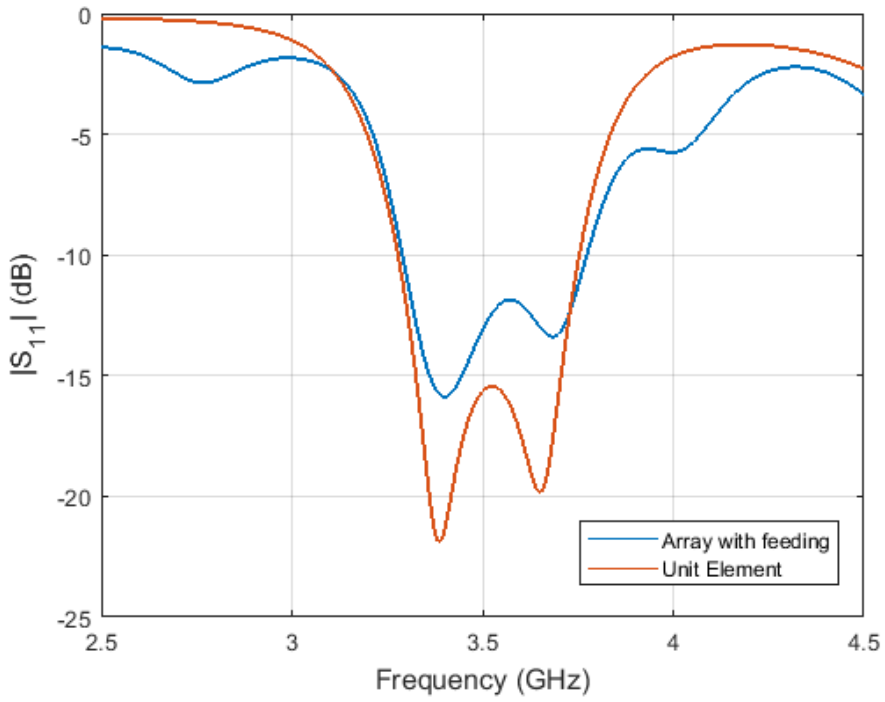

Figure 4.17. Comparison of return loss simulation results of unit element antenna and vertical sub-array with feeding network

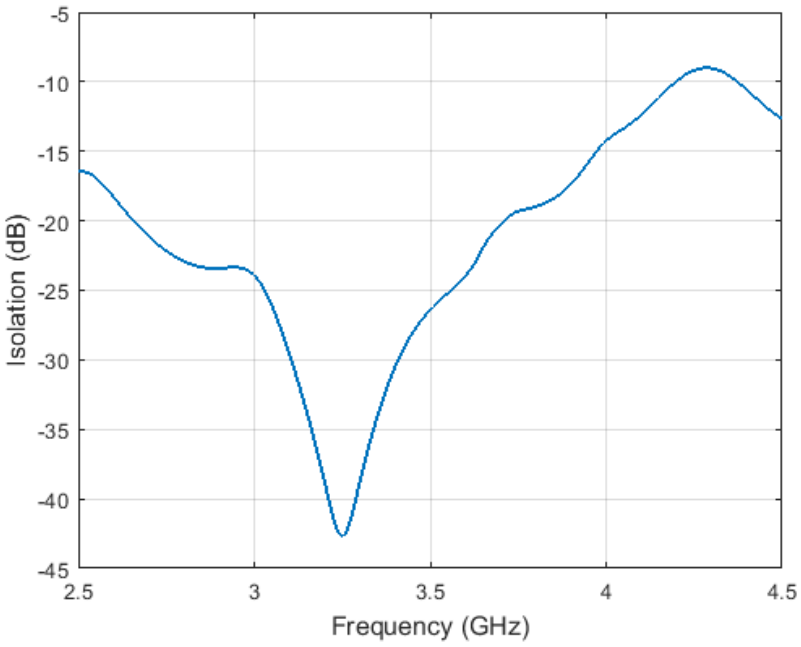

Figure 4.18. Isolation between 2 ports of the same sub-array

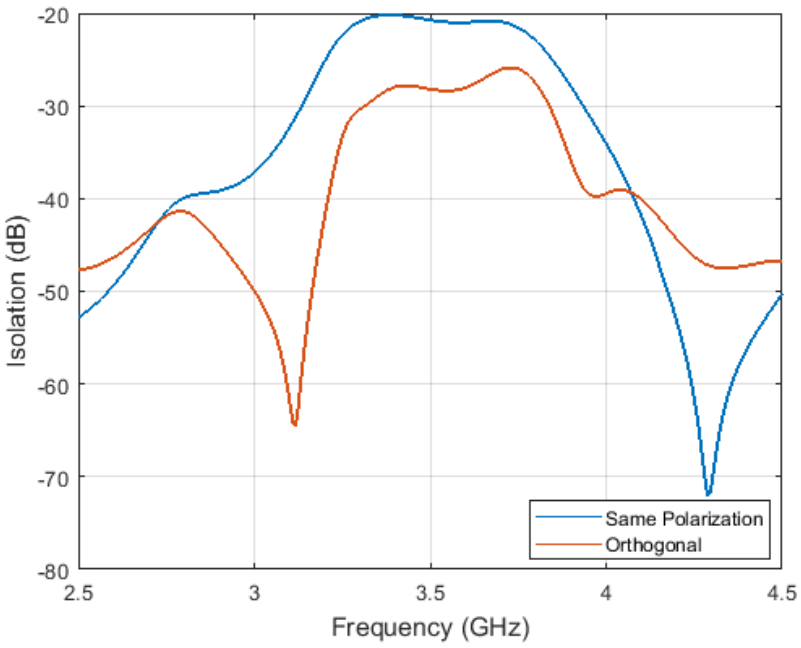

Figure 4.19. Isolation between adjecent sub-arrays for same and orthogonal polarized ports

Figure 4.19 portrays the isolation between neighboring sub-arrays. This depiction reveals two distinct types of isolation. The first pertains to the isolation between ports with the same polarization of the adjacent sub-arrays, measuring at approximately 20 dB. In contrast, the second type of isolation pertains to the orthogonally polarized ports of the adjacent sub-arrays. As anticipated, this second type of isolation is notably stronger, closer to 30 dB.

Finally, in Figure 4.20, the radiation pattern of the 1×4 vertical sub-array with the feeding network at 3.5 GHz is depicted. A comparison with the sub-array gain without the feeding network reveals a decline of approximately 1-1.5 dB in the antenna gain. This reduction is attributed to the insertion loss introduced by the antenna feeding network.

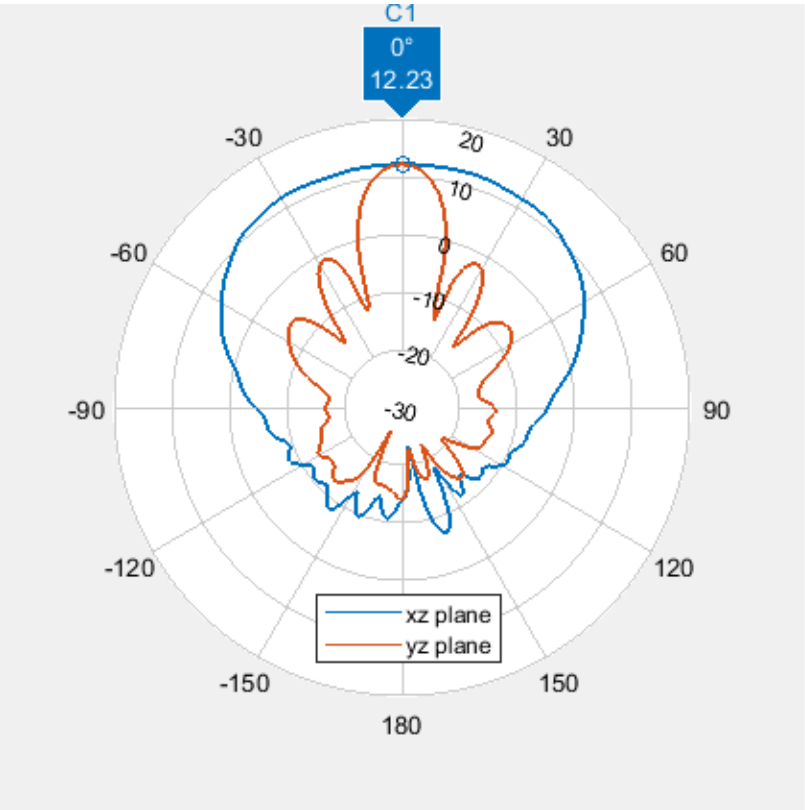

Figure 4.20. Radiation pattern of the sub-array with feeding network

4.3 Prototype Fabrication

Upon achieving favorable outcomes in terms of return loss, isolation, polarization, and radiation pattern from the simulation data, it is decided to advance to the prototype manufacturing stage for the antenna array. However, this time, the array will be fabricated by professional PCB manufacturers, deviating from the previous approach of prototyping using the LPKF prototyper machine. Additionally, the design strategy has shifted towards creating 1×4 vertical sub-arrays and manufacturing them individually instead of manufacturing the antenna array as one piece. This modular approach enables scalability by assembling the desired quantity of sub-arrays as needed.

Furthermore, an aluminum frame/plate is fabricated to facilitate the seamless integration of all the PCBs onto it, offering a unified ground plane for both the bottom antenna layer and the feeding network. Following the assembly of the antenna array using the aluminum frame, along with spacers, nuts, and screws made from Nylon 6 plastic, a total of 16 SMA connectors are soldered to the input ports of the feeding networks. Moreover, two metal fixtures are assembled to the aluminum frame to establish a connection between the antenna array and the radiation pattern measurement setup. Final view of the manufactured antenna array is shown in Figures 4.21 and 4.22.

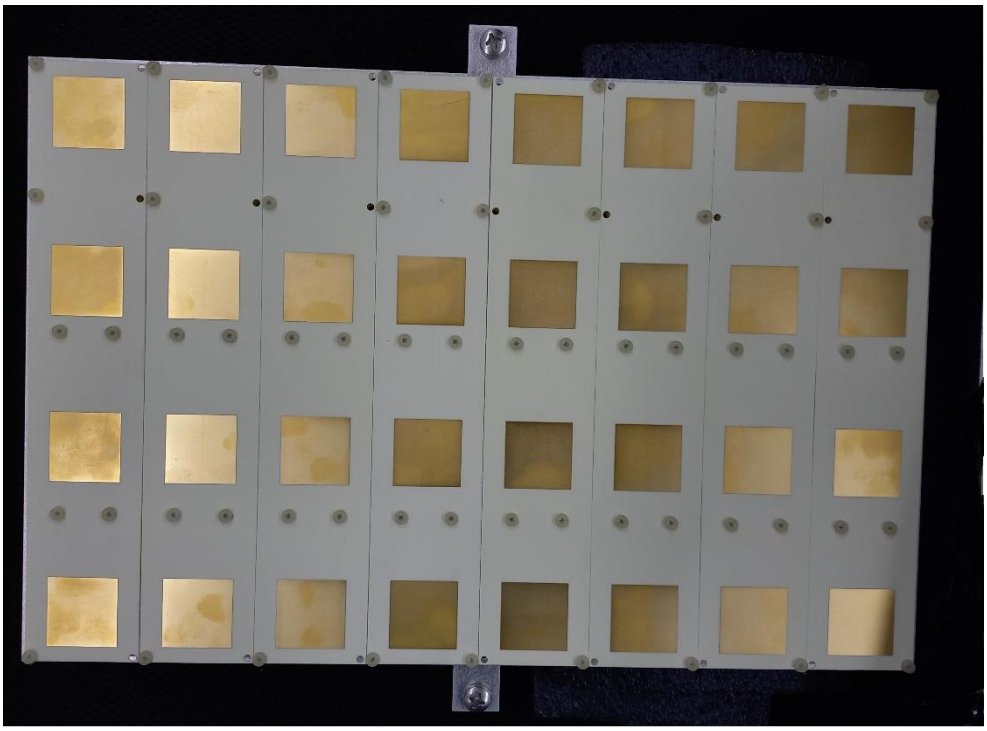

Figure 4.21. Top view of prototype antenna array

Figure 4.22. Bottom view of prototype antenna array

4.4 Measurement Results and Analysis

In this section, S parameters and radiation pattern measurements of the manufactured prototype antenna array will be presented. To ensure clarity and avoid any confusion, port numbers will be assigned and this numbering will be followed throughout the measurements. In Figure 4.23, the input ports of each subarray at the most bottom layer are shown and numbered. Each input port is corporately connected to two Wilkinson's power divider stages. In this way, the input signal is divided into 4 equivalent channels. Each channel is then connected to either +45° or -45° polarized ports of the antenna elements within the same subarray. The corresponding port connections to antenna elements can be seen in Figure 4.24, where pins of the antenna elements fed by the same input port are highlighted and numbered. In this fashion, each subarray is fed by two input ports corresponding to two different orthogonal polarizations, -45° (for odd-numbered antenna ports) and +45° (for even-numbered antenna ports) respectively.

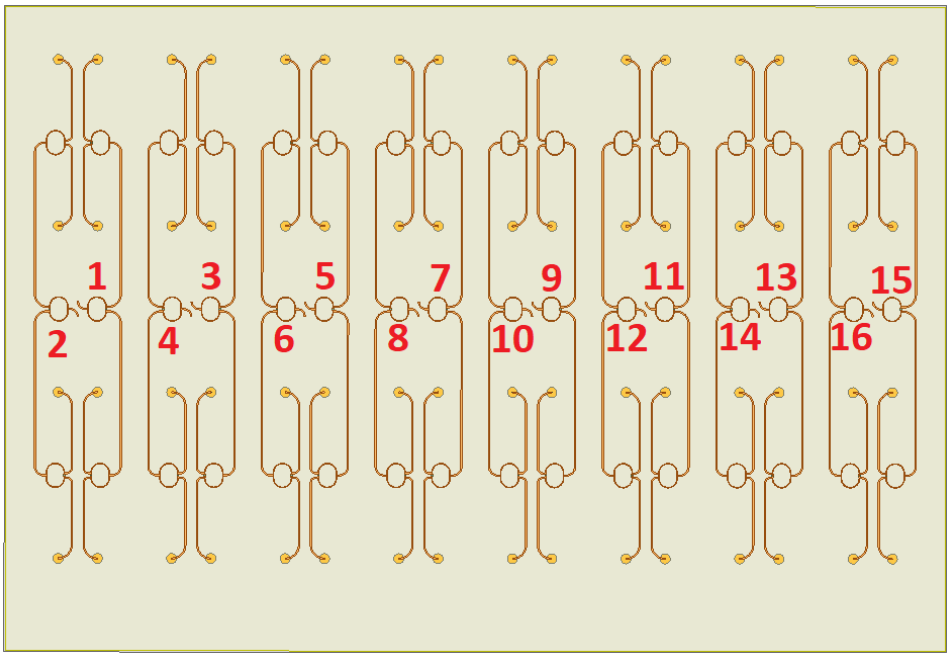

Figure 4.23. Bottom view of port numberings

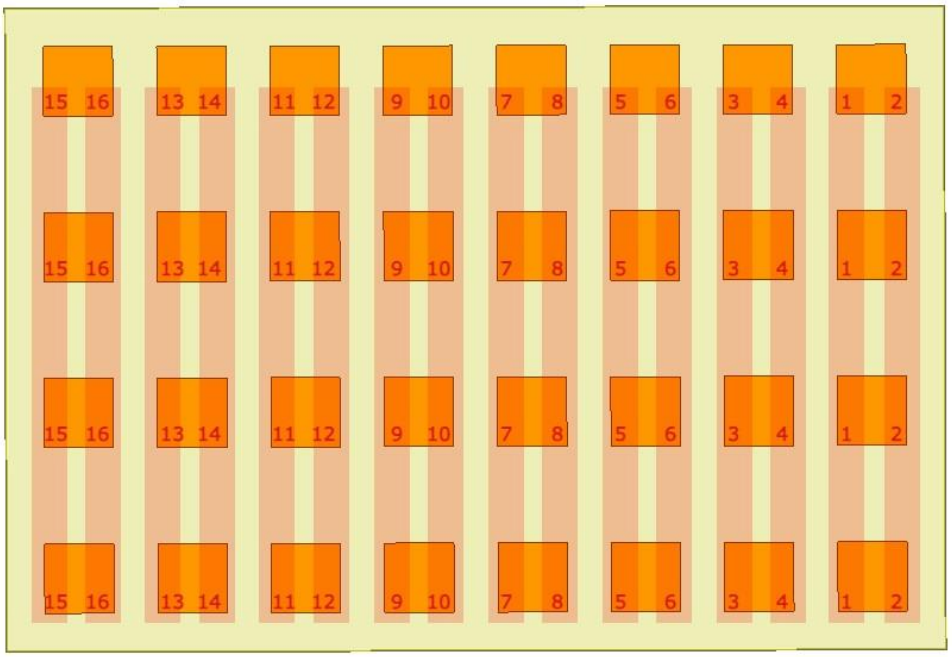

Figure 4.24. Top view of port numberings

Having decided the conventions on port numberings, S parameters measurements are done using a vector network analyzer (VNA). The first parameter to be measured is the reflection coefficients of each input port of subarrays. All the ports except the measured one are always properly terminated before measurements. A total of 16 ports are measured using VNA. Measurement results can be seen in Figures 4.25 to 4.28. As seen in these figures, simulated reflection coefficients are similar to measurement results. Contrary to simulation results, the resonances of the manufactured prototype are deeper which can be due to additional losses in the feed network. Besides, impedance bandwidth is also broader than simulations and covers the 5G n78 band (3300-3800 MHz) completely. This is mainly due to upper corner frequencies being shifted to higher frequencies in the manufactured prototype whereas lower corner frequencies remain in their locations as in the simulations. Corner frequencies in the figures can be seen through marker points. All of these discrepancies between the simulations and measurements are in favor of increasing the antenna array performance.

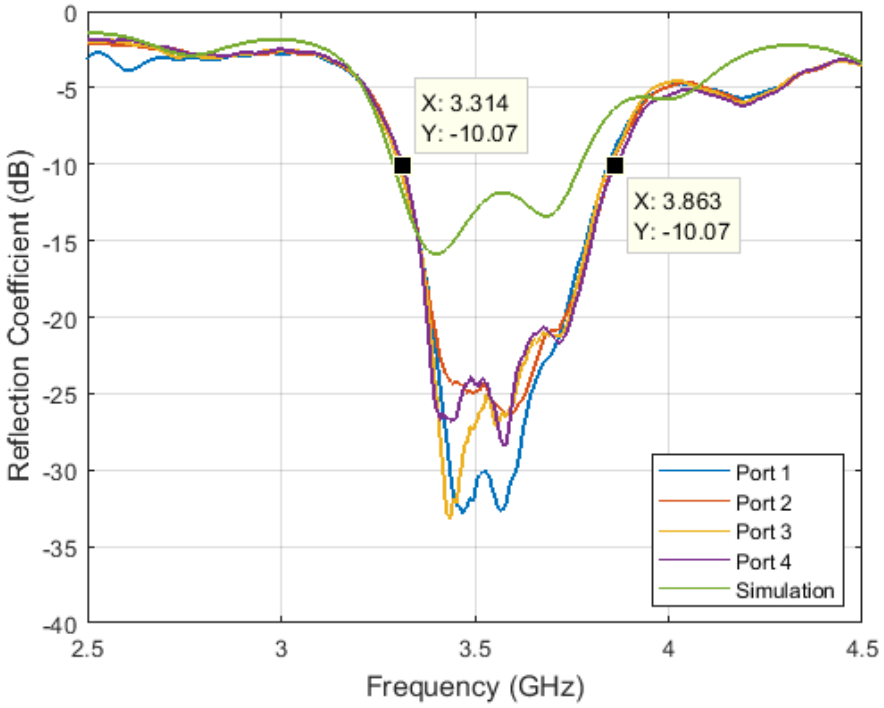

Figure 4.25. Reflection coefficient measurement results for port 1 to 4

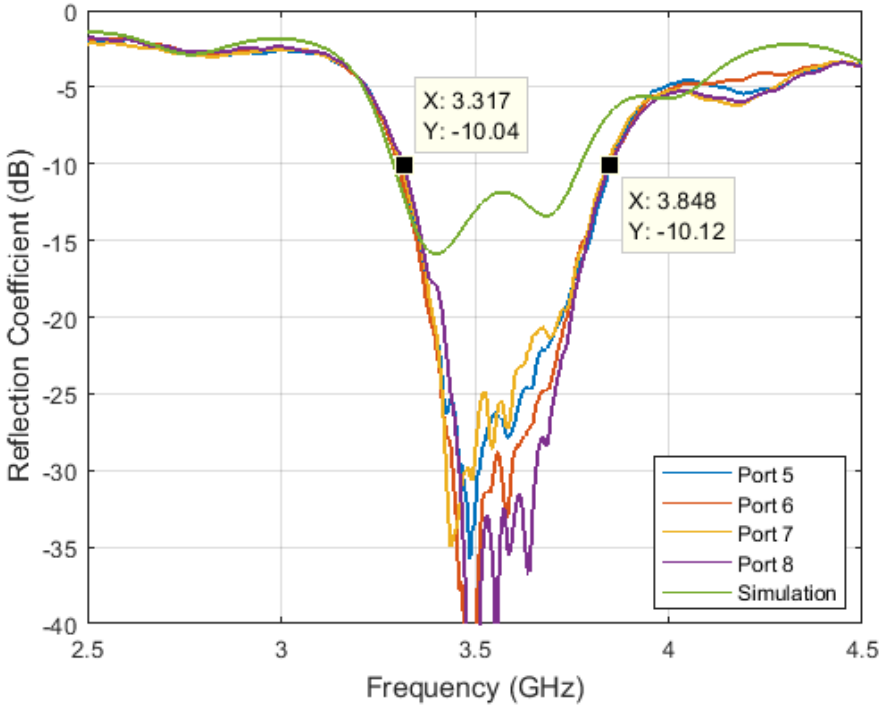

Figure 4.26. Reflection coefficient measurement results for port 5 to 8

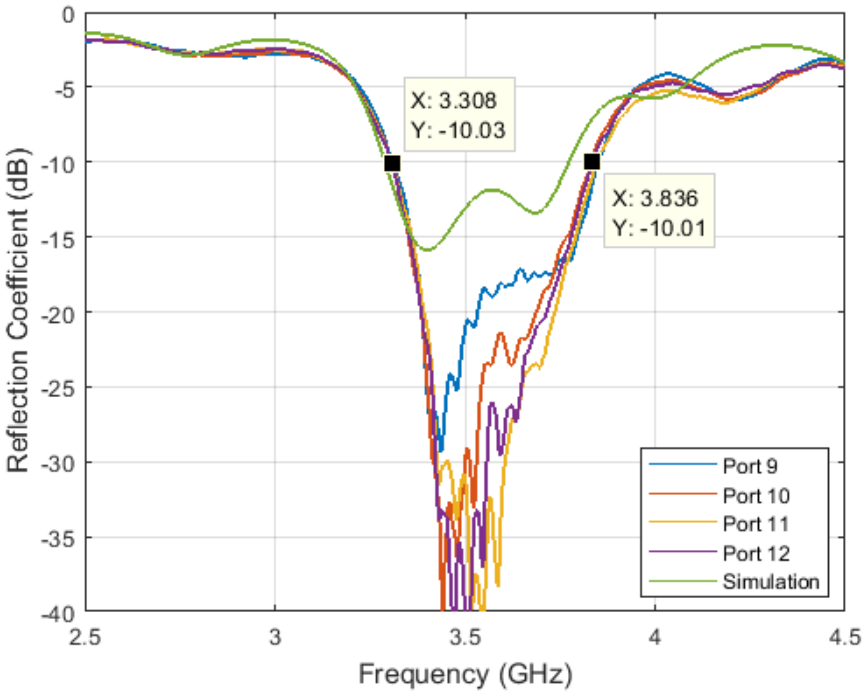

Figure 4.27. Reflection coefficient measurement results for port 9 to 12

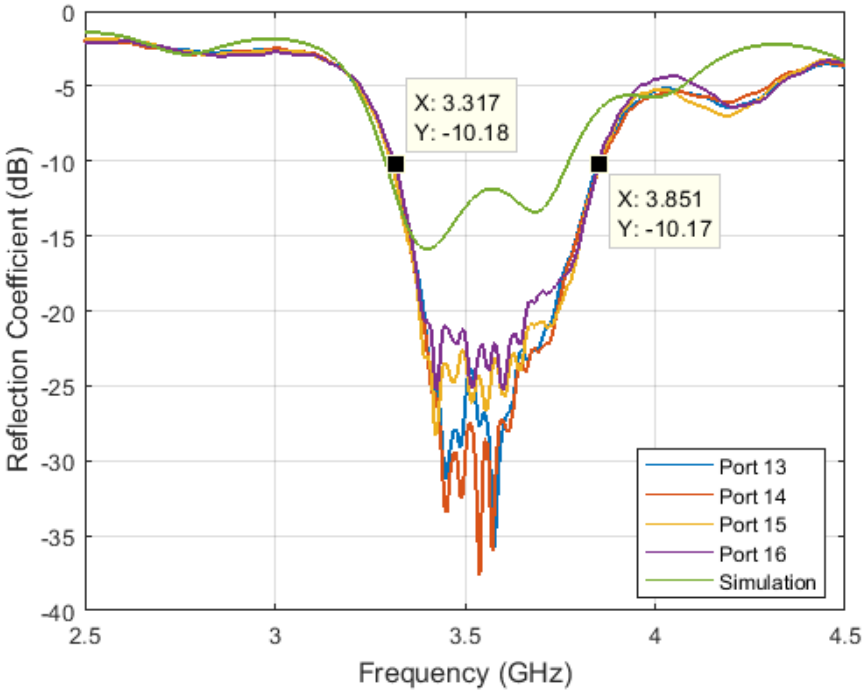

Figure 4.28. Reflection coefficient measurement results for port 13 to 16

Following the reflection coefficient measurements, another series of tests are carried out to assess the isolation between the input ports of the antenna array. Essentially, there are two distinct types of isolation within this antenna configuration. The first type pertains to the isolation between two different, orthogonal polarized ports that are connected to the same subarray. The measurement results for this isolation type are presented in Figure 4.29. In accordance with the simulation results, the isolation between these two orthogonal polarized ports exhibits its negative peak around 3.2 GHz. However, measurement results show a shift in this negative peak around 100-200 MHz. Notably, an isolation level of over 20 dB is achieved within the frequency range of approximately 3000 MHz to 3700 MHz. This isolation performance proves to be satisfactory, particularly within the context of the 5G n78 band, which operates within the frequency span of 3300 MHz to 3800 MHz.

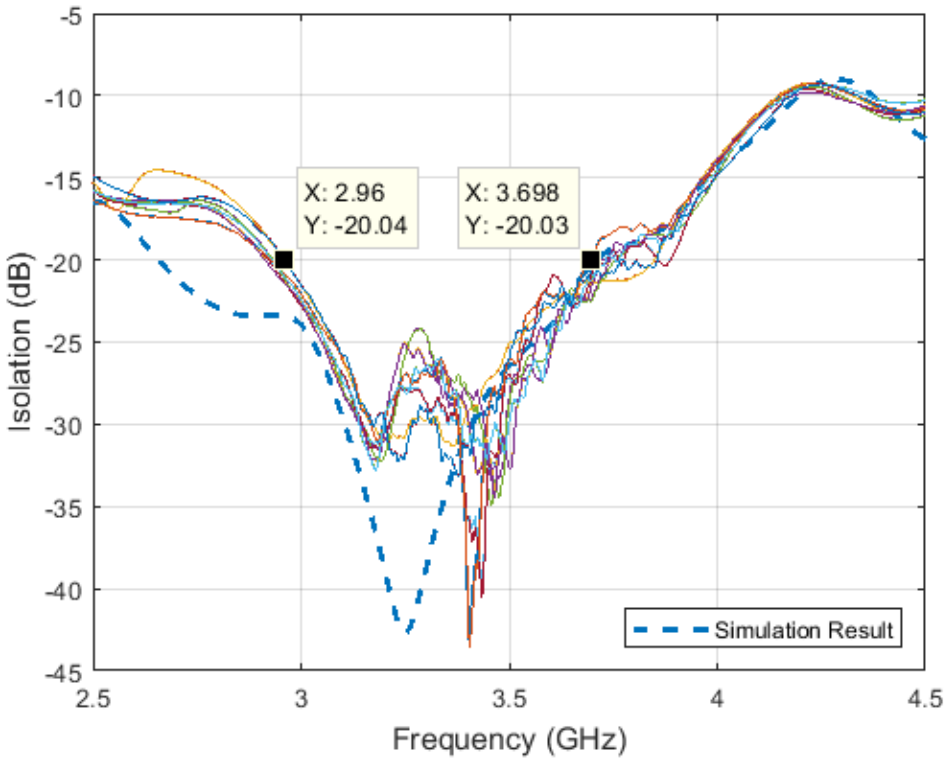

Figure 4.29. Isolation between orthogonal fed ports connected to the same sub-array

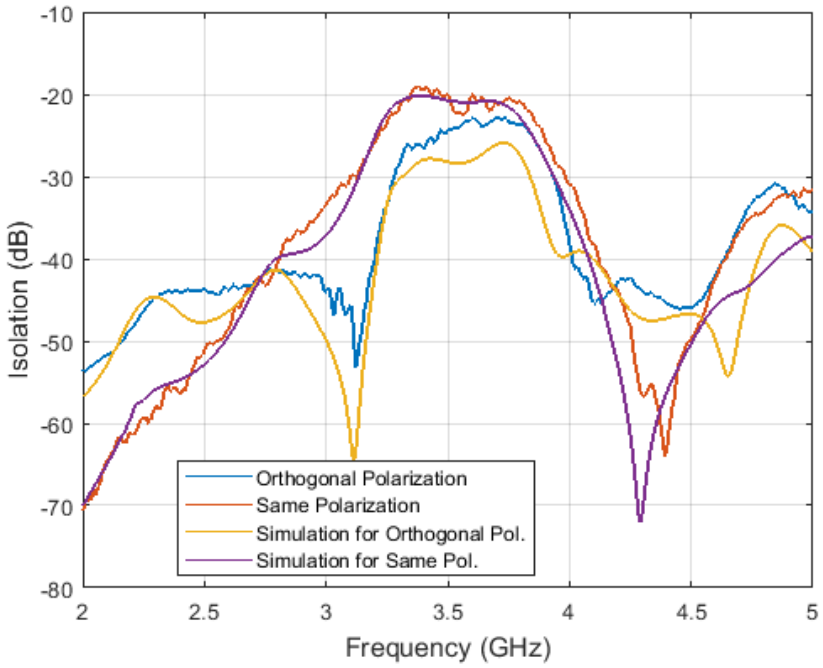

Figure 4.30. Isolation between adjacent subarrays (Between port 7 and port 10 (orthogonal polarization) and also between port 8 and port 10 (same polarization))

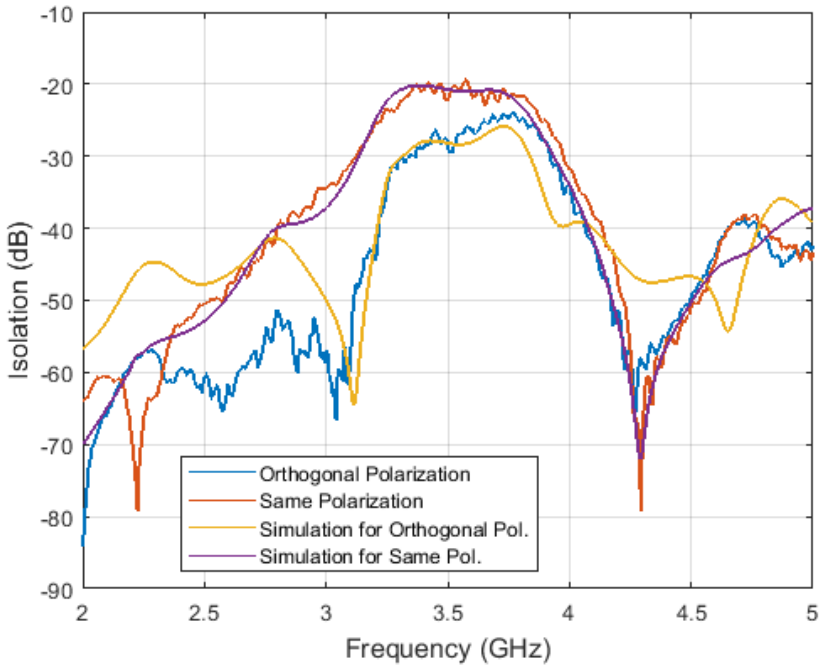

Figure 4.31. Isolation between adjacent subarrays (Between port 14 and port 15 (orthogonal polarization) and also between port 14 and port 16 (same polarization))

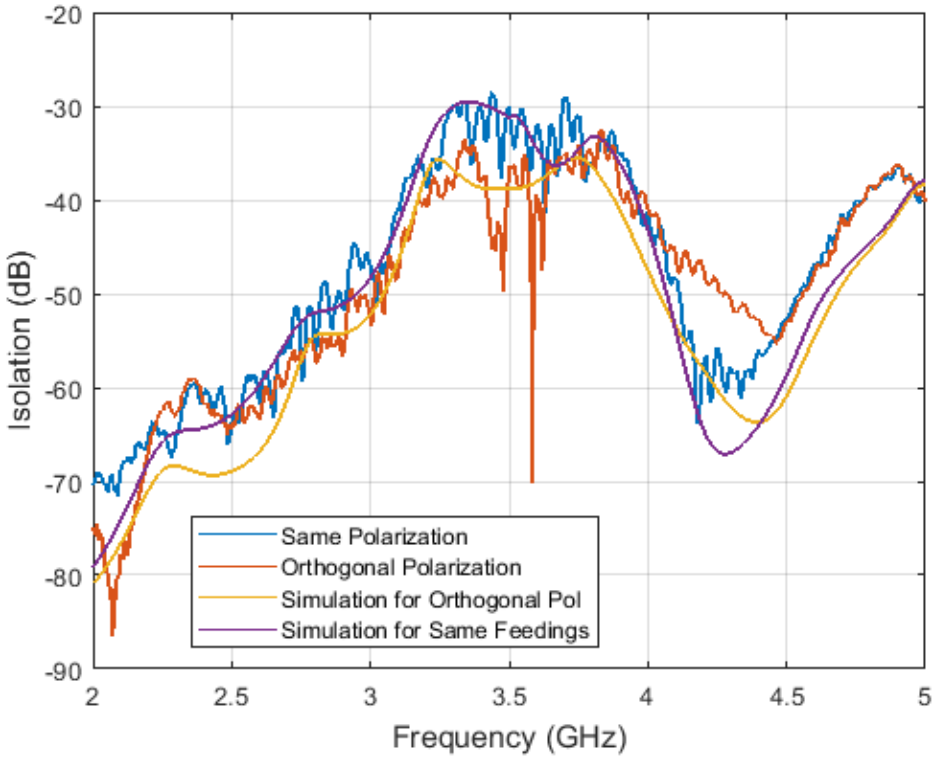

Figure 4.32. Isolation between far adjacent subarrays (Between port 11 and port 15 (orthogonal polarization) and also between port 12 and port 15 (same polarization))

The second type of isolation being examined is the isolation between adjacent subarrays. In this scenario, the input ports that are measured can either be the same polarized ports or orthogonal polarized ports. The measurement results for this type of isolation are presented in Figures 4.30 to 4.32. For reference, please consult to Figures 4.23 and 4.24 for port numbering. In Figure 4.30, the measurement results depict the isolation between port 8 and port 10, as well as the isolation between port 7 and port 10. It is worth noting that the isolation achieved between orthogonal feedings (port 7 and port 10) is significantly higher compared to the isolation between port 8 and port 10 (same polarized feedings). Furthermore, the measurement results closely align with the simulation curve. The isolation level remains below the -20 dB line, except for a small region around 3300 MHz. Although this slight violation occurs at the edge of the band of interest (3300-3800 MHz), it is considered tolerable as it does not excessively exceed the -20 dB limit line. Similar trends are

observed in Figure 4.31, which presents the measurement results for isolations between port 14 - port 15 and port 14 - port 16. Notably, the curves in this figure exhibit even more desirable behavior as they remain completely below the limit line. Additionally, these curves align well with the simulation results.

One additional set of measurement results is presented in Figure 4.32, focusing on the isolation between port 11 and port 15, as well as the isolation between port 12 and port 15. In this particular case, the examined subarrays are not adjacent to each other, but rather, there is an additional subarray between them. This configuration increases the distance between the subarrays under examination and leads to an improved isolation performance. As illustrated in Figure 4.32, the isolation curves remain below the -30 dB line. Similar to the previous cases discussed, there is an agreement between the simulation and measurement results for this configuration, as well. The measured isolation levels align with the simulated values, indicating that the anticipated performance is consistent with the actual measurements.

In conclusion, the measurement and simulation results demonstrate a consistent and satisfactory agreement. Overall, the S parameter measurements obtained from the manufactured prototype of the antenna array exhibit positive and promising characteristics. As a result, the proposed design proves to be a strong candidate for 5G applications in the n78 band, particularly when considering the S parameter measurements. The absence of major discrepancies between the measurement and simulation results highlights the reliability and accuracy of the prototype. This alignment between the two sets of data reinforces the confidence in the performance of the antenna array design.

In addition to its S parameters, the radiation characteristics of the antenna array are of paramount importance. To evaluate radiation characteristics, anechoic chamber of Middle East Technical University Department of Electrical and Electronics Engineering - Ayaslı Research Center is utilized. Figure 4.33 illustrates the antenna array during radiation pattern measurements in the anechoic chamber.

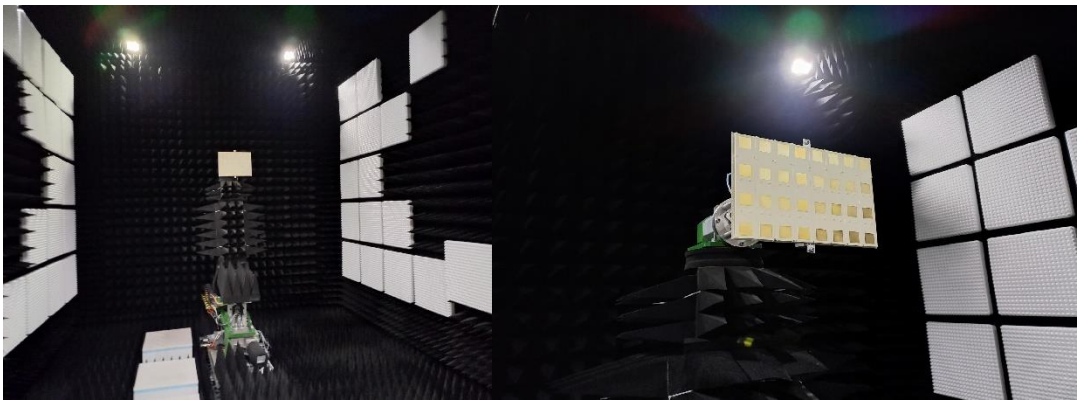

Figure 4.33. Radiation pattern measurements in the anechoic chamber

To begin with, just before radiation pattern measurements of the prototype, a reference standard gain horn (SGH) antenna is measured whose gain characteristics are provided. SGH and the prototype are located at the same point as receiving antenna during measurements and transmitting antenna is the same at the both cases. In this way, since the distance between transmitting and receiving antenna is the same at both cases and the gain of the SGH is known, array gain is found. All of the following figures are presented with the corresponding measured gain values instead of being presented as normalized patterns. Secondly, the polarization of the antenna array is confirmed through antenna pattern measurements as the array is rotated in the ϕ direction (with the z-axis serving as the rotation axis). As depicted in Figure 4.34, the maximum antenna gain is achieved when the antenna array is rotated by 45° in the ϕ direction. This observation confirms the polarization of the antenna. Hence, it is established that the antenna elements possess the anticipated slant polarization, consistent with the outcomes of the simulation results.

To ease the measurement process, the inherent symmetries of the antenna array will be utilized. As evident from Figures 4.21 - 4.24, the antenna array exhibits symmetry along the x-direction. This symmetry is reflected in pairs such as port 1 and port 15, port 2 and port 16, and so forth. Utilizing on this symmetry, the required number of measurements can effectively be reduced by half. The presence of this symmetry is evident in Figures 4.35 - 4.38, where a comparison between the co-polarized and

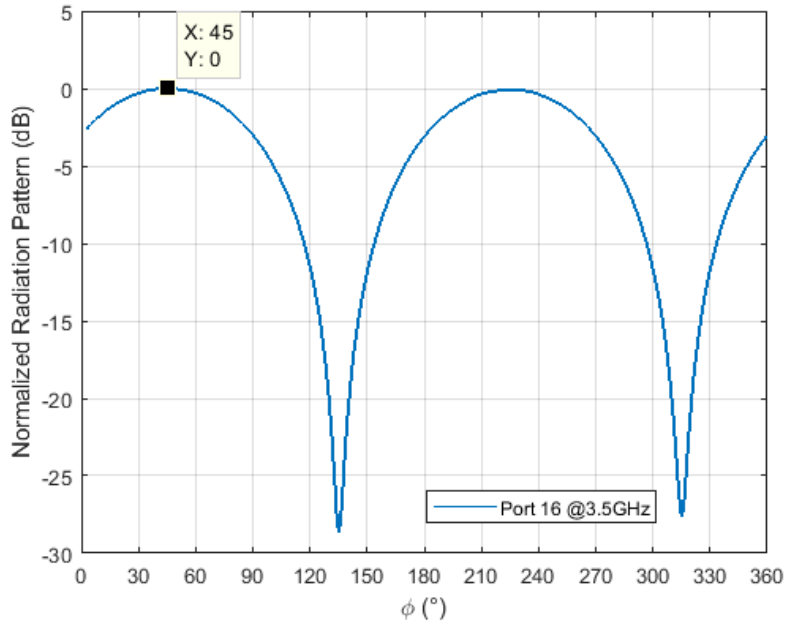

Figure 4.34. Normalized antenna radiation pattern measurement with varying polarization

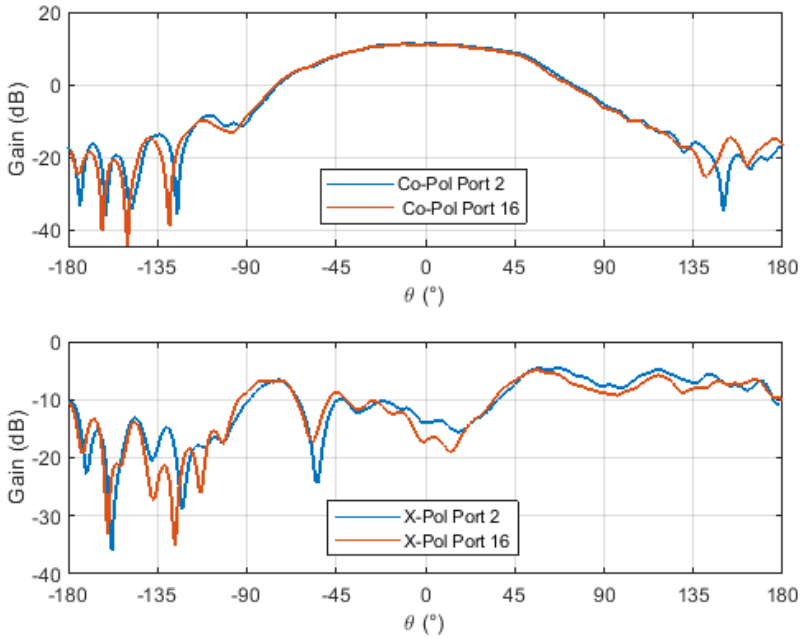

Figure 4.35. Comparison of radiation pattern measurements of port 2 and port 16 for ϕ=0° plane at 3.5GHz

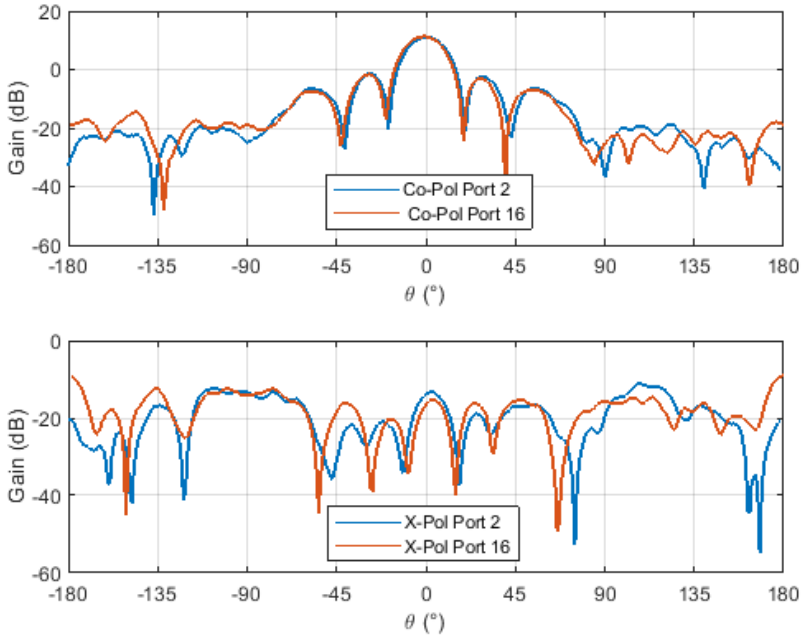

Figure 4.36. Comparison of radiation pattern measurements of port 2 and port 16 for ϕ=90° plane at 3.5GHz

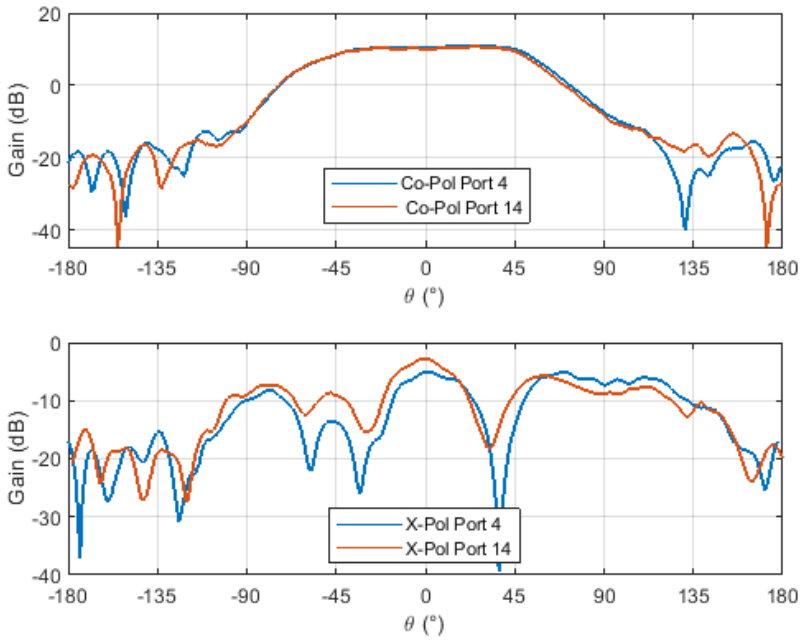

Figure 4.37. Comparison of radiation pattern measurements of port 4 and port 14 for ϕ=0° plane at 3.5GHz

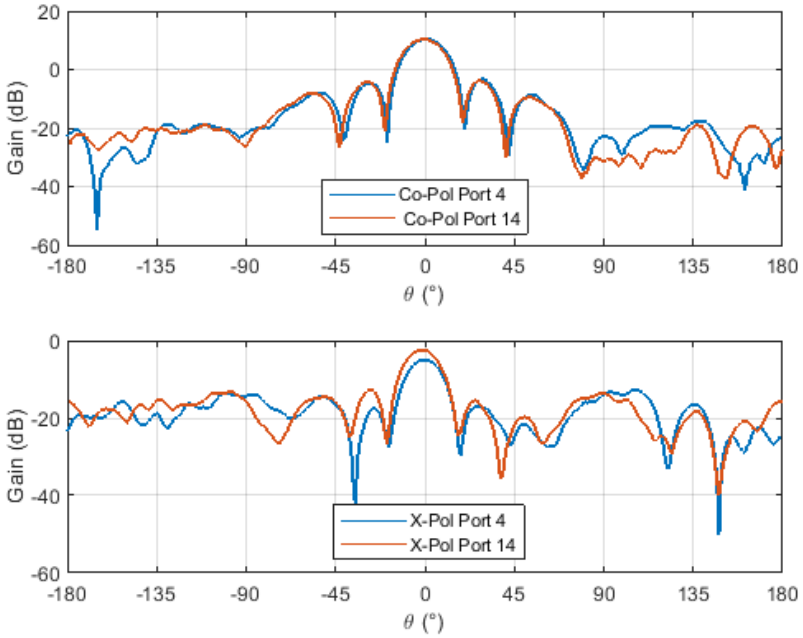

Figure 4.38. Comparison of radiation pattern measurements of port 4 and port 14 for ϕ=90° plane at 3.5GHz

cross-polarized radiation pattern measurement results of port 2 and port 16, as well as port 4 and port 14, can be observed for ϕ=0° and ϕ=90° planes. Although, the resemblance between the co-polarized patterns is particularly pronounced since the measured gains are significantly higher; the curves depicted in Figures 4.35 – 4.38 exhibit a remarkable similarity to their correspondents.

Upon recognizing the symmetry property of the antenna array, it has been determined that radiation pattern measurements pertaining to sub-arrays on the left-hand side of the antenna array would suffice, owing to the inherent symmetry of the configuration. To achieve this, radiation pattern measurements were conducted for ports 9 through 16. A comparison between simulation and measurement results for ports 12, 14, and 16 is presented in Figures 4.39 through 4.44 in which co-polarized and cross-polarized radiation patterns are given for ϕ=0° and ϕ=90° planes at 3.5 GHz.

Several observations can be made regarding the simulation and measurement results. Firstly, there is an additional 1 to 1.5 dB of loss evident in the co-polarization measurement results when compared to the simulation outcomes. This disparity could stem from insufficient accuracy in the simulation setup or, more likely, the assembly process of the antenna array, which might introduce new losses related to SMA connector transitions and the transition from the feed network to the antenna element.

Secondly, it is noteworthy that the side lobe and null locations exhibit remarkable similarities between the measurement and simulation outcomes. This alignment is a gratifying validation of the agreement between the two sets of results. Additionally, the co-polarized results exhibit a higher degree of accuracy in the simulation outputs, which is understandable considering their dominant and more potent influence on the radiation characteristics. This, in turn, leads to fewer simulation errors for calculating co-polarized components.

Finally, another notable observation is that measurement and simulation results exhibit a notably accurate alignment, particularly in the vicinity of the broadside region, generally corresponding to areas where $\theta<90°$ and $\theta>-90°$. However, beyond this range (where $\theta>90°$ and $\theta<-90°$), the precision of the simulations experiences a reduction. This discrepancy mainly arises from the simulation setup, where the offset distance of the radiation box is deliberately minimized in the -z direction (pertaining to the back lobe of the antenna, which is of lesser significance compared to the main lobe). This setup choice is intended to enhance simulation efficiency by reducing computational resource utilization and simulation duration associated with a larger radiation box.

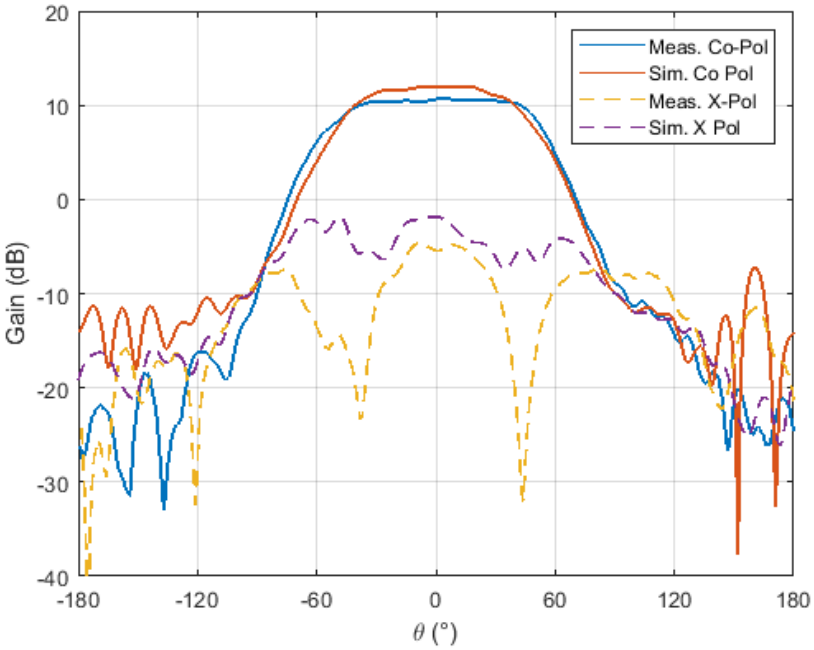

Figure 4.39. Simulation and measurement results of radiation pattern of port 12 at ϕ=0° (3.5 GHz)

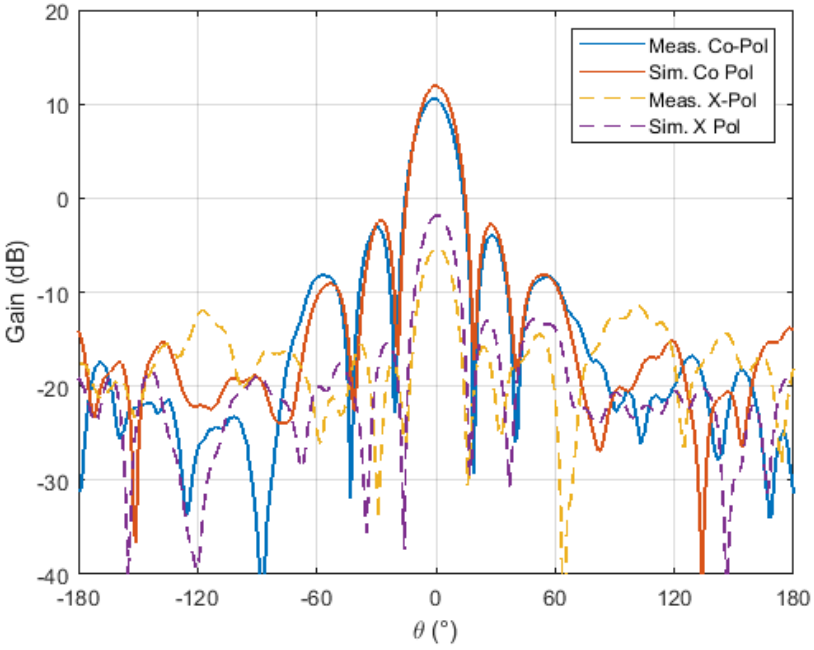

Figure 4.40. Simulation and measurement results of radiation pattern of port 12 at ϕ=90° (3.5 GHz)

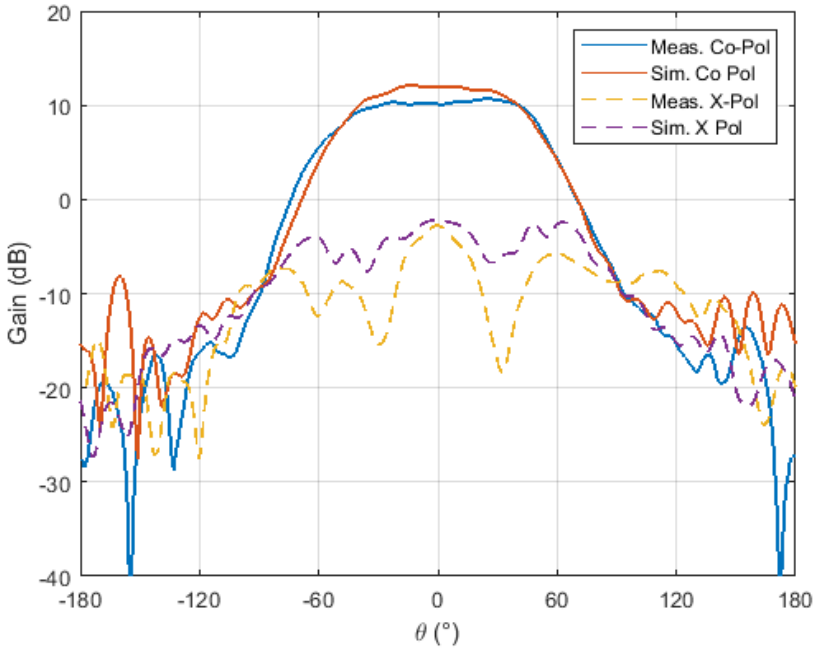

Figure 4.41. Simulation and measurement results of radiation pattern of port 14 at ϕ=0° (3.5 GHz)

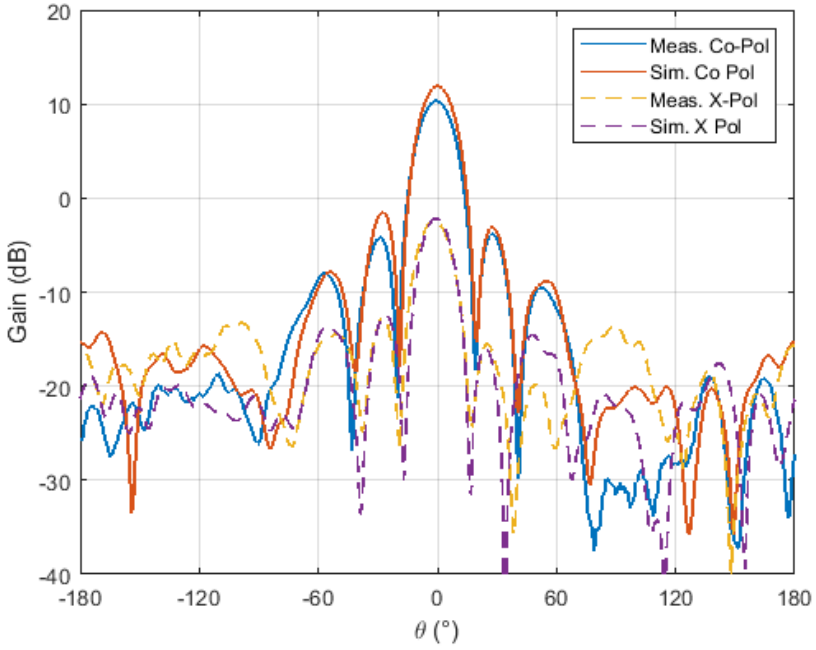

Figure 4.42. Simulation and measurement results of radiation pattern of port 14 at ϕ=90° (3.5 GHz)

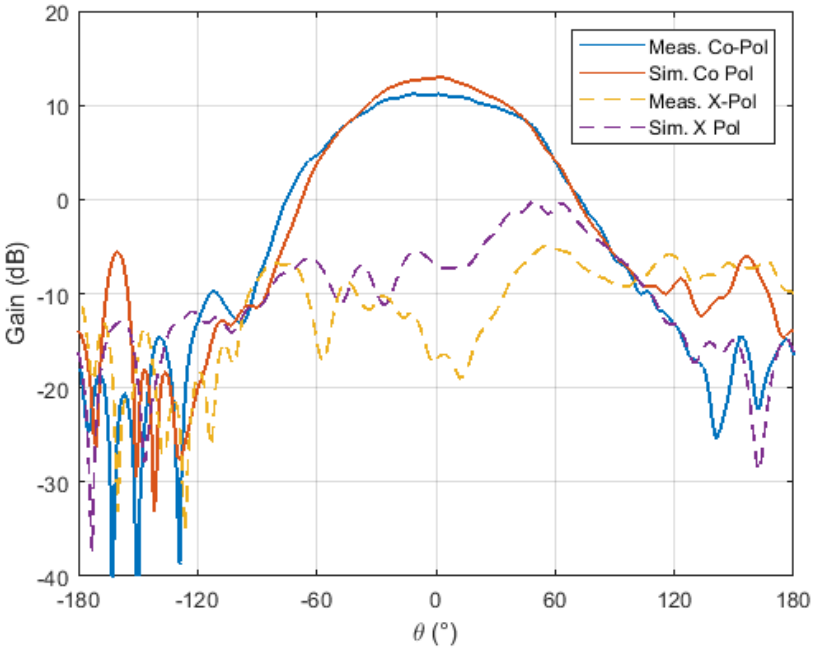

Figure 4.43. Simulation and measurement results of radiation pattern of port 16 at ϕ=0° (3.5 GHz)

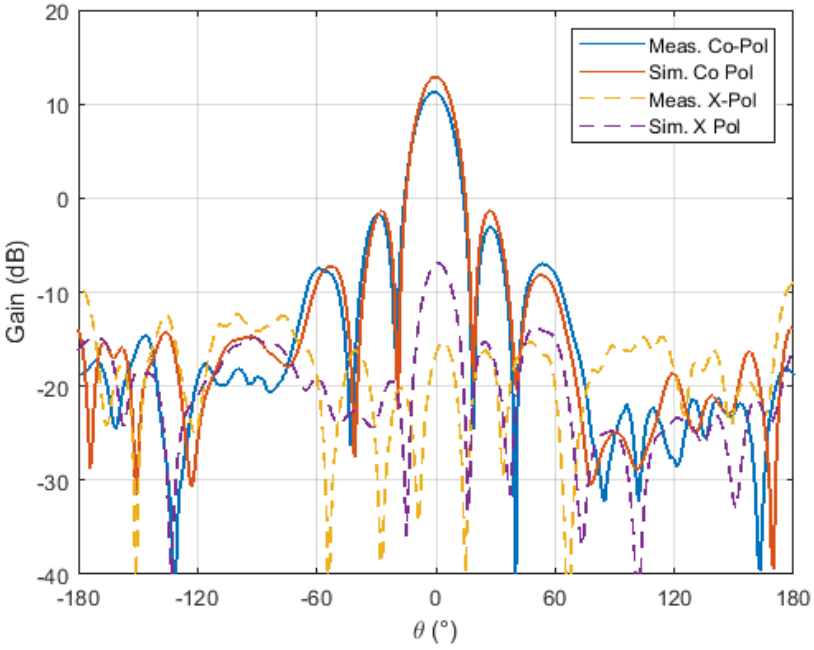

Figure 4.44. Simulation and measurement results of radiation pattern of port 16 at ϕ=90° (3.5 GHz)

Figures 4.45 to 4.50 display co-polarized radiation pattern measurements from port 9 to port 16 at ϕ=0° for various frequencies. Correspondingly, Figures 4.51 to 4.56 present co-polarized radiation pattern measurements from port 9 to port 16 at ϕ=90° for different frequencies. Within these co-polarized radiation patterns, a noticeable trend emerges: the broadside antenna gain escalates as the frequency increases. This phenomenon is in line with the explanation provided in Chapter 3, attributing this effect to the growing electrical dimensions of the patch and the array with increasing frequency.

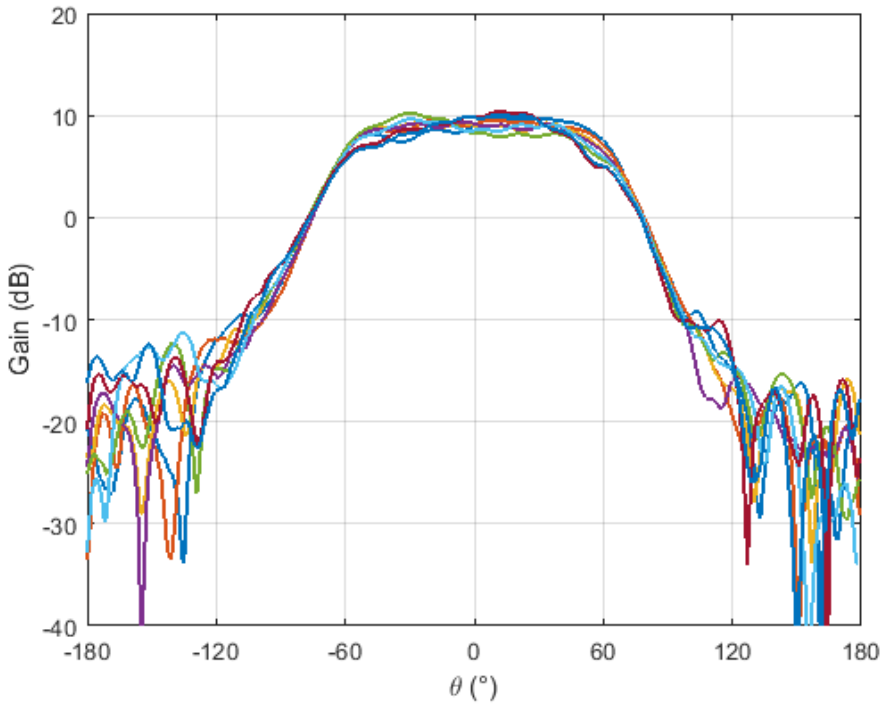

Figure 4.45. Co-Pol radiation pattern for port 9 through port 16 at ϕ=0° (3.3 GHz)

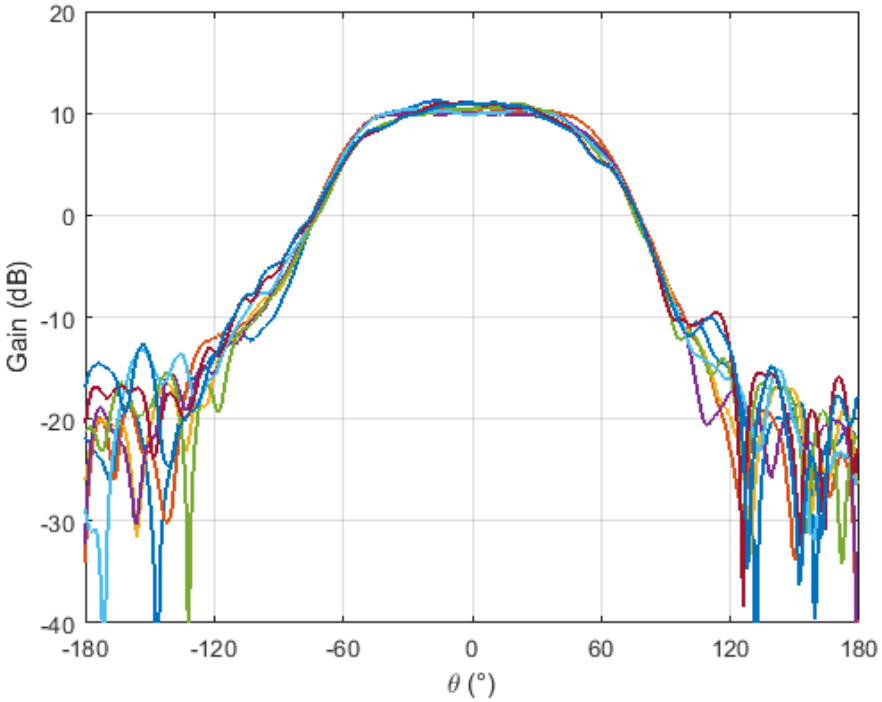

Figure 4.46. Co-Pol radiation pattern for port 9 through port 16 at ϕ=0° (3.4 GHz)

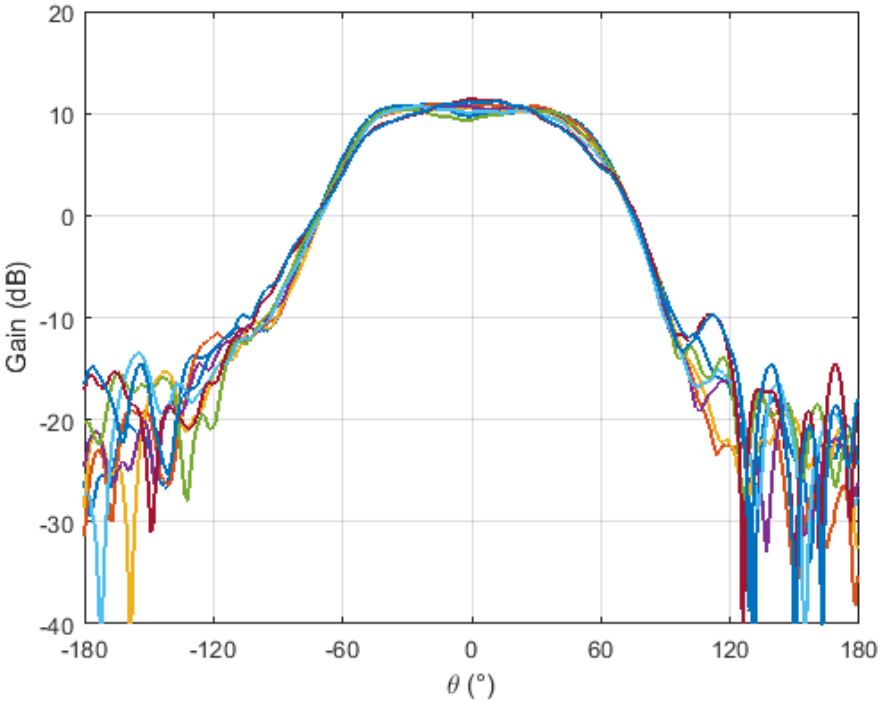

Figure 4.47. Co-Pol radiation pattern for port 9 through port 16 at ϕ=0° (3.5 GHz)

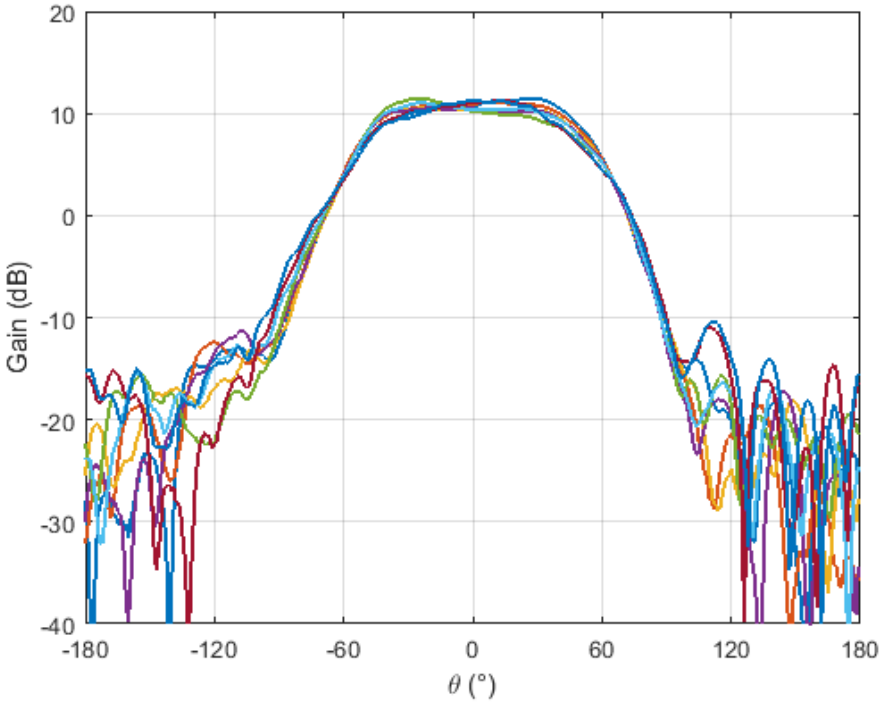

Figure 4.48. Co-Pol radiation pattern for port 9 through port 16 at ϕ=0° (3.6 GHz)

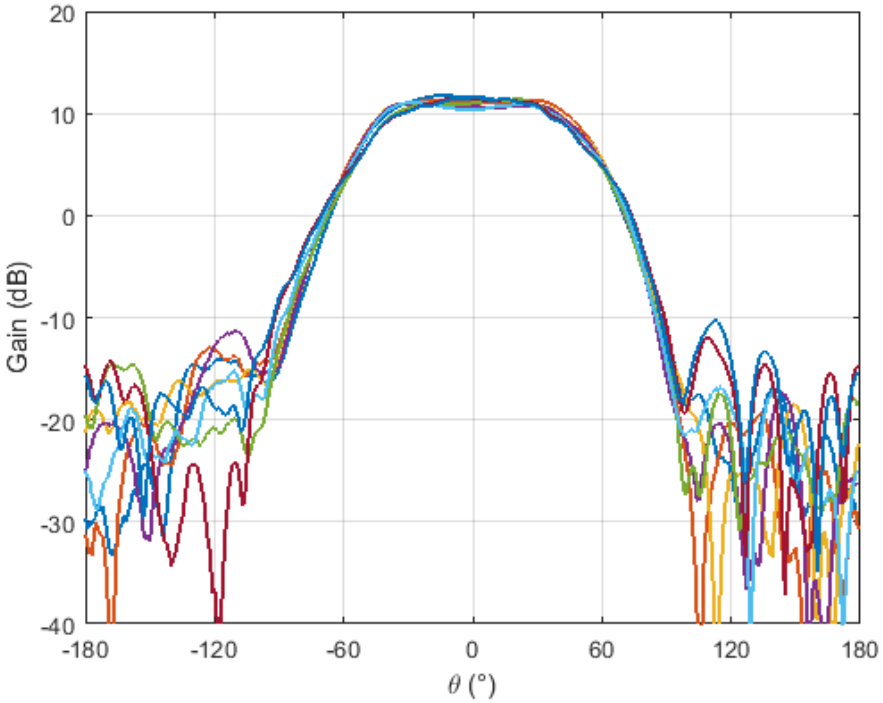

Figure 4.49. Co-Pol radiation pattern for port 9 through port 16 at ϕ=0° (3.7 GHz)

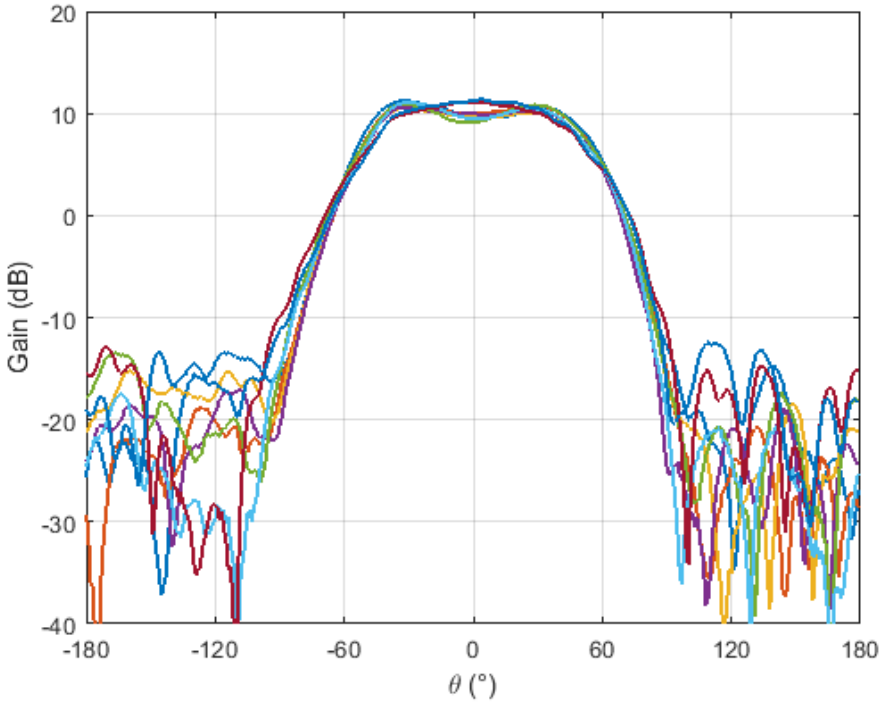

Figure 4.50. Co-Pol radiation pattern for port 9 through port 16 at ϕ=0° (3.8 GHz)

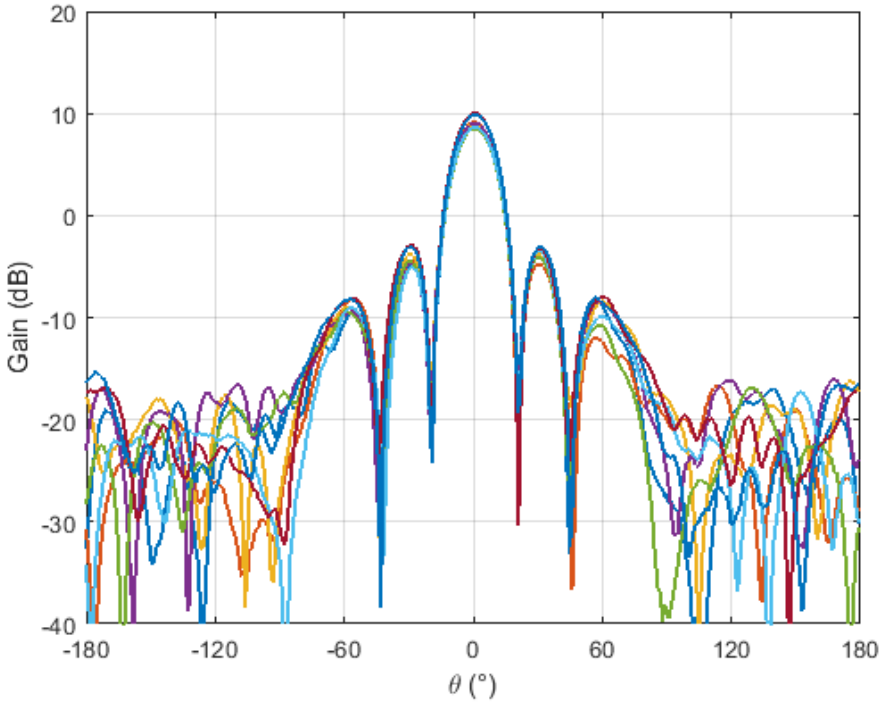

Figure 4.51. Co-Pol radiation pattern for port 9 through port 16 at ϕ=90° (3.3 GHz)

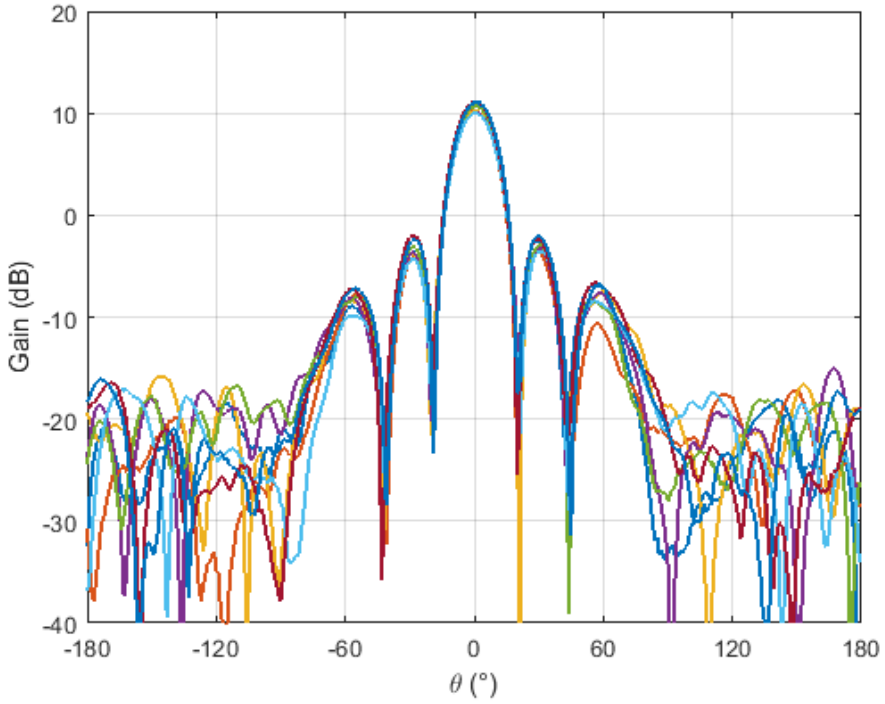

Figure 4.52. Co-Pol radiation pattern for port 9 through port 16 at ϕ=90° (3.4 GHz)

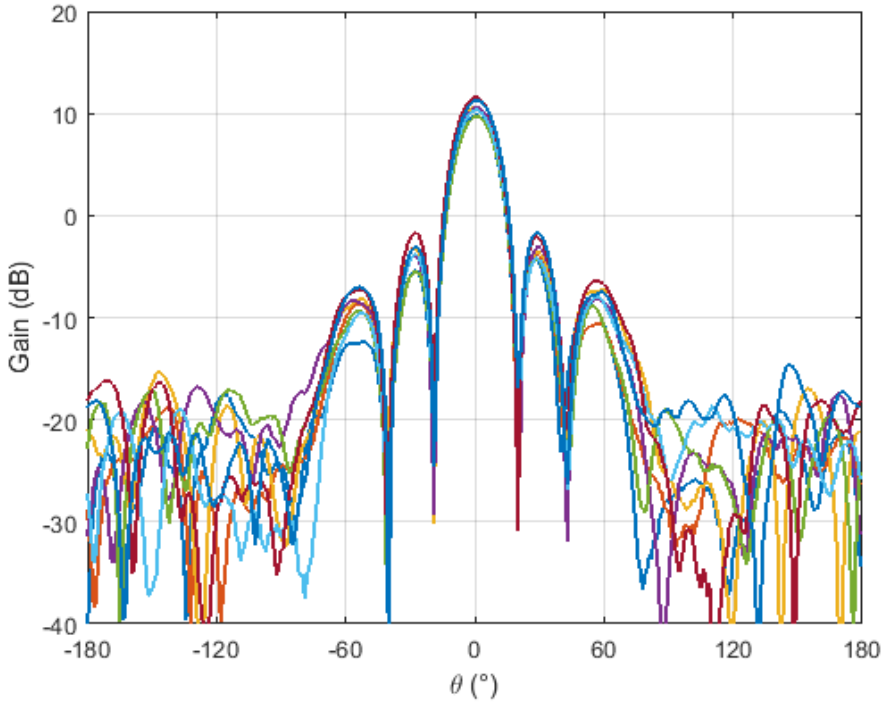

Figure 4.53. Co-Pol radiation pattern for port 9 through port 16 at ϕ=90° (3.5 GHz)

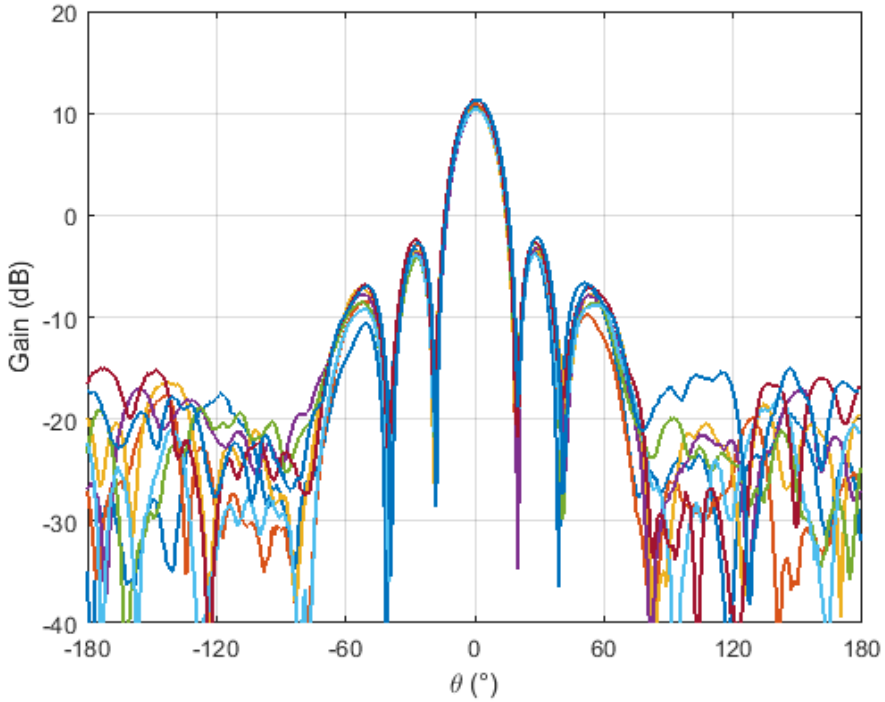

Figure 4.54. Co-Pol radiation pattern for port 9 through port 16 at ϕ=90° (3.6 GHz)

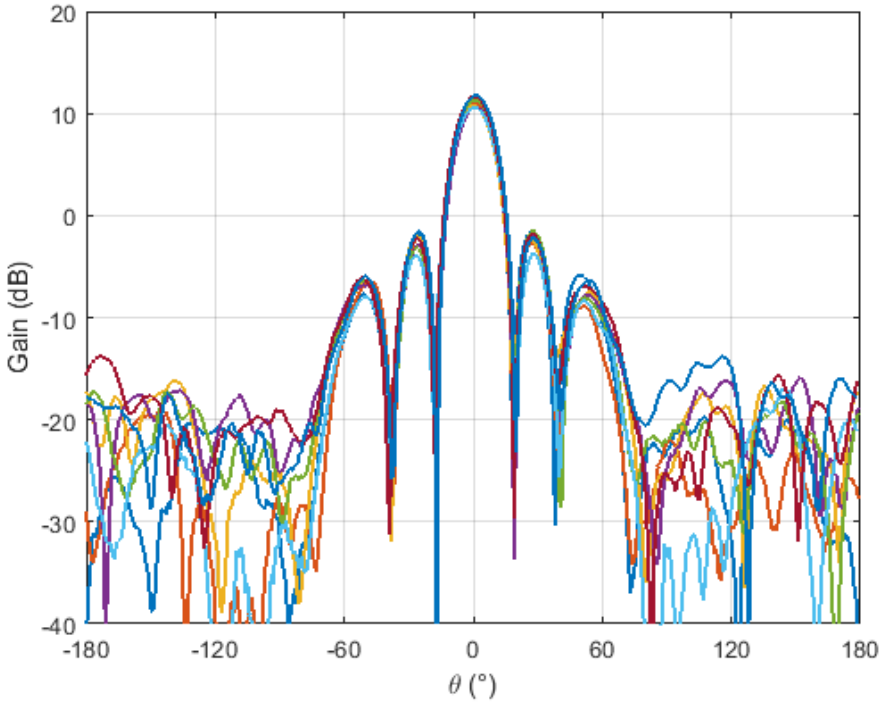

Figure 4.55. Co-Pol radiation pattern for port 9 through port 16 at ϕ=90° (3.7 GHz)

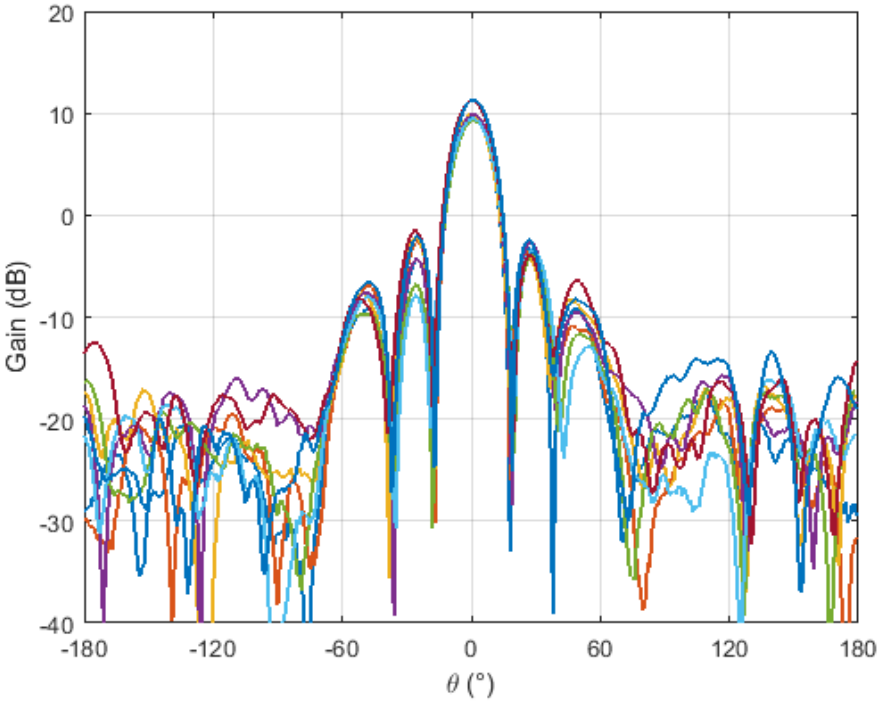

Figure 4.56. Co-Pol radiation pattern for port 9 through port 16 at ϕ=90° (3.8 GHz)

To sum up, in this chapter the configuration of the antenna array is presented, including the number of unit antenna elements and their respective spacings. Subsequently, vertically aligned elements are grouped into sub-arrays and a feeding network is designed for these sub-arrays. Once the feeding network is integrated into the antenna array, a physical prototype of the antenna array is manufactured based on satisfying simulation results. S parameter measurements and radiation pattern measurements in the anechoic chamber are conducted for the prototype and thoroughly analyzed. Since radiation pattern measurements of each subarray are obtained in terms of magnitude and phase, these results can be combined with specific weights in order to perform beamforming. This concept is discussed in the next chapter.

CHAPTER 5

ARRAY PATTERN SYNTHESIS USING ACTIVE ELEMENT PATTERN METHOD

In Chapter 3, unit antenna element is designed, simulated, prototyped and validated by measurements, achieving a thorough understanding of its characteristics. Similarly, Chapter 4, outlined the decisions for the antenna array configuration, delving into element numbers and spacings. The simulation journey then led to the evaluation of a 4×8 antenna array, where each unit element was individually excited. Subsequently, the design and implementation of the feeding network emerged, connecting the -45° or 45° polarized ports of each 1×4 vertical sub-array. The simulations involving the integrated antenna array and feeding network justified the initiation of an actual prototype. Comprehensive measurements were performed, encompassing S parameters and radiation patterns. However, the complexity of engaging all 16 ports presented challenges such as exciting all of the ports at the same time, moreover applying specific weights (amplitude and phase) to each input port. Consequently, the active element pattern (AEP) method was employed to obtain overall array radiation pattern, allowing the measurement of one port at a time while the others were terminated with 50 Ω load. A distinctive advantage of AEP lies in its incorporation of mutual coupling effects between sub-arrays, given that the measured sub-array is integrated into the whole array while others remain terminated with matched load.

5.1 Formulation

The active element pattern denotes the radiation pattern of the array in the scenario where a single radiating element is excited while all others are terminated with matched loads. Utilizing the superposition principle, the far-field radiation pattern

produced by an array where all elements are driven can be mathematically represented using active element patterns, as showcased in [36]:

$$E_t(\theta,\phi) = \sum_{n=1}^{N} I_n E_n(\theta,\phi) \tag{5.1}$$

where E_t is the total radiation pattern of the antenna array, I_n is the complex excitation coefficient of n^{th} element, and E_n is the active element pattern of the n^{th} element.

5.2 Beamforming with AEP Method

Utilizing the principle outlined in Equation (5.1), AEP method is employed to generate different beams by using measured active element patterns, which are then compared with simulation results. To reveal the correlation between simulation and measurement outcomes, additional losses between simulation and measurement results of subarray patterns discussed in Chapter 4 are compensated. This is done by means of subtracting 1.5 dB from simulated radiation patterns. As a result, peak gains (broadside gains) of the radiation patterns obtained by simulation and AEP method are equated in the following figures. Moreover, a MATLAB script implementing the AEP method throughout this chapter can be found in Appendix A.

Figures 5.1 to 5.4 depict the co-polarized radiation patterns at ϕ=0° plane, operating at 3.5GHz, while various ports (sub-arrays) are excited with equal amplitudes and phases in order to demonstrate the accuracy of the method. Different beams are obtained, each exhibiting peak gains of 13.67 dB, 15.42 dB, 16.67 dB and 19.73 dB, respectively. The corresponding HPBWs are 50°, 32°, 23° and 11°. A noteworthy consistency is observed between the radiation patterns generated by full-wave simulations and the AEP method However, it is important to highlight that, beyond the θ=60° cone, simulation results exhibit slight degradation from measurement results. This degradation becomes more pronounced as θ exceeds 90° and reaches 180°. This occurrence can be attributed to the size of the radiation box in the

simulation setup. The +z direction offset of the radiation box is intentionally kept sufficiently large, while offsets in the +x, -x, +y, -y, and -z directions are relatively smaller. This setup design aims to balance computational resource utilization and simulation time.

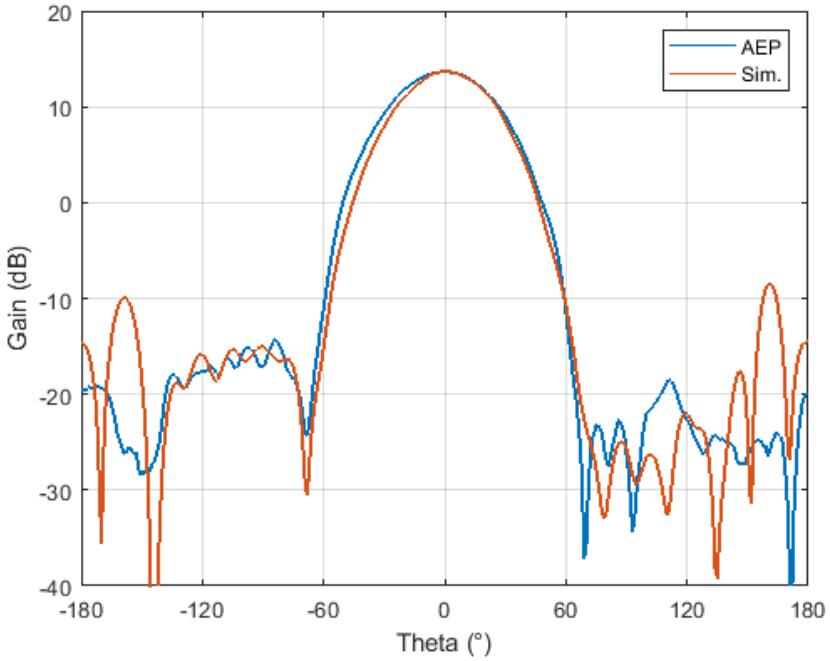

Figure 5.1. Co-Pol radiation pattern at ϕ=0° plane when port 14 and port 16 are excited (3.5 GHz)

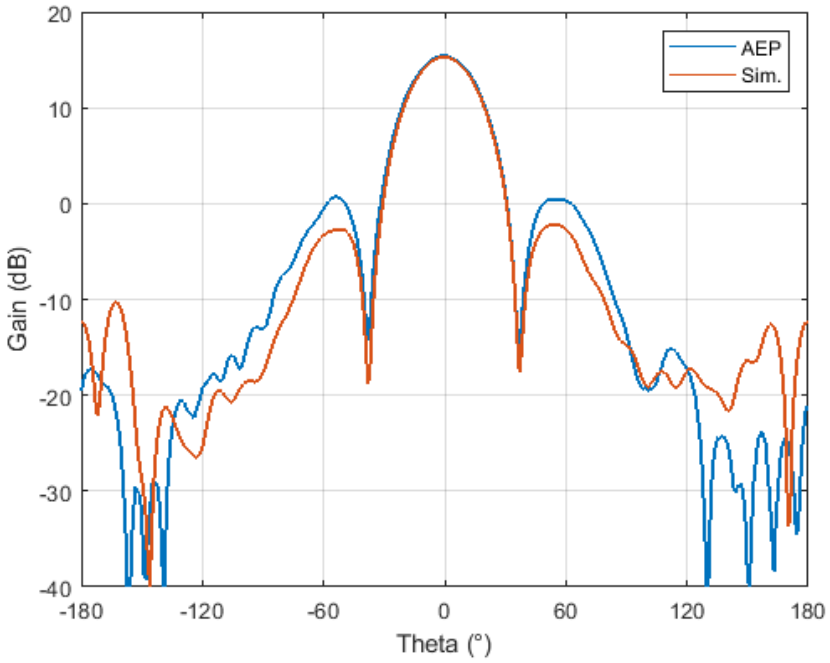

Figure 5.2. Co-Pol radiation pattern at ϕ=0° plane when port 12, port 14 and port 16 are excited (3.5 GHz)

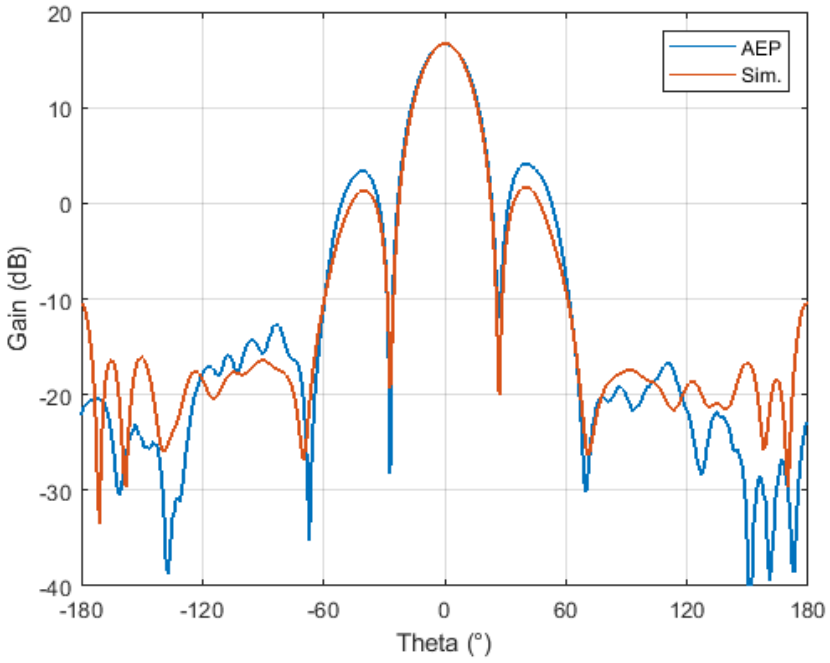

Figure 5.3. Co-Pol radiation pattern at ϕ=0° plane when port10, port 12, port 14 and port 16 are excited (3.5 GHz)

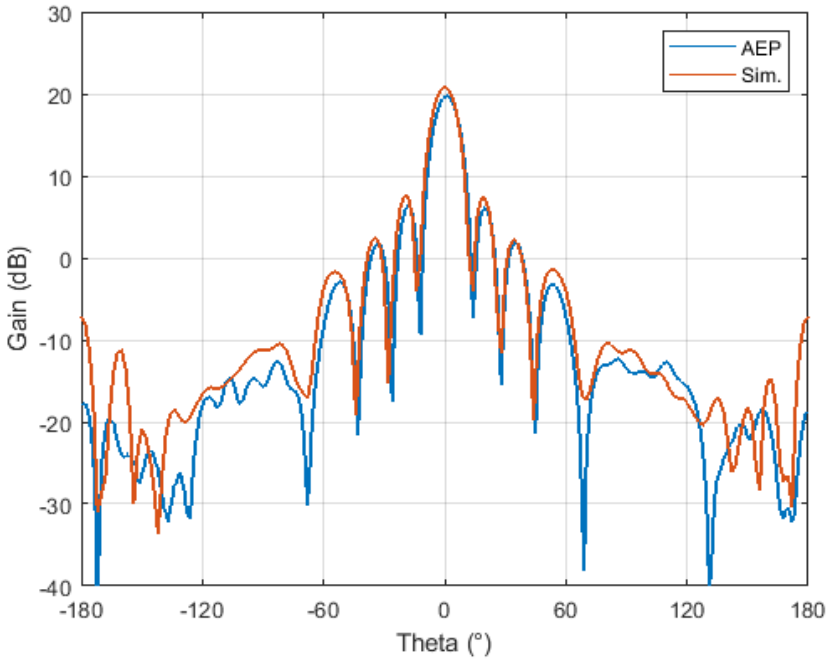

Figure 5.4. Co-Pol radiation pattern at ϕ=0° plane when all 8 sub-arrays are excited from +45° polarized ports (3.5 GHz)

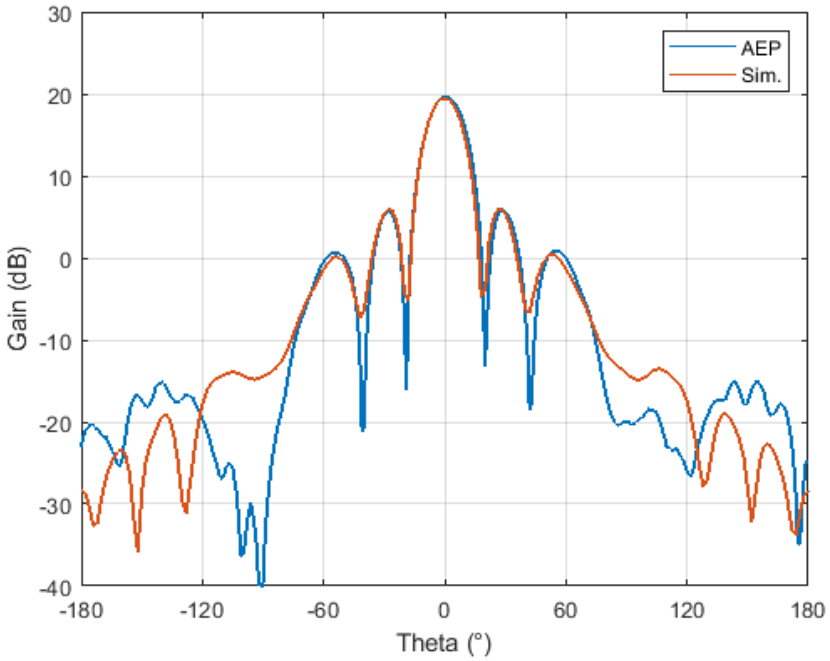

Figure 5.5. Co-Pol radiation pattern at ϕ=90° plane when all 8 sub-arrays are excited from +45° polarized ports (3.5 GHz)

Similarly, Figures 5.5 depicts the co-polarized radiation pattern at the ϕ=90° plane, operating at 3.5 GHz, while all of the 8 ports (sub-arrays) are excited with equal amplitudes and phases. The generated beam exhibits the peak gain of 19.73 dB as before, and Half-Power Beamwidth (HPBW) of 17°. Since there is no change in the number of elements in y direction regardless of number of excited ports, HPBW is always constant at ϕ=90° plane and do not depend on number of excited ports.

5.3 Beamsteering with AEP Method

Since, equivalently we have linear array of 8 sub-arrays, and each sub-array is driven independently, progressive phase shift may be applied to each port which leads resulting beam to be steered. This is equivalent to adjusting the phase of the I_n term in Equation (5.1). Figure 5.6 to 5.11 represents the radiation patterns at the ϕ=0° plane, operating at 3.5 GHz while all of the 8 sub-arrays are excited with various progressive phase shifts.

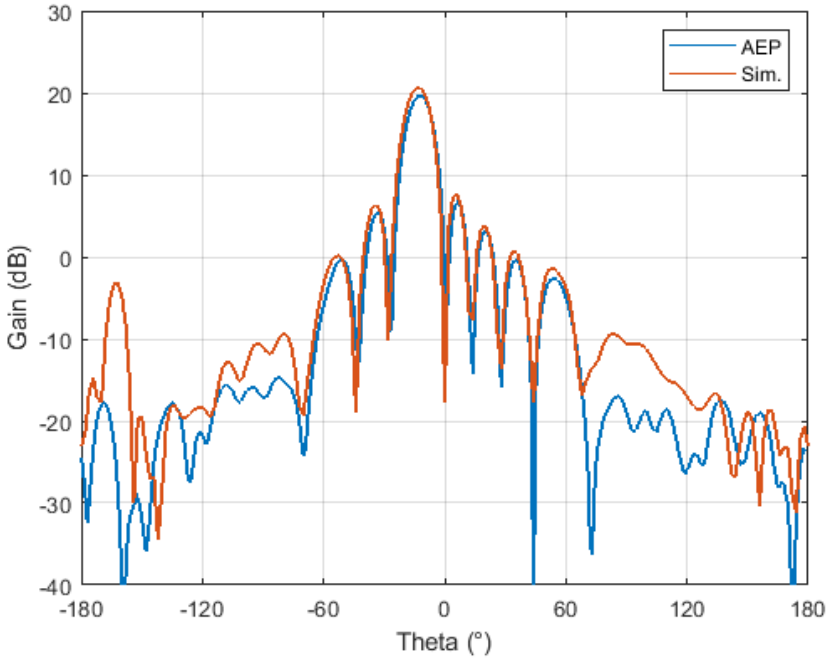

Figure 5.6. Co-Pol radiation pattern at ϕ=0° plane beam steered to θ=-13° with 45° progressive phase shift between elements (3.5 GHz)

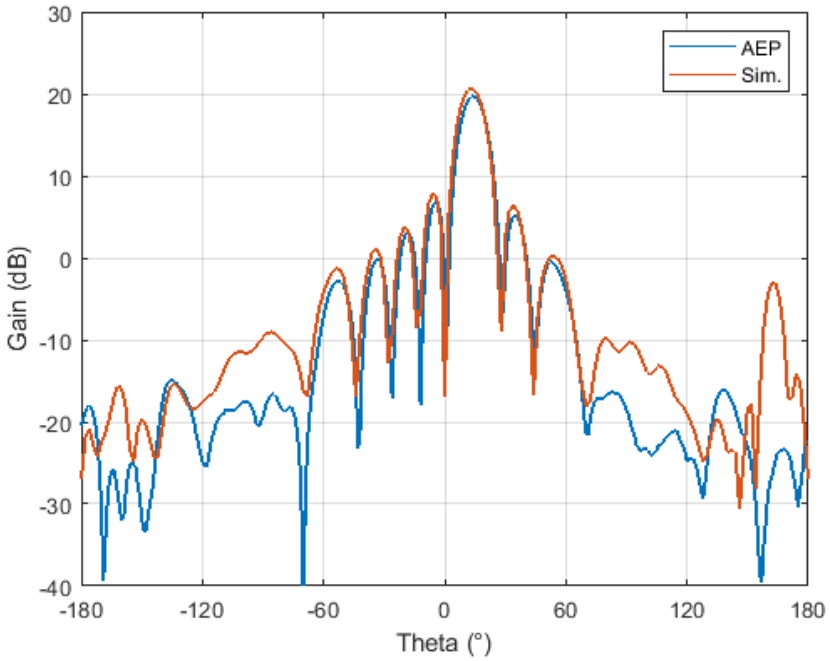

Figure 5.7. Co-Pol radiation pattern at ϕ=0° plane beam steered to θ=13° with -45° progressive phase shift between elements (3.5 GHz)

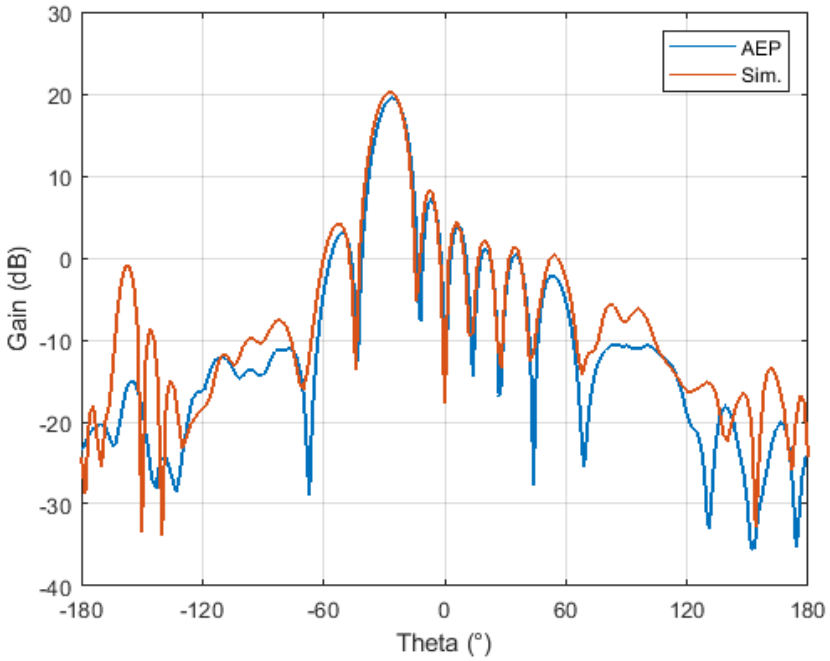

Figure 5.8. Co-Pol radiation pattern at ϕ=0° plane beam steered to θ=-27° with 90° progressive phase shift between elements (3.5 GHz)

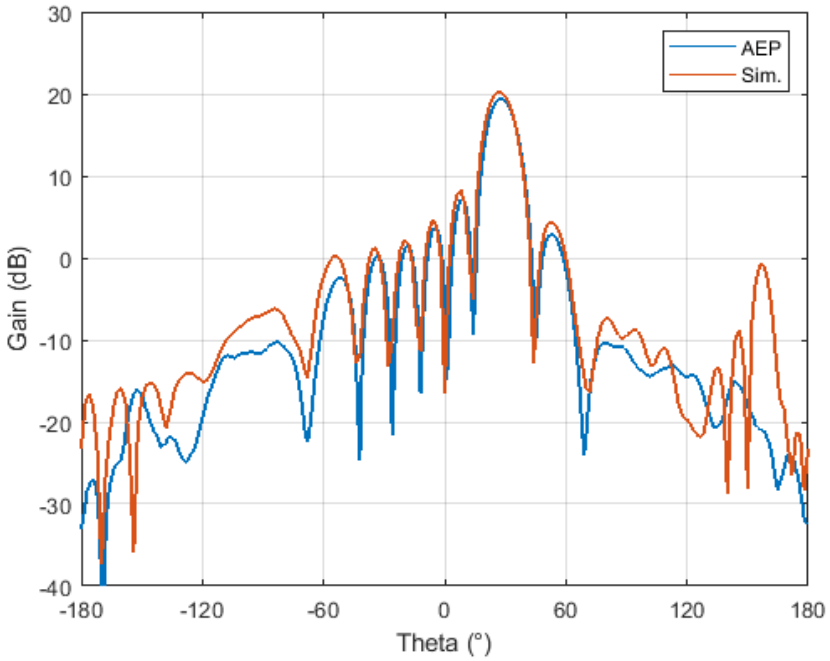

Figure 5.9. Co-Pol radiation pattern at ϕ=0° plane beam steered to θ=27° with -90° progressive phase shift between elements (3.5 GHz)

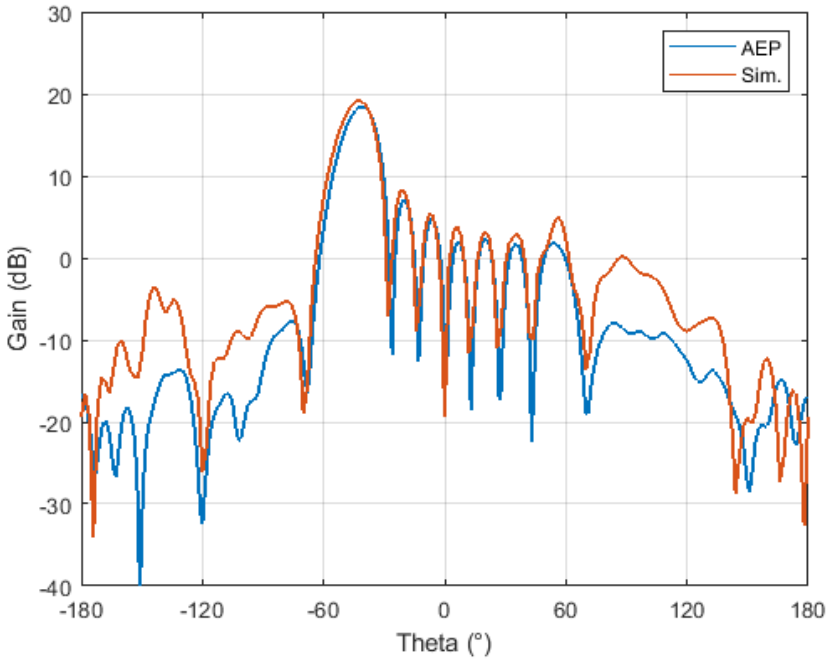

Figure 5.10. Co-Pol radiation pattern at ϕ=0° plane beam steered to θ=-42° with 135° progressive phase shift between elements (3.5 GHz)

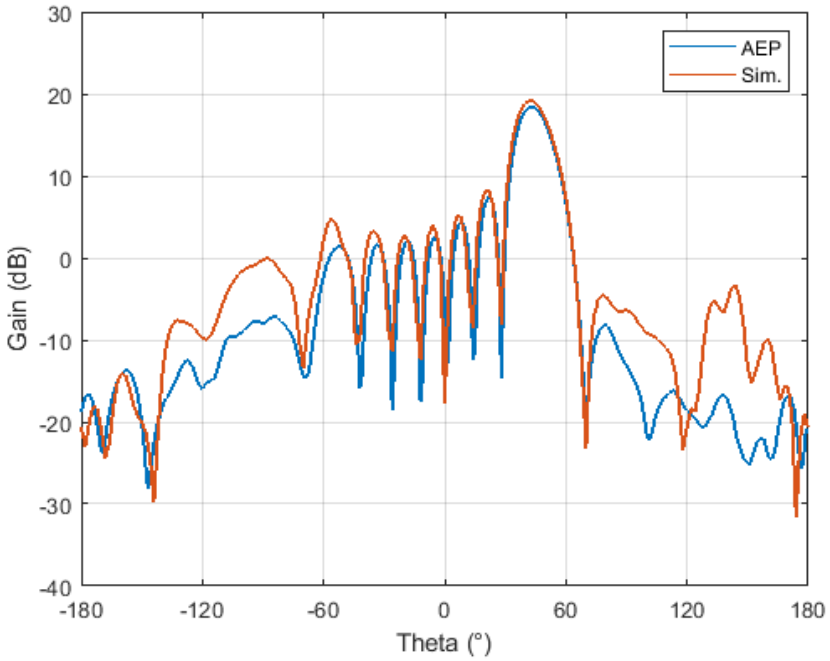

Figure 5.11. Co-Pol radiation pattern at ϕ=0° plane beam steered to θ=42° with -135° progressive phase shift between elements (3.5 GHz)

5.4 Multi-Beam Forming

Up to this point, the generation of different beams by combining various numbers of sub-arrays (as discussed in Chapter 5.2) and the ability to steer these beams to various angles (as explained in Chapter 5.3) have been explored. Considering a practical scenario in which a BS or radio is surrounded by multiple UE devices, such as mobile phones or other cellular devices, located in different directions, the concept of multi-beamforming becomes highly relevant. Through multi-beamforming, it becomes feasible to simultaneously assign distinct beams to these devices. These beams can be generated at varying polarizations and frequencies, allowing for steering in different directions. This approach leverages polarization diversity, spatial diversity, and frequency diversity to optimize overall communication performance.

Utilizing the active element method in conjunction with measurement results of the sub-arrays, the generation of four distinct beams is demonstrated to showcase the capability of multi-beamforming. The resultant beams are depicted in Figure 5.12. Beam 1, operating at 3.5 GHz, is generated by employing ports 2, 4, 6, and 8 (located on the right half of the array). Consequently, it exhibits a +45° polarization and is directed towards +14°. Proceeding to Beam 2, which operates at 3.8 GHz, its generation involves ports 10, 12, 14, and 16 (located on the left half of the array), yielding a +45° polarization and steering angle of -14°. Moving to Beam 3, also operating at 3.8 GHz, it is formed by utilizing ports 1, 3, 5, and 7 (located on the right half of the array). This results in a -45° polarization and a steering angle of -28°. Lastly, Beam 4, generated at 3.5 GHz, is produced through ports 9, 11, 13, and 15 (on the left half of the array). It exhibits a -45° polarization and is steered towards +28°. It is noteworthy that Beam 2 and Beam 4 share the same sub-array elements but employ different polarized ports, as do Beam 1 and Beam 3. To enhance isolation, Beam 2 and Beam 4 operate at different frequencies, similar to the operation of Beam 1 and Beam 3, which also function at different frequencies. This frequency separation mitigates potential cross-talk or interference, thereby optimizing the effectiveness of the multi-beamforming approach.

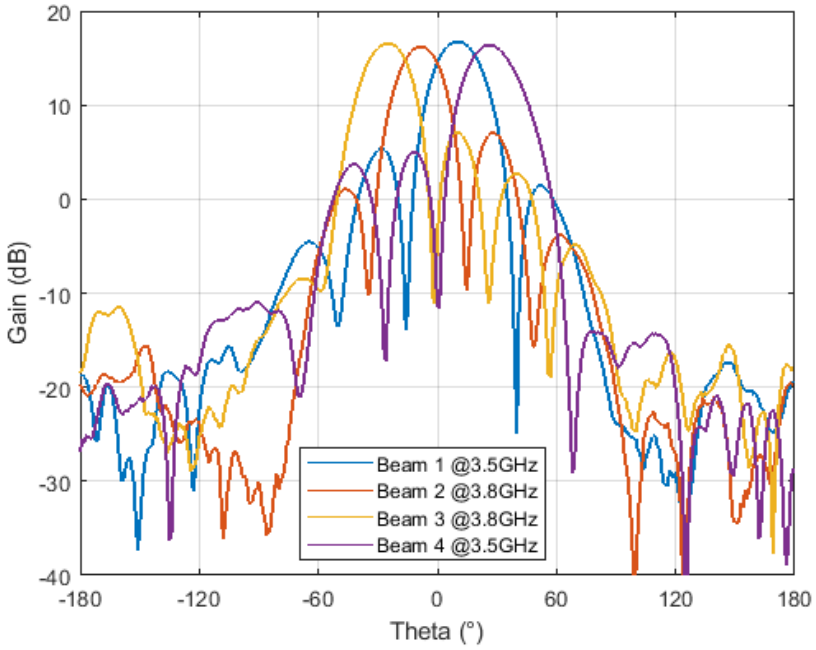

Figure 5.12. Multi-beam forming at different frequencies and polarizations

To sum up, in this chapter, radiation pattern measurement results of each sub-array where a single radiating element is excited while all others are terminated with matched load are superposed. In other words, far-field patterns of the sub-arrays are linearly combined by adjusting their phases or by deactivating some sub-arrays. In this way, several beams are obtained, beams are steered or more than one beam is generated at the same time to demonstrate multibeam forming.

CHAPTER 6

CONCLUSION

6.1 Summary and Conclusions

Throughout this thesis study, MIMO antenna array design for 5G applications is discussed. The primary motivation is to enhance the performance of the communication system by incorporating several concepts.

First of all, a broad frequency band is essential in fifth-generation communication systems in order to enhance the data rate and channel capacity therefore antenna bandwidth is an important attribute to support this idea. The MIMO antenna array covered and designed in the scope of this thesis operates at sub-6GHz region of the 5G protocol specifically at n78 band.

Furthermore, in 5G MIMO systems, polarization diversity plays a role during signal transmission and reception. A crucial benefit of this diversity is its ability to counteract the effects of multipath fading. Moreover, polarization diversity contributes to expanding the data-carrying capacity of the communication channel. Through the incorporation of various polarizations, the system becomes capable of concurrently transmitting multiple distinct data streams. This advancement leads to a substantial increase in both data rate and overall capacity of the system. This concept is implemented in the proposed antenna element by aligning the location of the feeding point of the stacked microstrip patch antenna.

Other employed concepts as important attributes of the proposed MIMO antenna array are the ability of beamsteering, multi-beam forming and spatial multiplexing of the antenna array. These are ensured by the 8×4 configuration and feeding techniques incorporated in the design and lead to a substantial augmentation of data rates and network capacity.

As presented in Chapter 3, simulation enviroment and simulaton setup is build in order to implement chosen unit antenna element which was coaxially dual fed stacked patch antenna with air gap in between its layer. Physical aspects, dimensions and stack up configuration of the unit element are determined. In order to optimize the antenna performance, parametric sweeps are performed in the simulations. Following finalization of the simulation phase by satisfying results, a prototype was manufactured based on designed unit antenna element and comprehensively measured in order to compare simulation and measurement results. As a result, a unit element antenna was obtained with an impedance bandwidth of more than 500 MHz considering 10 dB return loss level. The unit antenna demonstrates over 20 dB of isolation between its ports in the region of interest. Resulting surface current distributions on the patches were alligned with diagonal axes of the square shaped patches which enables the slant polarized excitation. As for radiation pattern, 10 dB of broadside gain was obtained with more than 60° of HPBW and 17 dB front to back ratio at 3.5 GHz.

Upon agreement between simulation and measurement results of the unit element, array design phase was initiated as presented in Chapter 4. Antenna array configurations were explored, element number and element spacings were determined. Following the implementation of proposed array configuration, resulting antenna array radiation pattern and its beamforming/beamsteering capabilities were investigated in the simulation environment. On the other hand, a feeding network for antenna elements was designed in order to propose a practical way to feed total of 32 elements. After refinement of the antenna array design, a prototype array was manufactured based on proposed design. Subsequently, the fabricated prototype underwent comprehensive measurements, and a detailed analysis of its performance was conducted. As a result, return loss performance similar to that of the unit element was obtained for the antenna array. Minimum 20 dB of isolation was measured between adjacent subarrays. Measured radiation patterns are utilized in order to apply active element pattern (AEP) method to generate different beams in Chapter 5. When all of the 32 elements are excited,

generated beam has 19.73 dB peak gain with 11° and 17° HPBWs in ϕ=0° and ϕ=90° planes, respectively. Front to back ratio was approximately 38 dB. Generated beam was also steered in ϕ=0° and ϕ=90° planes where grating lobes occured when beam steered to θ=60° and θ=15° at the ϕ=0° and ϕ=90° planes, respectively. Also AEP method was utilized in order to perform multibeam forming and generate different beams with different sub-array configurations in order to be used in different scenarios. Resulting beams belong to this concept was presented in Chapter 5.

While above-mentioned concepts are incorporated into the design, following conclusions emerge:

Incorporating stacked patches in the designed antenna, may significantly broaden the impedance bandwidth. Another conclusion about the bandwidth enhancement is that incorporating the air gap in the desing leads to quality factor reduction due to increasing volume of the antenna and also due to decreasing effective dielectric constant of the substrate. As quality factor decreases, the bandwidth is enhanced by inserted air gap. It is also notable that the physical aspects, dimensions and stack up configuration of the unit element should be optimized in order to achieve these bandwidth enhancements.

Furthermore, as a final remark, modular structure of the designed antenna array enables different configurations while performing multi-beam forming. This is important when creating different excitation schemes to provide solutions to different scenarios.

6.2 Future Works

Throughout this thesis study, the performance of the proposed antenna is evaluated by S parameters measurements and radiation pattern measurements.Although, these measurement results are sufficiently satisfying, in order to evaluate the performance of the proposed design in a real scenario, the designed antenna array can be integrated into a 5G radio unit. In this case, performance enhancement concepts presented in

Chapter 2 can be evaluated in terms of their corresponding metrics. Upon evaluation of the antenna array based on this integration, it can be optimized iteratively, if necessary.

Another idea to be implemented as next step of this thesis study is array pattern synthesis using non-uniform excitation. In Chapter 5 of this thesis study, AEP method is applied by exciting each sub-array using equal amplitudes. However, by using different methods from literature (e.g. Taylor Line-Source Method) non-uniform excitation coefficients can be obtained so that side lobe level, half-power beam width and null locations can be controlled.

Finally, another future study can be scaling up the antenna array since designed antenna array has modular structure. In this way, the proposed design can be scaled into a massive MIMO antenna array. For example, by locating two identical 8×4 arrays side by side, as shown in Figure 6.1, antenna gain can be improved and also by applying progressive phase shift between two arrays beam can be steered on y direction.

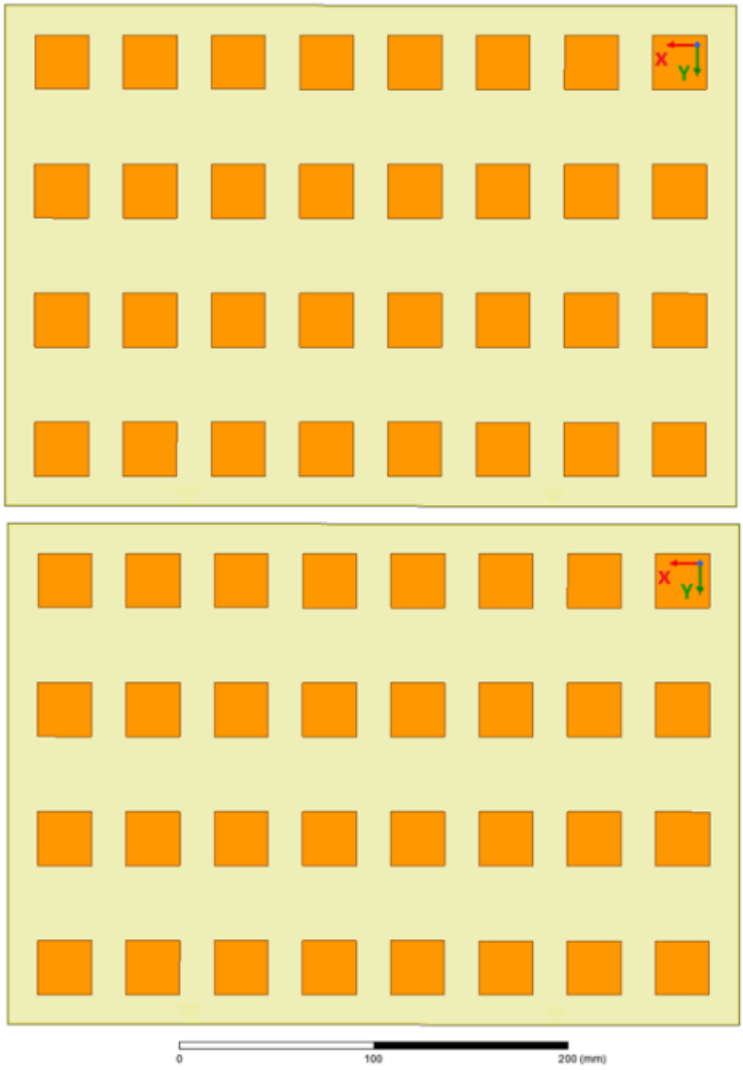

Figure 6.1. Two identical 8×4 arrays located side by side

REFERENCES

[1] WHY DO WE NEED 5G?. ETSI. (n.d.). https://www.etsi.org/technologies/5g

[2] Rodriguez Avila, D. (2021). A portable picocell antenna for 5G (thesis). Retrieved from https://infoscience.epfl.ch/record/286797?ln=fr.

[3] Puskely, J., Mikulasek, T., Aslan, Y., Roederer, A., & Yarovoy, A. (2022). 5G SIW-based phased antenna array with cosecant-squared shaped pattern. IEEE Transactions on Antennas and Propagation, 70(1), 250–259. https://doi.org/10.1109/tap.2021.3098577

[4] Mishra, G., & Sharma, S. K. (2021). A multifunctional full-polarization reconfigurable 28 GHz staggered butterfly 1-D-beam steering antenna. IEEE Transactions on Antennas and Propagation, 69(10), 6468–6479. https://doi.org/10.1109/tap.2021.3070226

[5] Hamberger, G. F., Trummer, S., Siart, U., & Eibert, T. F. (2017). A planar dual-polarized microstrip 1-D-beamforming antenna array for the 24-GHz band. IEEE Transactions on Antennas and Propagation, 65(1), 142–149. https://doi.org/10.1109/tap.2016.2618847

[6] Ding, C., Sun, H.-H., Zhu, H., & Jay Guo, Y. (2020). Achieving wider bandwidth with full-wavelength dipoles for 5G base stations. IEEE Transactions on Antennas and Propagation, 68(2), 1119–1127. https://doi.org/10.1109/tap.2019.2950108

[7] Ntawangaheza, J. de, Sun, L., Xie, Z., Pang, Y., Zheng, Z., & Rushingabigwi, G. (2021). A single-layer low-profile broadband metasurface antenna array for sub-6 ghz 5G Communication Systems. IEEE Transactions on Antennas and Propagation, 69(4), 2061–2071. https://doi.org/10.1109/tap.2020.3027042

[8] Liu, Y., Li, Y., Ge, L., Wang, J., & Ai, B. (2020). A compact hepta-band mode-composite antenna for SUB (6, 28, and 38) ghz applications. IEEE Transactions on Antennas and Propagation, 68(4), 2593–2602. https://doi.org/10.1109/tap.2019.2955206

[9] Lan, J., Yu, Z., Zhou, J., & Hong, W. (2020). An aperture-sharing array for (3.5, 28) ghz terminals with steerable beam in millimeter-wave band. IEEE Transactions on Antennas and Propagation, 68(5), 4114–4119. https://doi.org/10.1109/tap.2019.2948706

[10] Chu, Q.-X., & Luo, Y. (2013). A broadband unidirectional multi-dipole antenna with very stable beamwidth. IEEE Transactions on Antennas and Propagation, 61(5), 2847–2852. https://doi.org/10.1109/tap.2013.2243898

[11] Zheng, D.-Z., & Chu, Q.-X. (2017). A multimode wideband ± 45° dual-polarized antenna with embedded loops. IEEE Antennas and Wireless Propagation Letters, 16, 633–636. https://doi.org/10.1109/lawp.2016.2594240

[12] Huang, H., Liu, Y., & Gong, S. (2017). A broadband dual-polarized base station antenna with Anti-Interference Capability. IEEE Antennas and Wireless Propagation Letters, 16, 613–616. https://doi.org/10.1109/lawp.2016.2594095

[13] Mak, K. M., Lai, H. W., & Luk, K. M. (2018). A 5G wideband patch antenna with antisymmetric L-shaped probe feeds. IEEE Transactions on Antennas and Propagation, 66(2), 957–961. https://doi.org/10.1109/tap.2017.2776973

[14] Chu, Q.-X., Wen, D.-L., & Luo, Y. (2015). A broadband ±45° dual-polarized antenna with Y-shaped feeding lines. IEEE Transactions on Antennas and Propagation, 63(2), 483–490. https://doi.org/10.1109/tap.2014.2381238

[15] Wen, D.-L., Zheng, D.-Z., & Chu, Q.-X. (2017). A wideband differentially fed dual-polarized antenna with stable radiation pattern for base stations. IEEE Transactions on Antennas and Propagation, 65(5), 2248–2255. https://doi.org/10.1109/tap.2017.2679762

[16] Ye, L. H., Zhang, X. Y., Gao, Y., & Xue, Q. (2020). Wideband dual-polarized four-folded-dipole antenna array with stable radiation pattern for base-station applications. IEEE Transactions on Antennas and Propagation, 68(6), 4428–4436. https://doi.org/10.1109/tap.2020.2969749

[17] Ding, C. F., Zhang, X. Y., & Yu, M. (2020). Simple dual-polarized filtering antenna with enhanced bandwidth for base station applications. IEEE Transactions on Antennas and Propagation, 68(6), 4354–4361. https://doi.org/10.1109/tap.2020.2975282

[18] Gao, Y., Ma, R., Wang, Y., Zhang, Q., & Parini, C. (2016). Stacked patch antenna with dual-polarization and low mutual coupling for massive MIMO. IEEE Transactions on Antennas and Propagation, 64(10), 4544–4549. https://doi.org/10.1109/tap.2016.2593869

[19] Li, T., Li, Q., Zhang, M., Zhang, A. X., Zhang, J., & Chen, X. (2019). Four-beam antenna array with low side-lobe for base station application. 2019 Photonics & Electromagnetics Research Symposium - Fall (PIERS - Fall). https://doi.org/10.1109/piers-fall48861.2019.9021549

[20] Ansari, M., Jones, B., Zhu, H., Shariati, N., & Guo, Y. J. (2021). A highly efficient spherical Luneburg lens for low microwave frequencies realized with a metal-based artificial medium. IEEE Transactions on Antennas and Propagation, 69(7), 3758–3770. https://doi.org/10.1109/tap.2020.3044638

[21] Gu, L., Yang, W., Che, W., Chen, D., Zhang, Y., & Feng, W. (2018). A dual-steerable-beam multi-slot coupled metasurface antenna. 2018 IEEE International Conference on Computational Electromagnetics (ICCEM). https://doi.org/10.1109/compem.2018.8496675

[22] Sanad, M., & Hassan, N. (2019). A sub-6 GHz multi-beam base station antenna for 5G with an arbitrary beam-tilting for each beam. 2019 IEEE Radio and Wireless Symposium (RWS). https://doi.org/10.1109/rws.2019.8714542

[23] Kayani, H. A., Gueuning, Q., Goreux, N., Vanhoenacker-Janvier, D., Oestges, C., & Craeye, C. (2020). Reconfigurable cellular base station antenna consisting of parasitic radiators. IEEE Transactions on Industrial Electronics, 67(8), 7083–7093. https://doi.org/10.1109/tie.2019.2935991

[24] Walter Honcharenko, M. (2019, April 16). Sub-6 ghz MMIMO base stations meet 5G's size and weight challenges. Microwave Journal.

https://www.microwavejournal.com/articles/31754-sub-6-ghz-mmimo-base-stations-meet-5gs-size-and-weight-challenges

[25] Kumar, S., Dixit, A. S., Malekar, R. R., Raut, H. D., & Shevada, L. K. (2020). Fifth generation antennas: A comprehensive review of design and performance enhancement techniques. IEEE Access, 8, 163568–163593. https://doi.org/10.1109/access.2020.3020952

[26] Ansari, R. I., Aslam, M. A., & Chrysostomou, S. A. H. and Chrysostomos. (2018, August 22). Network coding for distributed Antenna Systems. IntechOpen. https://www.intechopen.com/chapters/60835

[27] Shah, A. F., & Islam, Md. S. (2014). A survey on cooperative communication in Wireless Networks. International Journal of Intelligent Systems and Applications, 6(7), 66–78. https://doi.org/10.5815/ijisa.2014.07.09

[28] Zhang, H., Dai, H., Zhou, Q., & Hughes, B. L. (2006). On the Diversity Order of spatial multiplexing systems with transmit antenna selection: A geometrical approach. IEEE Transactions on Information Theory, 52(12), 5297–5311. https://doi.org/10.1109/tit.2006.885531

[29] Bjornson, E., Hoydis, J., Kountouris, M., & Debbah, M. (2014). Massive MIMO systems with Non-Ideal Hardware: Energy Efficiency, estimation, and capacity limits. IEEE Transactions on Information Theory, 60(11), 7112–7139. https://doi.org/10.1109/tit.2014.2354403

[30] Gani, A. (2023). Implementation of massive MIMO in 5G Networks: Strategy and technical studies in Indonesia. Indonesian Journal of Advanced Research, 2(3), 189–200. https://doi.org/10.55927/ijar.v2i3.3563

[31] Singhwal, S. S., Kanaujia, B. K., Singh, A., Kishor, J., & Matekovits, L. (2020). dual-band circularly polarized mimo dra for sub-6 ghz applications. International Journal of RF and Microwave Computer-Aided Engineering, 30(10). https://doi.org/10.1002/mmce.22350

[32] Balanis, C. A. (2016). Antenna Theory Analysis and Design. Wiley.

[33] Nel, B. A., Skrivervik, A. K., & Gustafsson, M. (2023). Q-factor bounds for microstrip patch antennas. IEEE Transactions on Antennas and Propagation, 71(4), 3430–3440. https://doi.org/10.1109/tap.2023.3243726

[34] Parizi, S. A. R. (2017, November 15). Bandwidth enhancement techniques. IntechOpen. https://www.intechopen.com/chapters/57320

[35] Kumar, G., & Ray, K. P. (2003). Broadband microstrip antennas. Artech House.

[36] He, Q.-Q., & Wang, B.-Z. (2008). Design of microstrip array antenna by using active element pattern technique combining with Taylor synthesis method. Progress In Electromagnetics Research, 80, 63–76. https://doi.org/10.2528/pier07103006

APPENDICES

A. MATLAB script for implementing AEP method

```
%% beamforming @3.5 GHz for phi=0

PS=0; % to apply successive phase shift between subarrays

[port2_rect_x,  port2_rect_y] =
pol2cart(deg2rad(port2_polar_45_roll_0(:,7)),
10.^(port2_polar_45_roll_0(:,6)/20) );
[port4_rect_x,  port4_rect_y] =
pol2cart(deg2rad(port4_polar_45_roll_0(:,7)+PS),
10.^(port4_polar_45_roll_0(:,6)/20) );
[port6_rect_x,  port6_rect_y] =
pol2cart(deg2rad(port6_polar_45_roll_0(:,7)+2*PS),
10.^(port6_polar_45_roll_0(:,6)/20) );
[port8_rect_x,  port8_rect_y] =
pol2cart(deg2rad(port8_polar_45_roll_0(:,7)+3*PS),
10.^(port8_polar_45_roll_0(:,6)/20) );
[port10_rect_x,port10_rect_y]=
pol2cart(deg2rad(port10_polar_45_roll_0(:,7)+4*PS),10.^(port10_pola
r_45_roll_0(:,6)/20) );
[port12_rect_x,port12_rect_y]=
pol2cart(deg2rad(port12_polar_45_roll_0(:,7)+5*PS),10.^(port12_pola
r_45_roll_0(:,6)/20) );
[port14_rect_x,port14_rect_y] =
pol2cart(deg2rad(port14_polar_45_roll_0(:,7)+6*PS),10.^(port14_pola
r_45_roll_0(:,6)/20) );
[port16_rect_x,port16_rect_y] =
pol2cart(deg2rad(port16_polar_45_roll_0(:,7)+7*PS),10.^(port16_pola
r_45_roll_0(:,6)/20) );

w=[1 1 1 1 1 1 1 1]; %weight of each subarray
beam_rect_x= w(1)*port2_rect_x + w(2)*port4_rect_x +
w(3)*port6_rect_x + w(4)*port8_rect_x + w(5)*port10_rect_x +
w(6)*port12_rect_x +  w(7)*port14_rect_x +  w(8)*port16_rect_x;
beam_rect_y= w(1)*port2_rect_y + w(2)*port4_rect_y +
w(3)*port6_rect_y + w(4)*port8_rect_y + w(5)*port10_rect_y +
w(6)*port12_rect_y +  w(7)*port14_rect_y +  w(8)*port16_rect_y;

[beam_phase,beam_mag]=cart2pol(beam_rect_x,beam_rect_y);

beam_dB=20*log10(beam_mag);

figure
plot(port2_polar_45_roll_0(:,1),beam_dB,'LineWidth', 1.25)
hold on

% sim=xlsread('v3.1_2subarray.xlsx'); % port 14-16 is excited
% sim=xlsread('v3.1_3subarray.xlsx'); % port 12-14-16 is excited
```

```
% sim=xlsread('v3.1_4subarray.xlsx'); % port 10-12-14-16 is excited
% sim=xlsread('Broadside 3.5.xlsx'); %all of 8 port is excited
sim=xlsread('Phi 0 bx 180.xlsx');



plot(sim(:,1),sim(:,2)-1.7,'LineWidth', 1.25)


grid on
legend('AEP','Sim.')
xlim([-180 180])
ylim([-40 30])
xticks([-180 -120 -60 0 60 120 180])
xlabel("Theta (°)")
ylabel("Gain (dB)")


%% multibeam forming

PS1=30; % to apply successive phase shift betwen subarrays
PS2=-30;
PS3=90;
PS4=-90;

[port2_rect_x,  port2_rect_y] =
pol2cart(deg2rad(port2_polar_45_roll_0(:,7)),
10.^(port2_polar_45_roll_0(:,6)/20) );
[port4_rect_x,  port4_rect_y] =
pol2cart(deg2rad(port4_polar_45_roll_0(:,7)+PS1),
10.^(port4_polar_45_roll_0(:,6)/20) );
[port6_rect_x,  port6_rect_y] =
pol2cart(deg2rad(port6_polar_45_roll_0(:,7)+2*PS1),
10.^(port6_polar_45_roll_0(:,6)/20) );
[port8_rect_x,  port8_rect_y] =
pol2cart(deg2rad(port8_polar_45_roll_0(:,7)+3*PS1),
10.^(port8_polar_45_roll_0(:,6)/20) );
[port10_rect_x,port10_rect_y]
=pol2cart(deg2rad(port10_polar_45_roll_0(:,13)),10.^(port10_polar_4
5_roll_0(:,12)/20) );
[port12_rect_x,port12_rect_y]
=pol2cart(deg2rad(port12_polar_45_roll_0(:,13)+PS2),10.^(port12_pol
ar_45_roll_0(:,12)/20) );
[port14_rect_x,port14_rect_y]
=pol2cart(deg2rad(port14_polar_45_roll_0(:,13)+2*PS2),10.^(port14_p
olar_45_roll_0(:,12)/20) );
[port16_rect_x,port16_rect_y]
=pol2cart(deg2rad(port16_polar_45_roll_0(:,13)+3*PS2),10.^(port16_p
olar_45_roll_0(:,12)/20) );
```

```
[port1_rect_x,  port1_rect_y] =
pol2cart(deg2rad(port15_polar_135_roll_0(:,13)),
10.^(port15_polar_135_roll_0(:,12)/20) );
[port3_rect_x,  port3_rect_y] =
pol2cart(deg2rad(port13_polar_135_roll_0(:,13)+PS3),
10.^(port13_polar_135_roll_0(:,12)/20) );
[port5_rect_x,  port5_rect_y] =
pol2cart(deg2rad(port11_polar_135_roll_0(:,13)+2*PS3),
10.^(port11_polar_135_roll_0(:,12)/20) );
[port7_rect_x,  port7_rect_y] =
pol2cart(deg2rad(port9_polar_135_roll_0(:,13)+3*PS3),
10.^(port9_polar_135_roll_0(:,12)/20) );
[port9_rect_x,  port9_rect_y] =
pol2cart(deg2rad(port9_polar_135_roll_0(:,7)),
10.^(port9_polar_135_roll_0(:,6)/20) );
[port11_rect_x,  port11_rect_y] =
pol2cart(deg2rad(port11_polar_135_roll_0(:,7)+PS4),
10.^(port11_polar_135_roll_0(:,6)/20) );
[port13_rect_x,  port13_rect_y] =
pol2cart(deg2rad(port13_polar_135_roll_0(:,7)+2*PS4),
10.^(port13_polar_135_roll_0(:,6)/20) );
[port15_rect_x,  port15_rect_y] =
pol2cart(deg2rad(port15_polar_135_roll_0(:,7)+3*PS4),
10.^(port15_polar_135_roll_0(:,6)/20) );


beam1_rect_x= port2_rect_x + port4_rect_x + port6_rect_x +
port8_rect_x;
beam1_rect_y= port2_rect_y + port4_rect_y + port6_rect_y +
port8_rect_y;

beam2_rect_x= port10_rect_x + port12_rect_x + port14_rect_x +
port16_rect_x;
beam2_rect_y= port10_rect_y + port12_rect_y + port14_rect_y +
port16_rect_y;

beam3_rect_x= port1_rect_x + port3_rect_x + port5_rect_x +
port7_rect_x;
beam3_rect_y= port1_rect_y + port3_rect_y + port5_rect_y +
port7_rect_y;

beam4_rect_x= port9_rect_x + port11_rect_x + port13_rect_x +
port15_rect_x;
beam4_rect_y= port9_rect_y + port11_rect_y + port13_rect_y +
port15_rect_y;

[beam1_phase, beam1_mag]=cart2pol(beam1_rect_x,beam1_rect_y);

[beam2_phase, beam2_mag]=cart2pol(beam2_rect_x,beam2_rect_y);

[beam3_phase, beam3_mag]=cart2pol(beam3_rect_x,beam3_rect_y);

[beam4_phase, beam4_mag]=cart2pol(beam4_rect_x,beam4_rect_y);
```

```
beam1_dB=20*log10(beam1_mag);
beam2_dB=20*log10(beam2_mag);
beam3_dB=20*log10(beam3_mag);
beam4_dB=20*log10(beam4_mag);


figure
plot(port2_polar_135_roll_90(:,1),beam1_dB,'LineWidth', 1.25)
hold on
plot(port2_polar_135_roll_90(:,1),beam2_dB,'LineWidth', 1.25)
hold on
plot(port2_polar_135_roll_90(:,1),beam3_dB,'LineWidth', 1.25)
hold on
plot(port2_polar_135_roll_90(:,1),beam4_dB,'LineWidth', 1.25)
legend("Beam 1 @3.5GHz","Beam 2 @3.8GHz","Beam 3 @3.8GHz","Beam 4
@3.5GHz")
grid on
xlim([-180 180])
ylim([-40 20])
xticks([-180 -120 -60 0 60 120 180])
xlabel("Theta (°)")
ylabel("Gain (dB)")

figure
polarpattern(port2_polar_135_roll_90(:,1),beam1_dB, 'LineWidth',
1.25)
hold on
polarpattern(port2_polar_135_roll_90(:,1),beam2_dB, 'LineWidth',
1.25)
hold on
polarpattern(port2_polar_135_roll_90(:,1),beam3_dB, 'LineWidth',
1.25)
hold on
polarpattern(port2_polar_135_roll_90(:,1),beam4_dB, 'LineWidth',
1.25)


legend("Beam 1 @3.5GHz","Beam 2 @3.8GHz","Beam 3 @3.8GHz","Beam 4
@3.5GHz")
```